Quantum Structures in Photovoltaic Devices

Jenna Holder

Department of Materials

St. Anne's College

DPhil Thesis

Trinity Term 2013

Abstract

A study of three novel solar cells is presented, all of which incorporate a low-dimensional quantum confined component in a bid to enhance device performance.

Firstly, intermediate band solar cells (IBSCs) based on InAs quantum dots (QDs) in a GaAs p-i-n structure are studied. The aim is to isolate the InAs QDs from the GaAs conduction band by surrounding them with wider band gap aluminium arsenide. An increase in open circuit voltage (V_{OC}) and decrease in short circuit current (J_{sc}) is observed, causing no overall change in power conversion efficiency. Dark current - voltage measurements show that the increase in V_{OC} is due to reduced recombination. Electroreflectance and external quantum efficiency measurements attribute the decrease in J_{sc} primarily to a reduction in InGaAs states between the InAs QD and GaAs which act as an extraction pathway for charges in the control device.

A colloidal quantum dot (CQD) bulk heterojunction (BHJ) solar cell composed of a blend of PbS CQDs and ZnO nanoparticles is examined next. The aim of the BHJ is to increase charge separation by increasing the heterojunction interface. Different concentration ratios of each phase are tested and show no change in J_{sc}, due primarily to poor overall charge transport in the blend. V_{OC} increases for a 30 wt% ZnO blend, and this is attributed largely to a reduction in shunt resistance in the BHJ devices.

Finally, graphene is compared to indium tin oxide (ITO) as an alternative transparent electrode in squaraine/ C_{70} solar cells. Due to graphene's high transparency, graphene devices have enhanced J_{sc}, however, its poor sheet resistance increases the series resistance through the device, leading to a poorer fill factor. V_{OC} is raised by using MoO_3 as a hole blocking layer. Absorption in the squaraine layer is found to be more conducive to current extraction than in the C_{70} layer. This is due to better matching of exciton diffusion length and layer thickness in the squaraine and to the minority carrier blocking layer adjacent to the squaraine being more effective than the one adjacent to the C_{70}.

Acknowledgements

My interest in technological innovations started at a young age when my father took me to a pet shop and I was more fascinated by a vacuum cleaner than fluffy rabbits. Throughout school I revelled in solving maths problems and I thank my TGGS school friends and my maths teacher, Mr. Ashcroft, for sharing my enjoyment and making me feel less nerdy. As maths became incomprehensible, physics become more fascinating and I thank my physics teachers: the engaging Mr. Willett and the stylish Mrs. Tolley for opening my eyes to its wonders over the course of seven years. Alongside this, my geography teachers were pressing upon us the gravity of climate change and how we should diversify to renewable energy sources, which spurred my interest in this sector.

My undergraduate years at Warwick not only nurtured me into adulthood but my physics course gave me the tools to understand how the world (and universe) works. To my surprise, I realised that solid state physics was as cool as cosmology and chose this field for my final-year-project. Thanks to my supervisor, Dr. Diane Holland, myself and my project partner, Jon Robinson, were able to run around the department performing all sorts of experiments, making me feel like a 'real' scientist.

Out of a desire to solve the world's energy problems I embarked upon a PhD in the development of solar cells and soon discovered that saving the world is not easy. The work presented in this thesis would not have been possible without the support of my lab group. My supervisor duo was invaluable to me. Dr. Hazel Assender was always on hand to offer realistic and insightful viewpoints on my work. Dr. Andrew Watt provided me with inspiration, guidance and the mindset that "we should all just love each other". This ethos shone through in his lab group from the first day I joined. The more advanced students were always happy to help and chat. Particular mention goes to Shawn Willis, who taught me how to constructively play with solder and cables, guided me on my first steps into LabVIEW and carefully explained many theoretical points to me, all with a huge smile on his face and genuine happiness to teach. I thank Peter Kovacik for his scientific philosophies, fruitful

collaboration and plum wine. Simon Fairclough provided me with much entertainment and was a fab housemate. Laura Droessler and Elva Zou gave the lab a light-hearted and fun feel and are both shining role models to me. I am also forever grateful to Elva for being my rock during tough times and best friend during happy times. As new students came they all added something special to the group. Chris Cattley added a wonderful British wit. Assia Kasdi, Inji Yeom and Natasha Hjerrild brought enthusiasm and new scientific directions, and are really warm-hearted people, whom I'm lucky to have as friends. Darren Neo brought all that plus PbS quantum dots and useful discussion. I have fond memories from the start of my PhD of sitting through lectures and colloquia with Syarif Yahya and my lab-brother Cheng Cheng. I'm lucky to have continued to share the steps of my PhD with Cheng, who has been a great friend, travel companion and scientific collaborator.

Outside of the lab group there are many to whom I am grateful. Laurie Walton guided me through the mechanical workshop, making me far more confident about my practical abilities. Jamie Warner patiently taught me the key aspects of photoluminescence spectroscopy and let me use his setup. Jason Smith engaged in fruitful discussions about quantum dots with me. Richard Turner, Radka Chakalova and Paul Pattinson are others who have warmly helped me out with technical aspects of my project. The EPSRC gave me funds, without which this PhD would not have been possible.

Outside of science, I have met many fascinating people and made many great friends in Oxford without whom extra-lab life would have been much less fun. A special mention goes to my boyfriend, Simone Falco, who has supported me during the final stages of my PhD, despite my dwindling fun-ness!

The final mention goes to my parents, Martin and Angela Holder. Without them I wouldn't be who I am today or where I am today. My parents have selflessly given their all to help me succeed at every stage of life, including these last few years and despite having only a vague idea of what my PhD is about! For that reason this thesis is not dedicated to them. Instead, I dedicate to them the person I have become, and will grow to be, as a result of this experience.

Declaration of originality

This thesis is an account of work carried out by the author in the Department of Materials, University of Oxford under the supervision of Dr Andrew Watt and Dr Hazel Assender. Any work of others that has been drawn upon is duly acknowledged in the text, and a list of references is presented at the end of the thesis. No part of this thesis has been submitted towards the completion of another degree at the University of Oxford or elsewhere.

Table of contents

List of abbreviations

α	Absorption coefficient
Φ	Work function
$\hbar$	Planck's constant

Al	Aluminium
AlAs	Aluminium arsenide
AM 1.5	Air mass 1.5
AQE	Apparent quantum efficiency
C	Capacitance
CB	Conduction band
CQD	Colloidal quantum dot
CV	Capacitance - voltage
EQE	External quantum efficiency
E_a	Activation energy
E_F	Fermi energy
E_g	Band gap energy
FTIR	Fourier-transform infrared spectroscopy
GaAs	Gallium arsenide
HOMO	Highest occupied molecular orbital
I(0)	Input light intensity
I(x)	Intensity of light transmitted through a sample of thickness x
IB	Intermediate band
IBSC	Intermediate band solar cell
InAs	Indium arsenide
InGaAs	Indium gallium arsenide
IR	Infrared
ITO	Indium tin oxide
J_0	Reverse saturation current density
J_{dark}	Dark current density
J_{ph}	Photocurrent density
J_{sc}	Short circuit current density
JV	Current density – voltage

k_B	Boltzmann constant = 8.617 x 10^{-5} eV K^{-1}
LUMO	Lowest unoccupied molecular orbital
MBE	Molecular Beam Epitaxy
MoO_3	Molybdenum tri-oxide
n	Ideality factor
PbS	Lead sulphide
PCE	Power conversion efficiency
q	Charge on an electron
Q	Total charge
QD	Quantum dot
T	Temperature in units of Kelvin
UV	Ultraviolet
V	Voltage
VB	Valence band
V_{OC}	Open circuit voltage
ZnO	Zinc oxide

1. Introduction

1.1 Photovoltaics motivation

This thesis investigates quantum nano-materials in a range of solar photovoltaic (PV) devices, focussing on ways of improving device efficiency. PV devices (or 'solar cells') are made from semiconductors which convert sunlight into electricity. With energy from sunlight exceeding global electrical energy consumption by a factor of 60,000[1,2], PV has great promise in satisfying the world's electricity demand. At present, 71 % of electricity is generated by fossil fuels[3] but with reserve/production ratios of most fossil fuels decreasing[4] and CO_2 emissions from fossil fuels being the main contributor to climate change[5], it is crucial to develop cleaner, renewable sources of energy.

Despite this, the fraction of the world's electricity that is generated by solar power is less than 0.5 %[4]. What is hindering its deployment is the high cost compared to other energy sources[6]. Thus the goal in this field is to create solar devices with an overall low cost per watt of power. Chapter 4 of this thesis examines high efficiency[7], but high cost[8], solar cells made from III-V materials, with a GaAs base. Chapters 5 and 6 of this thesis study colloidal quantum dot and organic solar cells which have a lower efficiency[7,9] but compensate with a low cost[8–10].

Each device studied benefits from the advantages of a low-dimensional component. Decreasing the number of dimensions decreases the density of energy states in a material[11]. This means the gap between the conduction band and valence band (the 'band gap') can change[11,12], a property utilised in devices in chapters 4 and 5, which use zero-dimensional quantum dots as photon absorbers.

Chapter 6 uses graphene as the electrode of a solar cell, where charge transport is confined to the two dimensions of the graphene sheet. This renders it more likely that charge carriers will not

scatter during transport, which is termed ballistic travel[13]. In this case, carrier transport is just limited by the band structure. The 2D nature of graphene results in an interesting band structure, which, as will be seen in the section 2.4, renders charge carriers highly mobile.

In each study the systems have been modified from current standards, in an effort to improve solar cell power output. This chapter will go on to explain the physics of solar cell structures and, with this knowledge at its base, chapter 2 will examine the challenges faced in the photovoltaics industry.

1.2 Solar cell fundamentals

1.2.1 Photon absorption

Semiconductors can absorb photons that have at least the energy of the semiconductor band gap (E_g) (figure 1-1). The energy of the photon promotes an electron from the valence band to the conduction band, creating an electron-hole pair.

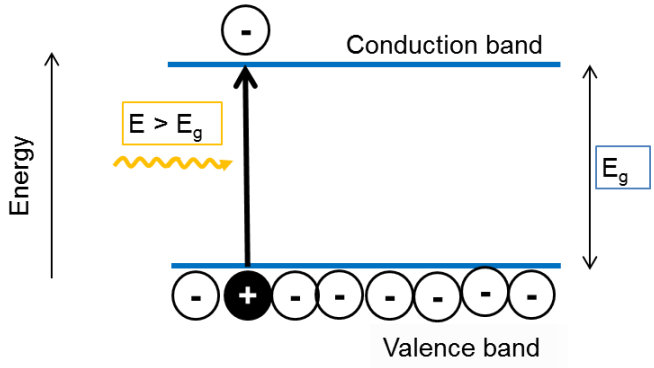

Figure 1-1: Absorption of a photon (yellow arrow) with energy, E, greater than the energy of the semiconductor band gap, E_g. This promotes an electron (white circle) from the conduction band to the valence band, leaving a positively charged 'hole' (black circle) in the valence band.

The thickness (x) and absorption coefficient (α) of a material determine how much light is absorbed, according to the Beer-Lambert law[14] (equation 1-1):

$$I(x) = I(0)e^{-\alpha x}$$

Equation 1-1

where $I(0)$ is the input light intensity and $I(x)$ is the intensity of light transmitted through the sample.

The absorption coefficient is inversely proportional to the wavelength of light[14], meaning that longer wavelengths are absorbed less than shorter wavelengths. In principle this results in shorter wavelengths being fully absorbed at the front of a material with longer wavelengths needing to pass through a greater depth of material for complete absorption.

1.2.2 Charge separation

Once an electron-hole pair is created, a driving force is needed to separate the opposite charges. For the cells in this thesis, this driving force is the electric field created at a junction between semiconductors of different doping or energy levels. An electric field will always drive electrons in one direction and holes in the other direction.

There exists more than one type of junction, with the p-n junction and p-i-n junction being the most common for inorganic crystalline solar cells and the excitonic junction used in molecular organic solar cells[15].

1.2.2.1 p-n junction

A p-n junction is a junction between a p-doped material and an n-doped material. If the two materials are the same, then the junction is called a p-n homojunction. If, instead, the materials are different, it is called a p-n heterojunction. When the materials come into contact, the majority carriers - holes from the p-doped side and electrons from the n-doped side - diffuse across the junction and recombine. This leaves negatively-charged ions at the edge of the p-type region and positively charged ions in the n-type region (figure 1-2A). The electric field created as a result of these ions opposes the diffusion of holes from the p-type region and electrons from the n-type region (i.e. impedes the flow of majority carriers across the junction) and eventually equilibrium is reached and the Fermi levels of both sides align (figure 1-2B).

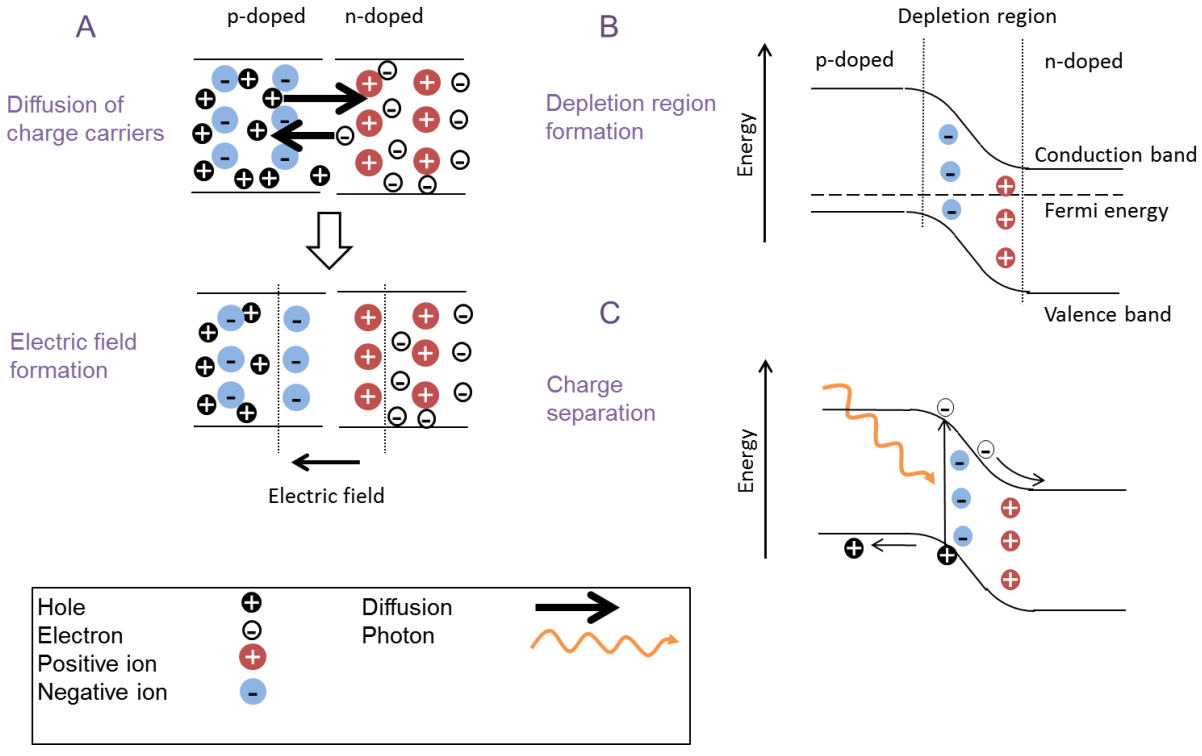

Figure 1-2: The formation of a p-n junction A: The diffusion of charge carriers when p-doped and n-doped materials are put in contact, which leads to the formation of an electric field. B: band diagram of the p-n structure with the depletion region shown. C: Operation of the p-n junction when illuminated.

The region of charged ions is known as the space charge region, or depletion region, as it is devoid of free charge carriers. Photogenerated electrons in this region will drift towards the n-doped side and photogenerated holes will drift towards the p-doped side, as a consequence of the built-in electric field.

1.2.2.2 The depletion width

The width of the depletion region depends on the relative doping either side of the junction. The equilibrium condition – when the Fermi levels align – can only be reached when the charge on each side is balanced. Thus if, for example, the n-doped side is less heavily doped than the p-doped side, a greater depth of the n-doped side must be depleted of free carriers before it matches the depleted area in the p-doped side. This is illustrated in figure 1-3.

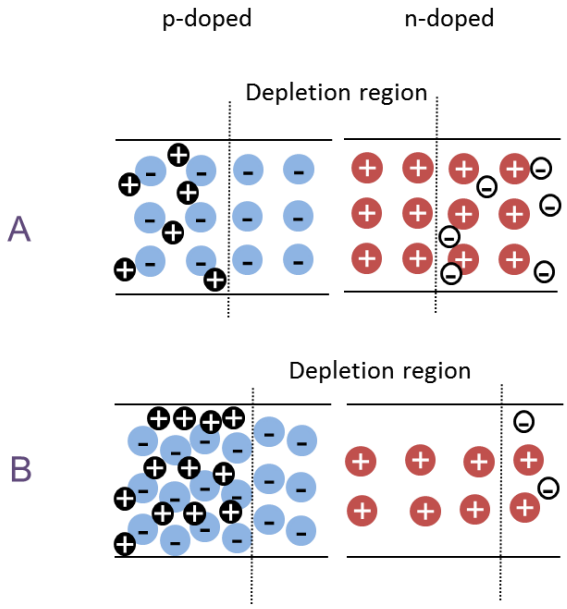

Figure 1-3: The spatial distribution of the depletion region in a p-n junction when the materials are A: equally doped and B: when the n-doped size is less heavily doped than the p-doped side.

1.2.2.3 The solar cell as a diode

The p-n junction is effectively a diode. Applying a reverse bias across the solar cell increases the barrier height, preventing majority carrier flow. Applying a forward bias across the solar cell decreases the barrier height, so electrons from the n-doped side and holes from the p-doped side can more easily traverse the junction. As barrier height decreases, majority carrier flow increases in an exponential manner. This scenario is described by the diode equation (equation 1-2), with J_{dark} being the current density that flows when the cell is not illuminated, J_0 being the reverse saturation current, q being the charge on an electron, V being the applied voltage, k_B being Boltzmann's constant and T being the temperature. The reverse saturation current is the small, bias-independent current that flows due to the diffusion of minority carriers across the junction[16].

$$J_{dark} = J_0 \left(e^{\frac{qV}{k_B T}} - 1\right)$$

Equation 1-2

Under illumination, the photogenerated current density (J_{ph}) must be added to this equation, so the complete equation for an ideal solar cell is shown in equation 1-3:

$$J = J_{ph} + J_0 \left(e^{\frac{qV}{k_B T}} - 1\right)$$

Equation 1-3

This equation follows the sign convention of negative photocurrent and positive dark current.

1.2.2.4 p-i-n junction

If a layer of intrinsic material is sandwiched between the p-doped and n-doped materials then a depletion region is still created as a result of the p-doping and n-doping and the potential difference generated is the same as that of the p-n junction. However the intrinsic region has a much lower free carrier concentration than the p- and n-doped sides, so the potential difference is dropped

across the whole of the intrinsic region. This extension of the depletion region can be favourable to the p-n junction if charges in the absorber material have poor mobility as, in the p-i-n design, the extended electric field will aid their drift to the far edges of the junction[17].

As will be seen in chapter 4, some solar cell architectures incorporate secondary absorber materials into the junction, in which case, being able to widen the depletion region to encompass these structures is a great benefit.

1.2.2.5 Excitonic junction

The internal electric fields at p-n and p-i-n junctions are not sufficient to separate charges in all materials. Within some molecular semiconductors, very tightly bound electron-hole pairs form upon photon absorption[15]. Such an electron-hole pair is called a Frenkel exciton, in which the electron and hole are Coulombically-bound over the distance of one molecule[18]. The field in a p-n or p-i-n junction is usually too weak to split a Frenkel exciton; these excitons will only dissociate into a separate electron and hole when they reach an interface of two materials with a larger energy offset than the exciton binding energy (E_b)[15]. Thus one material will act as an electron donor and the other as an electron acceptor. A schematic of the junction is shown in figure 1-4.

The Coulomb energy that binds the excitons is inversely proportional to the square of the dielectric constant of the semiconductor[19], so the tightly-bound Frenkel excitons are common in organic materials, which have a low dielectric constant. In comparison, inorganic crystalline solar cells typically have high dielectric constants, and photogeneration in these results in Wannier-Mott excitons, which are bound over a distance of up to 10 nm[18]. This distance is relatively large - much larger than the atomic spacing in a crystal lattice – which enables easier separation of the electron and hole.

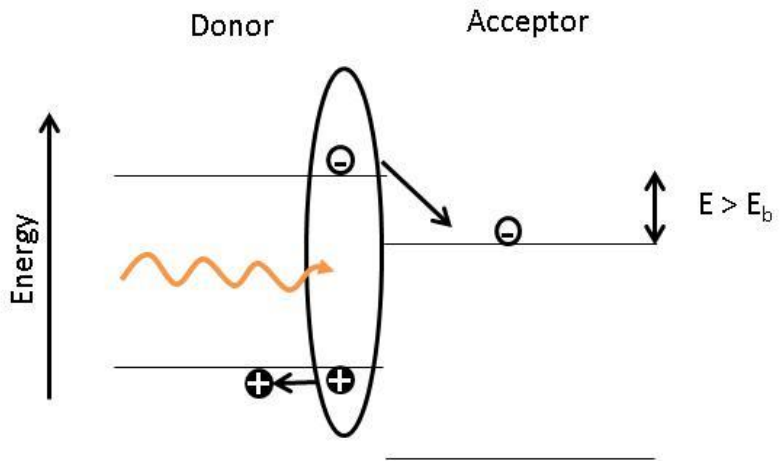

Figure 1-4: Excitonic junction. The photon creates a bound electron-hole pair, with binding energy, E_b. If the Frenkel exciton reaches the interface, and if there is a great enough energy level offset, the exciton can dissociate into separate charges.

1.2.3 Charge transport

Once electrons and holes are separated at the heterojunction, they must be transported through the semiconductor to the electrodes. The energy level alignment at the semiconductor-electrode interface is now crucial to ensure that charges can be easily injected into the electrodes. There are two types of semiconductor-metal junctions: Ohmic and Schottky[15]. Which junction forms depends on the relative work functions of the metal and the semiconductor. The work function of a material is the minimum energy required to remove an electron from the material, and is equal to the Fermi energy in a semiconductor or the electron affinity in a metal[15].

1.2.3.1 Ohmic junction

An Ohmic junction is one which favours the flow of majority carriers from the semiconductor to the metal. For a p-type semiconductor, this junction forms if the work function of the metal is greater than the Fermi level of the semiconductor, as shown in figure 1-5B. The opposite is true for an n-type material.

1.2.3.2 Schottky junction

If the metal-semiconductor junction inhibits flow of majority carriers then it is called a 'Schottky junction'. These are formed if the work function of the metal is either lower than the Fermi level of a p-type semiconductor or higher than the Fermi level of an n-type semiconductor. This scenario is shown in figure 1-5C for a p-type semiconductor. Some solar cells, especially at initial stages of development, have used this structure rather than heterojunctions for separating charges[20,21].

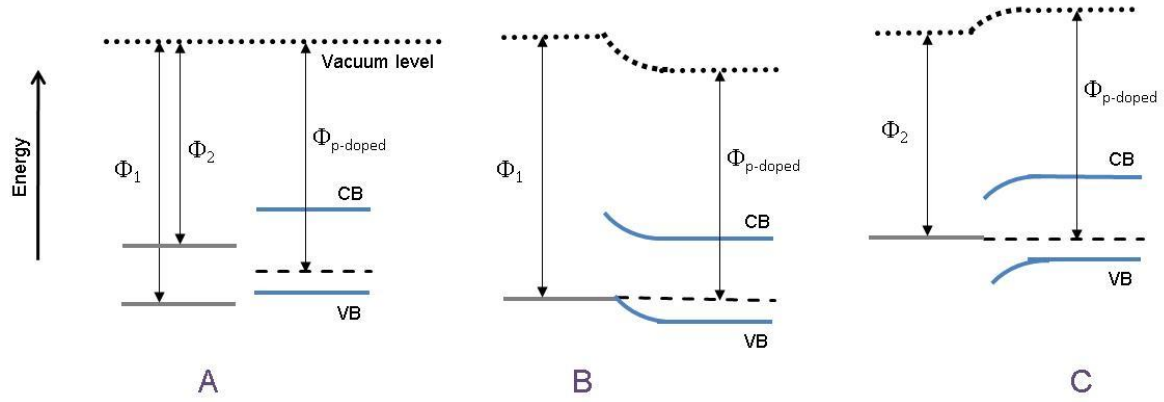

Figure 1-5: Metal/p-doped semiconductor junctions. A: pre-contact energy level alignment of two metals (grey lines) with work functions, Φ_1 and Φ_2, and a p-doped semiconductor with the work function $\Phi_{p\text{-doped}}$, being the energy between the Fermi energy (dashed line) and the vacuum energy (dotted line). Conduction bands (CB) and valence bands (VB) are also shown. B: Ohmic contact of semiconductor with metal 1. C: Schottky contact of semiconductor with metal 2.

1.2.4 Power output of a solar cell

The steps outlined in sections 1.2.1 – 1.2.3 detail the process that is undertaken to generate photocurrent. To generate power, the solar cells must also produce a photovoltage. The photovoltage is limited by the difference in bias between the separated electrons and holes, which is given by the difference between their quasi-Fermi levels under illumination[22]. The key parameters that describe the photocurrent and photovoltage are, respectively, the short-circuit current (I_{sc}) and the open-circuit voltage (V_{OC}). I_{sc} is the photogenerated current that flows through the circuit when there is no load on the circuit[23], so the electrodes are connected with no potential difference

between them. In practice, as I_{sc} is proportional to device area, and different solar cells have different device areas, the parameter J_{sc} is used, which is the short-circuit current density. V_{OC} is the voltage that develops at the solar cell electrodes when the device is illuminated and the electrodes are disconnected[23] (so there is an infinite load on the circuit and no current flows). An actual solar cell operates with a load between zero and infinity and also has a maximum power output at some value lower than the $J_{sc}.V_{OC}$ product.

The maximum power output of a solar cell will depend on resistances through the cell[23], namely series resistance and shunt resistance. Series resistance resists current flow through the cell and could be caused by the semiconductor or resistive contacts[23]. High values can reduce J_{sc}. The shunt resistance of a solar cell should ideally be very high, as this resistance prevents leakage currents caused by direct current flow between the opposite electrodes[24]. If this value is too low, V_{OC} can decrease. The solar cell equation including parasitic resistances is given in equation 1-4:

$$J = J_{ph} + J_0 \left(e^{\frac{q(V+JAR_s)}{k_B T}} - 1 \right) + \frac{V + JAR_s}{R_{sh}}$$

Equation 1-4

where A is the area of the solar cell.

The parameter that relates actual maximum power to theoretical maximum power is the fill factor (FF), given by equation 1-5, where J_{max} and V_{max} are the current density and voltage that combine to give the maximum power. Plotting equation 1-4 (figure 1-6) enables a visualisation of FF, in which it is the ratio of the areas of the green square to the red square.

$$FF = \frac{J_{max}.V_{max}}{J_{sc}.V_{OC}}$$

Equation 1-5

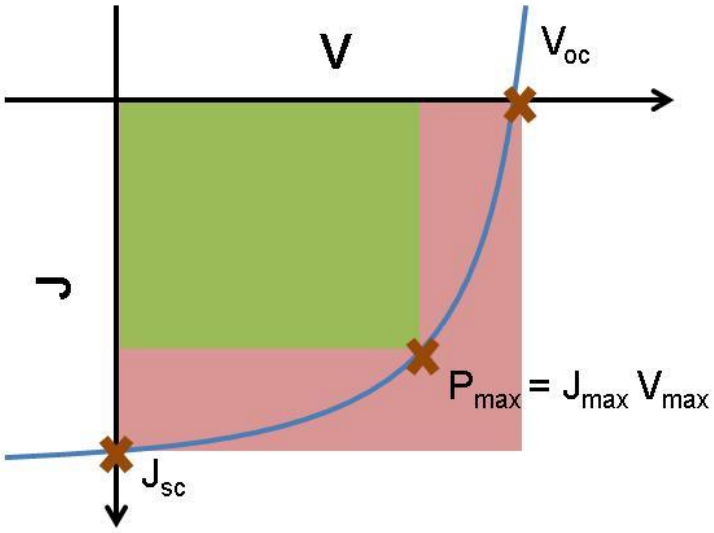

Figure 1-6: Plot of equation 1-4 (blue line) on current density (J) and voltage (V) axes. Key positions on the curve are marked: short circuit current (J_{sc}), open circuit voltage (V_{OC}) and maximum power (P_{max}). The fill factor of the curve is the ratio of the areas of the green square to the red square.

Collating these parameters result in the key figure of merit for solar cells: the power conversion efficiency (PCE), which is the ratio of the output power to the input power[23], as given by equation 1-6.

$$PCE = \frac{J_{max}.V_{max}}{P_{in}} = \frac{J_{sc}.V_{OC}.FF}{P_{in}}$$

Equation 1-6

1.2.5 Low dimensions

As materials in this body of work utilise zero-dimensional and two-dimensional systems, a brief introduction to the physics of these is given in this section. The focus will be on the band-gap tuneability of quantum dots as graphene has very particular properties that will be discussed in due course. However, this discussion of the changing energy level structure in low-dimensions is still relevant to 2D materials.

Quantum dots are materials scaled down to the nanoscale. Past a certain material-specific size threshold, called the exciton Bohr radius, quantum physics dictates that the band gap of a material increases as its size decreases[25]. The Bohr radius is the radius of the orbit of an electron around the nucleus in a hydrogen atom[26]. Converting this term to excitons, the exciton Bohr radius is the separation between the electron and hole in the bound pair[25]. Confining the exciton to lower than this size results in a change in how the energy states are described.

The energy of conduction band electronic states in a material, E, is given by equation 1-7 [27]:

$$E = E_0 + \frac{\hbar^2 k^2}{2m^*}$$

Equation 1-7

where E_0 is the energy from the top of the valence band to the bottom of the conduction band, k is the wavevector and m^* is the effective mass of the electron. The spacing between k states, Δk is inversely proportional to the size of the material (L)[28], as given by equation 1-8. When the size of the material is small, Δk will be large. E is proportional to k^2, so the spacing between energy levels is proportional to $(\Delta k)^2$. This results in large energy level spacings, and thus discrete levels, when the material is small[28], according to equation 1-9, where n is an integer.

$$\Delta k = \frac{\pi}{L}$$

Equation 1-8

$$E = E_0 + \frac{\hbar^2}{2m^*}\left(\frac{n^2\pi^2}{L^2}\right)$$

Equation 1-9

As the term in brackets in equation 1-9 cannot have a value of zero, this leads to band gap widening as shown in figure 1-7. Materials confined to this scale in all three dimensions are called quantum dots. Therefore if the size of the quantum dot can be controlled, then the band gap of the

semiconductor can be tuned. This can enable a fuller utilisation of the solar spectrum, via either optimum tuning of a single junction solar cell to the solar spectrum or by using semiconductors of different band gaps to absorb light across the solar spectrum.

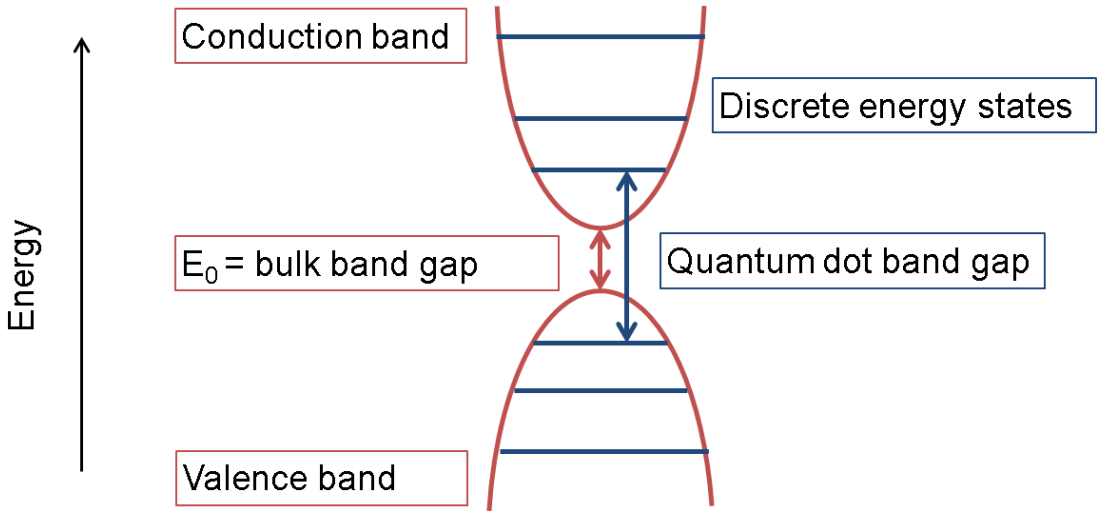

Figure 1-7: Band diagram of a 3D bulk material (red lines) compared with a quantum-confined material (blue lines)

2. Challenges in photovoltaics

To make photovoltaics commercially attractive it must have a low cost-to-power output ratio. The path of PV through time has led to a number of low-cost options[8,29,30], including using materials compatible with low-cost solution-based processing[9,10], for example that of colloidal quantum dots, studied in chapter 5. Solar cell power conversion efficiencies have concurrently increased across all types of solar cells[31], with the low-dimensional structures of this thesis aiming to increase efficiency further.

2.1 Lowering the cost of photovoltaic devices

First generation devices are made from inorganic semiconductor wafers[32], e.g. silicon, gallium arsenide and indium phosphide. Current monocrystalline cells of this structure have power conversion efficiencies reaching 25%[7]. The drawback of crystalline wafer solar cells is that they are costly to produce[33]. Thin-film 'second-generation' solar cells were developed to combat this issue[32,34] Common materials used for these are cadmium telluride, copper indium gallium selenide (CIGS), polycrystalline silicon and amorphous silicon, with manufacturing costs now lower than $0.70/Watt[35]. Later on, in a third generation of devices, came organic photovoltaics and colloidal quantum dot solar cells, utilising cheap materials[8] and with the potential for low-cost processing[9,10]. The cheaper solar cells tend to also have a lower efficiency[7,31]. To improve efficiency the physics of device operation must be tuned. The following sections will examine ways that have been proposed to improve PV efficiency, focussing on the methods explored in this thesis. Section 2.2 describes methods to increase photon absorption in the semiconductor, 2.3 examines ways of improving charge separation of photogenerated charges and 2.4 considers how the choice of transparent electrode affects device performance.

2.2 Improving the efficiency by increasing photon absorption

2.2.1 The limitations of a single band gap

The range of the solar spectrum that can be absorbed by a semiconductor is limited by its band gap energy, with photons of energy lower than this value unable to be absorbed (figure 2-1A). Simply choosing a material with a small band gap would also not be ideal because the excess energy of highly energetic photons is lost as heat as it relaxes to the band edge, rather than it being utilised as electrical energy[36] (figure 2-1B).

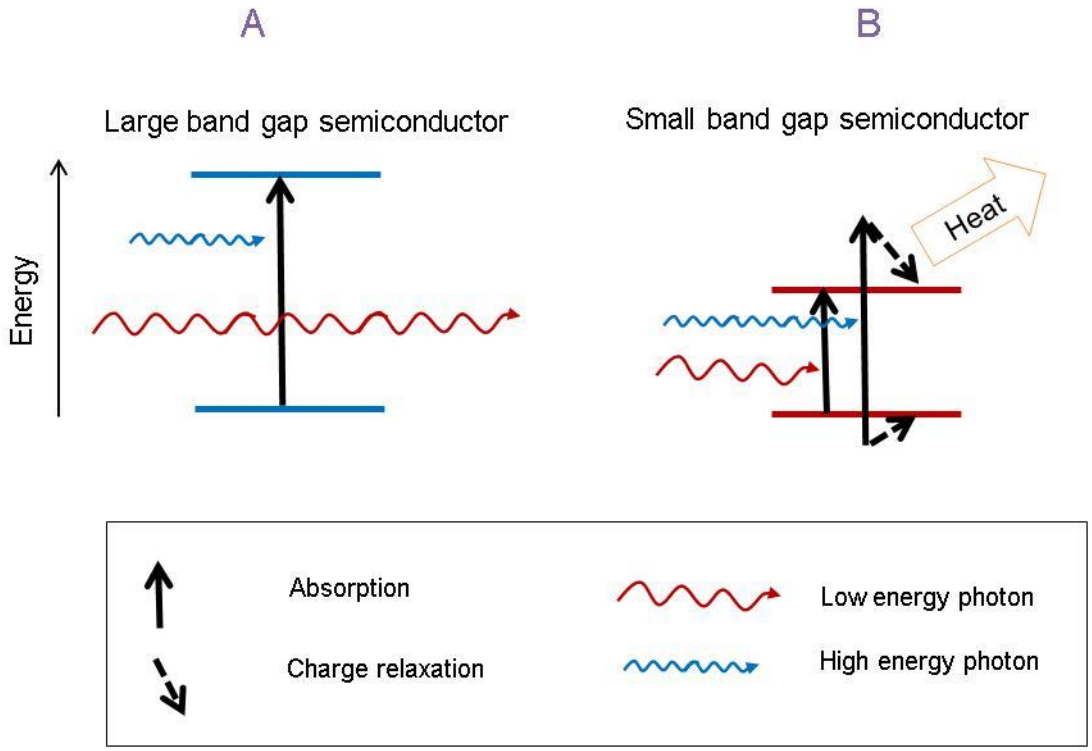

Figure 2-1: A: A large band gap semiconductor absorbing high energy light (blue arrow). Photons with energy less than the band gap (red arrow) cannot pass through. B: A small band gap semiconductor which absorbs low and high energy photons, but the electron-hole pair created with the high energy photon will quickly relax to the band edges via phonons, which will generate heat.

The theoretical maximum possible efficiency for a single-gap solar cell on Earth under concentrated sunlight is set by the Shockley-Queisser Limit, which stands at 40.7%[37]. This limit takes into account

losses from thermal radiation of the device, radiative recombination of electron and holes after photogeneration and losses due to inefficient use of the solar spectrum. Various methods have been proposed to increase this value by means of absorbing more of the solar spectrum.

One method is to use small band gap materials that - when excited with energy greater than twice the band gap - can create two or more electron-hole pairs. This can happen when the initially excited very energetic electron relinquishes its energy, which generates other excitons across the band gap[38]. This process is termed 'multiple exciton generation' (MEG). Most studies have been on the semiconductors rather than complete solar cells[39–41] but solar cells have shown MEG-induced photocurrent increases[42,43] and, if the competing process of hot-carrier cooling can be overcome, then further improvements could be made[44].

Another way is to use more than one material in a solar cell, so light of different wavelengths can be absorbed with little excess energy loss. This is the principle behind the tandem solar cell. In a tandem solar cell, a stack of semiconductors each absorbing a different path of the solar spectrum, can hypothetically reach 86% efficiency under concentrated sunlight[45]. Inorganic crystalline triple-junction devices have shown efficiencies over 40% under concentrated light[46]. Challenges in manufacturing tandem cells include ensuring lattice matching[47,48] and good electrical contact between layers[49]. These problems increase as more layers are used; however this is the only way to get closer to the Shockley-Queisser limit for these cells.

Another structure that employs more than one band gap is the intermediate band solar cell. This is the device that chapter 4 is based upon.

2.2.2 Intermediate band solar cells

The principle behind an intermediate band solar cell (IBSC) is shown in figure 2-2. If there is an energy band between the conduction band (CB) and valence band (VB) of a semiconductor, then photons of energy less than the band gap (E_g) can be absorbed and could generate current via the two step VB – IB then IB – CB process. It has been calculated that the Shockley Queisser efficiency limit for these cells should reach 63.1% under concentrated light[50].

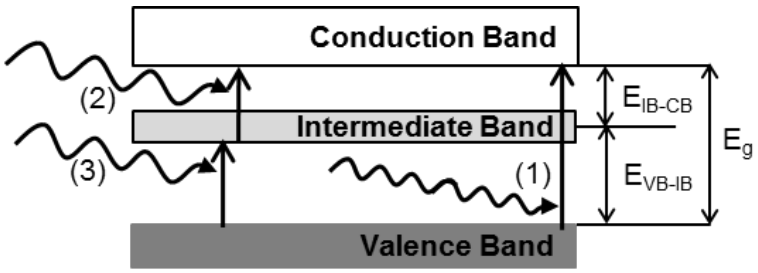

Figure 2-2: Schematic band structure of an intermediate band solar cell (IBSC) of bulk band gap E_g. As well as valence band (VB) – conduction band (CB) photon absorption (1), photons of energy less than E_g can be used in a two-step process ((2) and (3)) to generate current. These low energy photons must have energy greater than E_{VB-IB} to promote an electron to the intermediate band and energy greater than E_{IB-CB} to promote an electron to the conduction band.

To get anywhere near the Shockley-Queisser limit, certain attributes are required from an IBSC. The intermediate band energy states should act primarily as current generation centres and not as mid-gap recombination sites[51]. To achieve this there should be a high-enough density of mid-band-gap states to form a continuum[52]. Additionally, the intermediate band should be in electrical isolation from the conduction band and valence band, which requires careful choice of IB material[53]. If there were energy states in between these bands then the quasi-Fermi energy of photogenerated charges could pin to that of the intermediate band, reducing the photovoltage[54].

Many methods to achieve the IBSC have been considered. The first method devised to create sub-band gap levels was to implant impurities within the intrinsic layer of a p-i-n device[55,56]. However, these discrete impurities could act as recombination centres and thus reduce the short circuit current[57]. Another method is to create alloys in which the intermediate band is a natural result of its crystal lattice structure. A popular route has been to substitute titanium into III-V materials[58].

Theoretical[58] and experimental work[59–61] has been performed on these types of structures; however the high concentration of Ti required brings manufacturing challenges[61]. Much research has been performed on III-V p-i-n solar cells with embedded quantum wells[62–64]. These have shown good photocurrent yield but also exhibit drops in open circuit voltage[63,64], which have been attributed to increased recombination and lack of isolation of the quantum well band gap from the energy bands of the III-V host semiconductor. A theoretical improvement on this design, and the device that will be discussed in chapter 4, is the quantum dot intermediate band solar cell.

2.2.3 Quantum dot intermediate band solar cells

As seen from section 1.2.5, quantum dots have discrete energy levels. As QDs are confined in three directions, these energy levels are more discrete than for less confined structures, such as quantum wells. This leads to the reason QDs are the most promising structures to achieve isolation of the intermediate band: a high-density, regularly-spaced array of discrete QD energy levels embedded in the intrinsic region of a wider band gap p-i-n solar cell should result in no states between the IB and the CB and VB of the p and n materials[65].

A further benefit lies in the ease of manufacturing of the quantum dots. Since the inception of the quantum dot intermediate band solar cell by Marti et al.[53] in 2000, by far the most prevalent materials combination has been gallium arsenide (GaAs) with indium arsenide (InAs) quantum dots, chosen because of manufacturing ease: InAs is deposited with molecular beam epitaxy and self-assembles to form QDs via the Stranski-Krastanov growth method[66]. Although, at about 1.4 eV, the band gap of GaAs is far from the Shockley-Queisser limit ideal of 1.96 eV[67], the system provides a good base for research.

2.2.4 InAs/ GaAs QD IBSCs

Compared to GaAs reference cells, the quantum dot cells have exhibited an increase in photocurrent at low energy regions, emanating from the InAs quantum dot transitions[68,69]. However, often J_{sc} increases have been small and in most cases there is an accompanying decrease in open circuit voltage[70,71], suggesting that the intermediate band is not in isolation from the conduction and valence bands. The cause of this has been cited to be a by-product of the InAs self-assembly process. In this process, the compressive strain in the InAs caused by the lattice mismatch between the InAs and GaAs can lead to quantum-well-like layers beneath the dots[72,73], which increases as the number of QD layers increase[70,72]. These layers can be problematic as a continuum of energy states could then form between the QD energy state and the CB, destroying the desired IB isolation. To relieve this problem a few methods have been explored, starting with incorporating strain-compensating materials in to the device structure.

2.2.5 InAs/GaAs QD IBSCs – strain reduction

Identifying materials that are in tensile strain with GaAs and incorporating these between quantum dot layers is one way of offsetting the InAs compressive strain[74–76]. Strain-compensation layers with band gaps lower than the bulk material (e.g. GaNAs[76]) have not improved $V_{OC.}$ However, promise has been shown with GaP, which has a band gap of around 2.2 eV: much greater than the 1.4 eV band gap of the GaAs bulk material[75,77]. Despite V_{OC} still not matching that of the p-i-n device without quantum dots, it is greater than that of the QD device without a strain-compensation layer.

2.2.6 InAs/GaAs QD IBSCs – wide band gap layers

The reason the wide-band gap strain-compensation layer seems more effective than the narrow-band gap layer might originate from the decreased recombination in these devices[75]. Quantum dots can act as recombination centres[78] and higher recombination would increase injected dark current in a device. As V_{oc} is equal to the applied bias at which forward photocurrent and reverse dark current cancel, an increase in dark current would reduce V_{oc}. Wei and Forrest[79], suggested that wide band gap barriers around the QDs might reduce injection and thus recombination and dark current. Based on this theory Sablon et al.[80] made 'DFENCE' cells with AlGaAs barriers either side of the InAs QDs in a GaAs matrix. They made samples with different numbers of dot layers. Two out of three samples showed slight V_{oc} increases, with the third showing a slight decrease. A lower current was observed from energy states below the GaAs band gap, which they took as evidence that the energy barrier was impeding charge extraction (and would thus impede injection). However, although current from energy states between the QDs and the CB was suppressed, this was not always true from the QDs themselves, casting doubt over whether the AlGaAs does prevent charge extraction. Thus overall, the results were inconclusive.

In this study, an AlAs barrier is used on top of the InAs QDs. It might be more successful than AlGaAs because it has been found that AlAs can suppress InAs and GaAs intermixing[81–83], evidenced by a redshift of photoluminescence from the quantum dots, taken to mean that they have a reduced gallium content. Indium/ gallium intermixing was studied by Eisele et al.[84], who determined that when the InAs QDs are capped by GaAs, mixing of indium and gallium occurs to minimise the energies of the QD structures. This results in the formation of InGaAs layers above and to the sides of the quantum dot, which causes energy states intermediate to those of the InAs and the GaAs. If AlAs can prevent the formation of these states then it can not only help to prevent interaction of the conduction band and intermediate band but can reduce non-radiative recombination, as demonstrated by more intense photoluminescence spectra from AlAs-coated dots[81]. Furthermore,

AlAs does have a wider band gap than GaAs so can also act as an electronic barrier to charge carriers[85]. This can help to maintain isolation of the intermediate band.

The first solar cell of this design was manufactured in 2011[83] and showed promising results. However, it was not until this year (2013) that the mechanisms behind the AlAs-induced performance changes were studied[86], which chapter 4 of this thesis aims to build upon.

2.3 Improving efficiency by increasing charge separation

After electron-hole pairs are generated they have to be separated into electrons and holes before these charges can drift to the electrodes. The problem with p-n and excitonic junctions lies in the small charge separation region compared to the thickness of the solar cell. If an exciton cannot diffuse to the depletion region (in a p-n cell) or the heterojunction (in an excitonic cell) then it is unlikely to dissociate and thus will not contribute to the J_{sc}. This places a limit on the maximum useful thickness of the photon-absorbing layers. To overcome this problem in organic solar cells, the bulk heterojunction architecture was devised[87], in which the donor and acceptor materials are blended together, resulting in a much greater interface area. This structure has had much use with organic solar cells[88,89] and some use in hybrid organic-inorganic solar cells[90,91] but is only just coming into play for all-inorganic devices[92,93]. Colloidal quantum dot solar cells are one such inorganic system of interest.

2.3.1 Colloidal quantum dot solar cells

Colloidal quantum dot solar cells (CQDs) offer a solution to two of the drawbacks of market-dominating crystalline solar cells: their high cost of manufacture and their inability to utilise the entire solar spectrum[94]. CQDs are grown from precursor materials in solution at low temperature

(150 ^{o}C for the CQDs in chapter 5) and without the need of clean room. This lends itself to the possibility of creating CQD devices via roll-to-roll processing, potentially resulting in a low fabrication cost[94,95]. The physics of the CQDs is the same as that for the InAs QDs discussed in sections 1.2.5 and 2.2, i.e. they have discrete energy levels and tuneable band gaps. This latter property is another reason why CQDs are desirable for use in solar cells.

2.3.2 PbS quantum dots

Many CQD materials have been grown for solar cell use[96], some of the most well-known being CdTe, CdS, Si, CZTS and lead chalcogenides. In this work, PbS QDs are used. PbS and PbSe are often favoured because of their low bulk band gaps (that of PbS is 0.41 eV[97]), resulting in the ability to tune the dots to absorb at different regions across the solar spectrum. This low band gap also favours their use in multiple exciton generation (MEG) applications to create more than one exciton per excitation[98], as discussed in section 2.2.1. Furthermore, lead chalcogenide CQDs have a high carrier lifetime (tens of microseconds[93]), which improves drift and diffusion length[93,99]. CQDs can also be synthesized with a low size dispersion[94,100], facilitating fine-tuning of the desired size/ band gap.

Other factors, aside from electrical properties must be considered when choosing a quantum dot material. Oxidation sensitivity is important as it affects whether or not the dots must be made in a nitrogen dry-box and what type of device encapsulation is needed. In this respect, PbS is preferred over PbSe as air-stable PbS devices has been reported[101] but work is still underway to achieve the same with PbSe[102]. Increased stability would also ease toxicity concerns. Lead is more stable in PbS form than in elemental form[95] but stability and good encapsulation are necessary to ensure that the quantum dot form has suitably low toxicity. It should be pointed out that these same risks have not stopped cadmium chalcogenide QD-based solar cells becoming widespread[103]. Another vital factor is

the cost of the materials. FeS_2 has been reported to be the cheapest CQD material but PbS is shown to be inexpensive also at 0.00022 ¢/W (compare this to 0.0097 ¢/W for CdTe)[8].

Development of CQDs in solar cells has progressed from use in Schottky junction structures[104] to planar heterojunctions[105,106]. For use in heterojunctions, many CQD-CQD devices have been made[107,108] In addition, different acceptor materials have been used for different reasons. Polymers have been used frequently[109,110] as they are already created with roll-to-roll processing in mind, something in which nanostructures have great possibility. Wide band gap n-type materials, e.g. TiO_2 and ZnO are favoured for their transparency when used at the front of the cell[111,112], allowing light to pass through to the PbS layer whilst the type-II junction they form with PbS promotes charge separation and extraction. This has led to much development of this combination of structures, with PbS/ZnO bilayers having reached 4.4 % efficiency[113]. ZnO also has the benefit of being able to be formed from solution processing[114], making processing steps compatible with that of CQDs. For these reasons it is the materials combination studied in chapter 5.

2.3.3 Bulk heterojunction CQD solar cells

Moving from a bilayer to a bulk heterojunction structure is an attractive development for CQDs. CQD: organic nanocomposites have been in development since 1996[115] with PbS: organic composites being studied from the middle of the last decade[90,109,116]. The idea of transferring this bulk heterojunction (BHJ) structure to CQD all-inorganic heterojunctions is starting to take hold with the first solution-processed inorganic BHJ being made in 2011[92]. The aim of this device was to enable a thicker cell to be made – to increase photon absorption – but to still ensure that charge separation took place throughout the device. This PbS: modified-TiO_2 depleted bulk heterojunction (DBHJ) device was unlike organic bulk heterojunction solar cells in that the domain sizes of the PbS were large (order of 100 nm), as the TiO_2 induced depletion regions of a similar scale within the PbS

domains. However, current output was initially poorer for the bulk heterojunction cell than for a thinner PbS/ TiO_2 planar device. The authors attributed this to a larger electric field being needed at composite interfaces than planar interfaces, and indeed, once the electron affinity of the TiO_2 was deepened to overcome the PbS exciton binding energy, the short circuit current did improve. The comparison in this modified-TiO_2 case was with a planar device with the original electronic affinity of the TiO_2, so it is hard to quantify from this study the level of improvement that the bulk heterojunction induced.

A different type of PbS bulk heterojunction device is the nano-bulk heterojunction device (NBHJ) created by Rath et al. with Bi_2S_3 as the acceptor material[93]. A nano-bulk heterojunction device is one in which the donor/ acceptor domain size is on the nano-scale, quite different from the PbS/ TiO_2 structure previously mentioned. The authors claim that this leads to a more efficient charge separation and transport, as electron-hole pairs are less likely to recombine before separation (this presumably assumes that interface recombination is negligible). Lifetime measurements indicated that carrier lifetime was higher in the bulk heterojunction devices, suggesting that the improved charge separation does reduce recombination. Furthermore, a three-fold improvement in current output was measured from the NBHJ device. The device structure is such that there are neat PbS and BiS_2 phases either side of the bulk heterojunction. The authors propose that this creates a depletion region in the PbS, so separated holes both diffuse and drift towards their electrode. Despite not assuming much of a depletion region in the BiS_2, the diffusion of electrons seems enough to transport these charges to their electrode. The Bi_2S_3 acceptor has a couple of key advantages over TiO_2. Bi_2S_3 is solution processed with PbS at low temperature, unlike TiO_2. Another significant difference is that Bi_2S_3 is a visible light absorber, whereas TiO_2 is not.

Chapter 5 aims to transfer the benefits of the bulk heterojunction to the PbS/ ZnO system, which has been widely studied in planar form[12,112,117–119].

2.4 Improving efficiency by improving the electrode material

Much work is being carried out on the semiconductor layers of a solar cell, but overall device performance is also related to the performance of the electrodes. Chapter 6 specifically considers the transparent, top electrode.

An ideal top electrode should be:

1. Transparent over the solar spectral range
2. Have good electrical conductivity
3. Have work functions that maintain a high V_{OC}

For some applications, flexibility is also desirable.

2.4.1 Transparent conducting oxides

These top electrodes are commonly transparent conducting oxides (TCOs), particularly tin-doped indium oxide (ITO). ITO is favoured because it typically has a good transmittance of over 85% in the visible spectrum[120] and can exhibit sheet resistances as low as $5\ \Omega$/square[120]. One drawback of devices made with ITO is that indium is scarce and the price of indium is prone to fluctuation[121].

The scarcity of indium has prompted research into other suitable electrode materials. Aluminium zinc oxide (AZO) is one of the preferred transparent conducting oxide alternatives. In terms of chemical resistance and degradation there are pros and cons to using AZO over ITO[122]. The key point, though, is that the resistivity and transparency of AZO[123123–125] are comparable to the ITO values[125,126] so AZO can be widely implemented.

However, scarcity of indium is not the only issue with ITO as an electrode. A general problem with transparent conducting oxides is their brittle nature, meaning it is hard to use them in low-cost roll-to-roll applications[127,128].

2.4.2 Other transparent electrodes

For flexibility, conductive polymers seem like a good option. Poly(3,4-ethylenedioxythiophene) poly(styrenesulphonate) (PEDOT:PSS) has been studied for this purpose. PEDOT:PSS is intrinsically much less conductive than ITO[129] but chemical treatments are raising the conductivity to more comparable values [130–132]. Another way to increase their conductivity is to add a metal grid to the PEDOT:PSS layer[133], with flexible roll-to-roll devices of this type having been made[134,135].

The idea of a metal grid leads on to the technology of metal nanowires. Solution-processed random networks of metal nanowires can make a good transparent conductor[136,137]. A high density of nanowires could block out light but they also enhance scattering, and improvements of J_{sc} over devices made with ITO have been seen[136]. However, both the metal grids and nanowires have so far been made of silver. Remembering the issue with ITO was the scarcity and price of indium, creating silver electrodes does not seem to be an alternative that solves these issues.

Carbon, on the other hand, is abundant in the Earth's crust and cheap. Carbon nanotubes are being tested for use in transparent electrodes[138,139], exploiting the same principle as metal nanowires. The nanotubes have high conductivities[140], however, like other nanowire technologies, resistance at junctions between nanotubes[141] results in a high sheet resistance[142]. Graphene is another carbon allotrope but is a thin sheet, so suffers less from junction resistance than the nanotubes (with the sheet resistance of graphene dependent on the density of resistive grain boundaries in the sheet). Graphene is the material that is studied in chapter 6, with the benefits of this material discussed next.

2.4.3 Graphene

Graphene is a one-atom thick sheet of carbon atoms. Its thinness lends itself to high transparency, with a maximum possible transmittance of 97 %[143]. The transmission spectrum of graphene varies little with wavelength of light, as there is little possibility for interference caused by the thin graphene sheet.

On each carbon atom in the sheet, one s-orbital and two p-orbitals bond with three adjacent carbon atoms. These bonds hybridise and the resultant sigma bond creates a very strong hexagonal lattice structure (figure 2-3). This gives the material great strength[144,145] and flexibility[144,146].

There is one remaining p-orbital on each carbon atom that does not contribute to bonding. Instead, the p-orbitals hybridise to form pi orbitals. The hexagonal graphene lattice results in an interesting electronic band structure for these pi orbitals. A unit cell on this lattice has two carbon atoms and each of these are part of a different sublattice, as shown in figure 2-3. When the energy bands of these sublattices cross, a conical dispersion relation forms, so graphene has a linear energy – momentum ($E-p$) relationship. This is quite unlike the parabolic band structure usual to most materials, described by:

$$E = \frac{p^2}{2m^*}$$

Equation 2-1

where m* is the effective mass of the electrons (in the conduction band) or holes (in the valence band). The linear relationship of graphene implies there is no relationship of the band structure to particle mass, i.e. the particles are effectively massless. Such massless behaviour is described by relativistic physics, which is used to describe the $E-p$ relationship of graphene[147] as $E = v_F p$ where v_F is the Fermi velocity of the electrons, which is equal to ~ 1 x 10^6 m/s in graphene[148]. Such a high velocity renders single crystals of graphene theoretically highly electrically conductive.

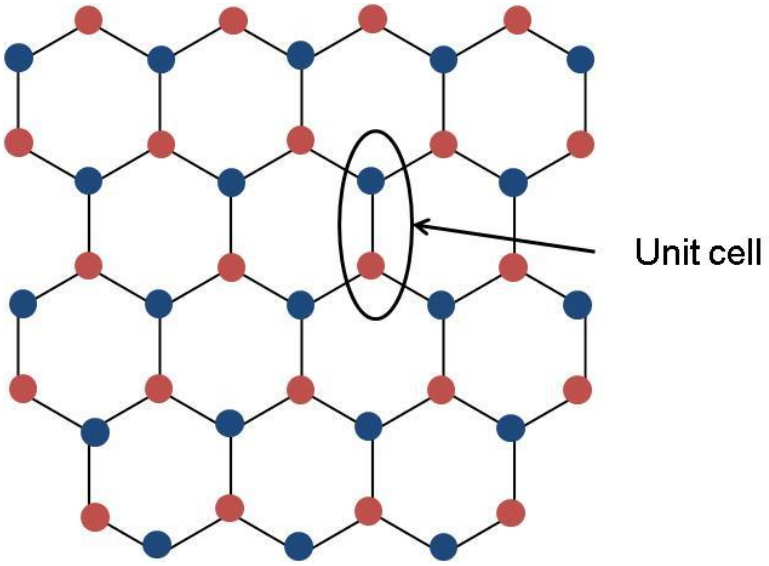

Figure 2-3: Chemical structure of graphene. All circles represent carbon atoms but each colour shows a separate sublattice.

Despite these promising properties, the use of graphene as an electrode is not yet perfect. The main drawback is the inability to manufacture a defect-free graphene sheet. Current manufacturing methods can now produce 30-inch graphene sheets[149] but as sheets become larger, polycrystallinity of the graphene becomes more unavoidable[150,151], with other defects possible during transferral of the graphene sheet to the desired substrate[152].The grain boundaries between the crystals place a limit upon charge mobility with monolayer graphene often having sheet resistances of hundreds of Ω/square[149,153], which is much higher than that of ITO[120].

There have been attempts to reduce sheet resistance. A simple method is to use multilayer graphene sheets[149], so inter-sheet charge transport is possible. Unfortunately, such a step lowers the optical transparency. Also, with more graphene sheets, the band structure tends towards that of bulk graphite but for less than ten graphene sheets an intermediate state remains, and this material is still described as graphene[154].

Another method to improve conductivity is to dope the graphene sheets. Substitutional doping is one method, but using susbtitutional atoms to change the structure of graphene can weaken graphene's enhanced electronic properties[155]. A way to solve this is to use materials which do not chemically interact with the graphene but act as an electron acceptor or donor [156,157]. Although the addition of any other species reduces the graphene transmittance, sheet resistance improvements more than compensate for this, with sheet resistance reductions of up to 70%[149,156,158].

The study in chapter 6 is the first test of graphene as the transparent electrode with a squaraine/ C_{70} heterojunction solar cell. For these preliminary investigations, no multilayering or doping of the graphene was undertaken, but it would be worth considering for future applications. Squaraine/ C_{70} is an up-and-coming organic solar cell combination, with the two materials absorbing across the whole visible spectrum between them[159] and squaraine being an excellent photon absorber.

To be a suitable electrode in this system, graphene must also have a work function that enables charge extraction and maintains a high open circuit voltage. The graphene is positioned in contact with the squaraine, for which it is used as the hole-transporting electrode. The work function of graphene is reported to be at around -4.4 eV from the vacuum level[160], whilst the HOMO of squaraine is around -5.3 eV[161]. Thus graphene might reduce the voltage a little, especially in comparison to the preceding electrode, ITO, which has a deeper work function. To combat this, studies are also performed with the hole transport layer, MoO_3, which has a work function aligned to the HOMO of squaraine[162] and which has already been shown to improve the properties of graphene-based solar cells[150].

3. Optoelectronic characterisation methods

3.1 UV-VIS Absorbance Measurements

Absorbance measurements were used in this thesis to identify which wavelengths of light were absorbed in solutions of semiconductor material, thin films, electrodes and entire devices. As well as then being able to determine the transmissivity of a solar cell component, the spectral information revealed the energies of the electronic transitions in a device.

Measurements were performed in a Cary 5000 UV-VIS spectrometer. Light was provided from a deuterium or a tungsten halogen lamp, depending on the wavelength of light required. The beam passed through a monochromator before splitting into two beams. One beam travelled through the sample and the other beam shone through a blank reference sample. The reference sample was either an empty cuvette, if solution absorption was being measured, or a blank substrate, if solid films were being measured. These beams were detected by the same machine, with their ratio giving the transmission through the sample. This setup is shown in figure 3-1.

Software that comes with the machine presented both transmittance and absorbance spectra. Absorbance (Abs) and transmittance (Tr) are related to the input light intensity (I_0) and detected light (I) via equation 3-1

$$\text{Abs} = -\log_{10}\left(\frac{I}{I_0}\right) = -\log_{10}(\text{Tr})$$

Equation 3-1

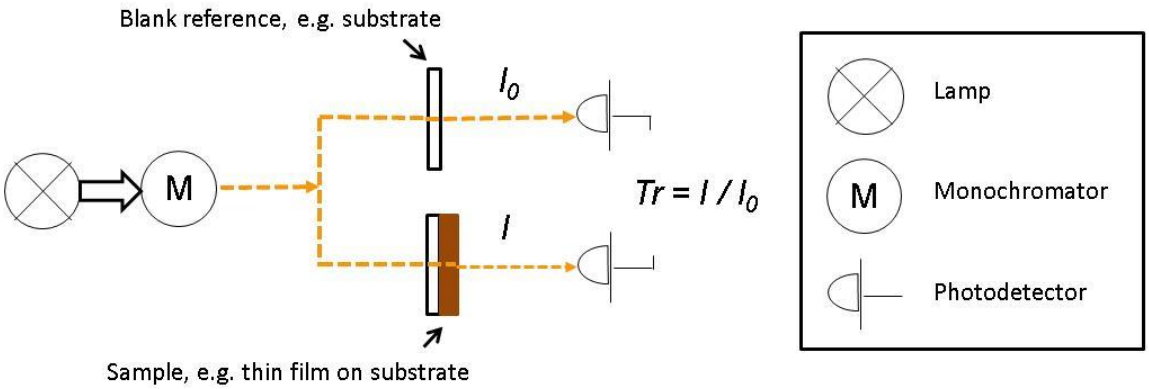

Figure 3-1: Schematic diagram of the absorbance spectroscopy setup

3.2 Electroreflectance

The GaAs-based samples of chapter 4 have opaque copper substrates, so transmission is not a possible method to investigate the electronic transitions in the solar cells. Reflectance spectroscopy could be used instead. In this technique, light is incident on the sample at a non-normal angle, so the reflected beam can be detected with a separate detector. Comparing the intensity of reflected light with that of the incident light reveals which wavelengths of light were absorbed and with what strength. However, for samples with low levels of absorption, simple reflectance might not offer suitable resolution[163]. A better method is to use the modulation spectroscopy technique of electroreflectance.

In electroreflectance, a modulating electric field is imposed onto a semiconductor sample. This electric field accelerates charges within the material, so the dielectric function changes with the electric field. This can be observed via a change in reflection (ΔR) of light. ΔR is greatest at photon energies close to energies of electronic transitions, as the modulation induces an alternating subduing or intensifying of the transition. This feature is the reason why modulation spectroscopy is an ideal technique for probing electronic transitions with greater resolution than standard reflectance spectroscopy[163]. On a graph, usually the normalised change in sample reflectance ($\Delta R/R$) is displayed.

To determine the energy of the electronic transition from the lineshapes, the Aspnes three-point method was used[164], which was designed to simplify the curve-fitting procedure. Taking two adjacent peaks around a transition, where E_A is the energetic position of the lower energy one and E_B is the energetic position of the higher energy one (figure 3-2), the exact transition energy (E_g) can be found according to equation 3-2.

$$E_g = E_A + (E_B - E_A)f(\rho)$$

Equation 3-2

where ρ is the ratio of peak heights ($\Delta R_B/\Delta R_A$) and $f(\rho)$ is a scaling factor that varies according to whether the critical point is 2D, 3D or excitonic, however the scaling factor only varies slightly between the different critical points, so the outcome will be almost invariant of the physical model used to represent the transition. This method gives a very good estimate of the transition energy and is widely used[165,166].

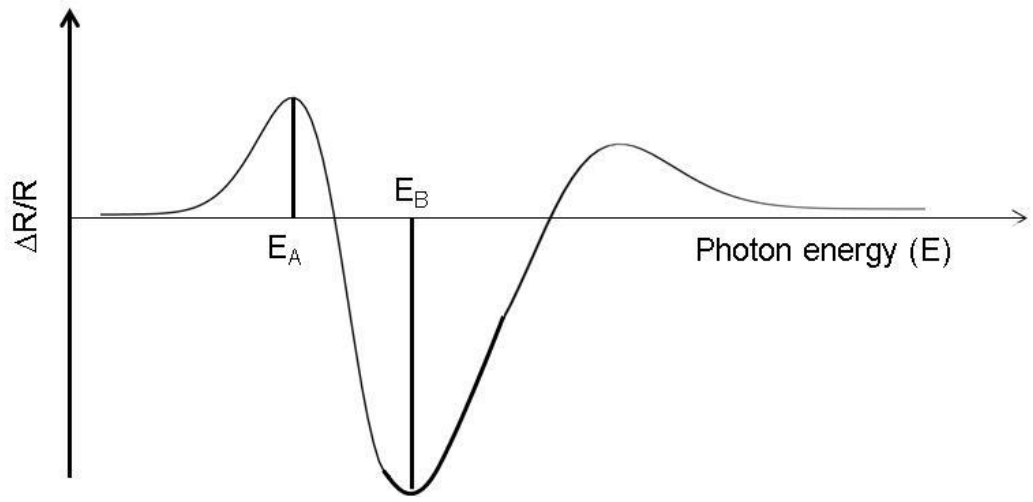

Figure 3-2: Example electroreflectance spectrum with a characteristic lineshape around an electronic transition

There are other features in the spectra besides those caused by electronic transitions. Although these will not be studied here, they are mentioned for reference. At the low energy side of a transition lineshape can appear 'low energy interference oscillations', which were studied by Blume et al.[167]. They determined that these oscillations originate in optical interference. At the higher

energy side of the transition are Franz-Keldysh oscillations. These arise because the change in dielectric function is proportional to Airy-function, which is oscillatory when the electric field interacts with the continuum of energy states in the energy bands but decays for energies lower than the band gap[163].

3.2.1 Experimental setup

Electroreflectance measurements were taken with a setup built by myself, the schematic of which is shown in figure 3-3. The samples were held in an Oxford Instruments nitrogen vacuum cryostat, as temperature-varying measurements were taken. Details of the temperature control can be found in section 3.6. A successful test of the setup was performed at room temperature on a crystalline GaAs film before use in the experiments in chapter 4,

The modulating electric field was applied to the samples with an Agilent 33210A function generator. The amplitude of ΔR is proportional to the applied modulating field[168,169]. For this work I chose an amplitude of 0.4 V, which was large enough to induce a sizeable response but not so large to move the solar cell too far from equilibrium.

The sample was illuminated at an angle of 45 degrees by focussed light from a quartz tungsten halogen lamp passing through an Oriel Cornerstone 130 1/8m monochromator. Longpass filters were used to remove second harmonics of the incoming light. The reflected beam from the sample was detected by a Newport 918 IR germanium photodetector.

To measure the change in reflectance, ΔR, a Princeton Applied Research 5210 lock-in amplifier (LIA) was used. The LIA was used because it can detect very small signals, and ΔR is often no more than thousandths the value of reflectance, R, for III-V materials[170–172]. Into the LIA were fed both the output from the Newport photodetector (i.e. the modulating reflectance signal) and a reference signal from the Agilent function generator, which modulated at the same frequency as the applied

electric field. These two signals were then multiplied together and integrated over a few milliseconds, with the integration output by the lock-in amplifier. The integration of any two signals that modulate in phase will be a constant value proportional to the amplitude of the signal, i.e. proportional to ΔR. If the two signals have different frequencies then the integration will be near zero.

To aid detection of this signal, the frequency of the applied field was picked to be distinct from electrical noise caused by mains power (which has as frequency of 50 Hz) and its harmonics. I found that a frequency of 277 Hz gave a good signal. Furthermore, an electrical bandpass filter around the 277 Hz reference signal and a mains power frequency filter at 50 Hz were switched on in the lock-in amplifier to help prevent noise. In addition, the setup was shielded with metal sheets to further reduce the likelihood of interference from surrounding electrical equipment. Before any readings were taken, the lock-in amplifier was tuned to make the reference signal in phase with the reflectance signal, to give the maximum output signal. Tuning was performed with the wavelength of input light set to excite the band gap of the GaAs, where the greatest ΔR response would be found[173]. The output signal of the lock-in amplifier was fed into a computer, where a custom-built LabVIEW program both controlled the monochromator and recorded the output signal at each wavelength.

As the signal $\Delta R/R$ is required, standard reflectance measurements were taken to record the 'R' component for each temperature used. This was performed by feeding the output of the photodetector directly into a Keithley 6485 picoammeter.

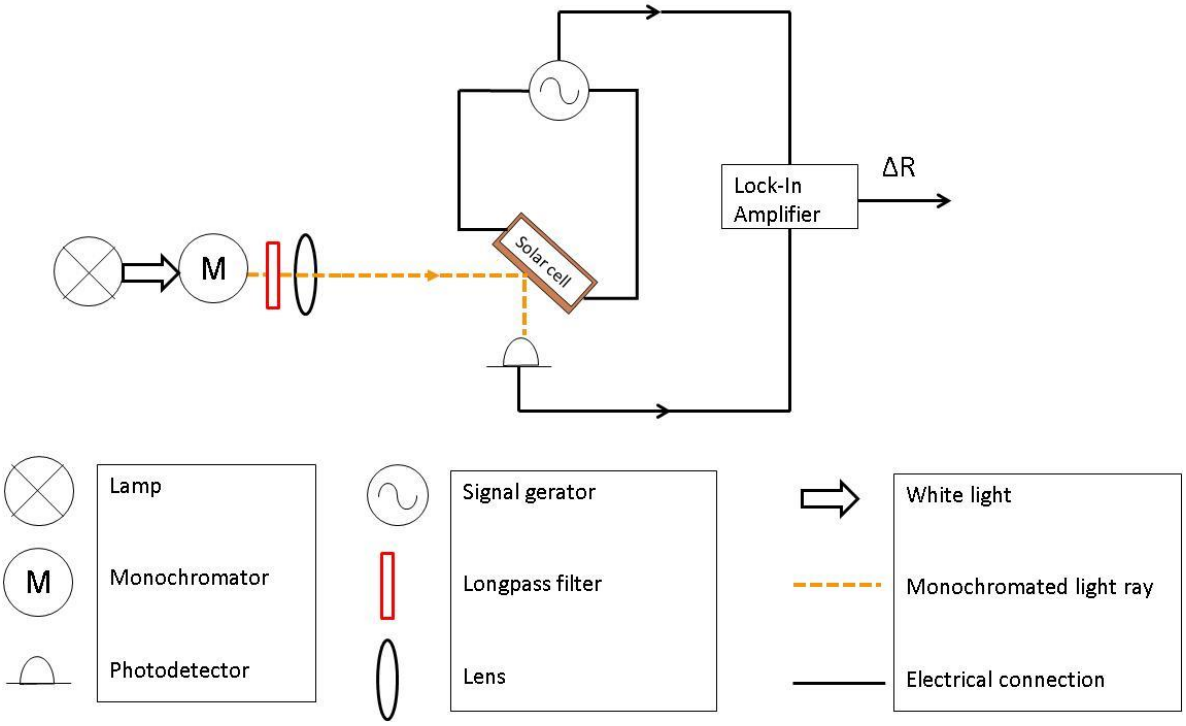

Figure 3-3 Schematic of the setup used to measure the change in reflectance upon applying a modulating bias.

3.3 Current density-voltage measurements

Current density-voltage (JV) measurements taken under solar illumination are used to determine the power conversion efficiency (PCE) of solar cells and thus this technique is one of the principal characterisation methods. As explained in section 1.2.4, the PCE is calculated from parameters that can be determined by a JV curve, namely open circuit voltage (V_{oc}), short circuit current density (J_{sc}) and fill factor (FF), and the input power density (P_{in}) (equation 3-3):

$$PCE = \frac{J_{sc}\, V_{oc}\, FF}{P_{in}}$$

Equation 3-3

Other parameters that can be obtained from a JV curve are the parasitic resistances through a device: series resistance and shunt resistance, which impact upon the other parameters.

JV measurements taken in the dark are equally as important as those taken under illumination, as from these, the diode ideality factor (n) and the dark saturation current density (J_0) are obtained, which provide information on charge recombination within devices.

3.3.1 Experimental Setup

For illuminated JV measurements, a Newport 67005 solar simulator illuminated the solar cells with a spectral range of AM1.5 and power of 100 W/cm^2, as measured with a Thorlabs D3MM power meter. The lamp was allowed half an hour to warm up before testing began. During testing, the colloidal quantum dot cells and organic cells of chapters 5 and 6 were mounted in a sample holder that allowed nitrogen to be flushed through, to reduce any possible degradation by air. The GaAs-based samples were mounted in a custom-built, electrically-shielded holder for use in ambient conditions. All devices were connected to a Keithley 2400 source-measure unit (SMU), which in turn was connected to a LabVIEW program which controlled the input voltage across the solar cell and measured its current output. Devices were tested from -0.5 V to +1 V in step sizes of at most 0.05 V.

For dark JV measurements, the front of the testing holder is covered to block all light. When any intensities between dark and full illumination were required, ND Melles Griot neutral density filters were placed in front of the solar simulator.

3.3.2 Solar cell parameter extraction

The LabVIEW program used to run the JV measurement also produced a document of current and voltage values. These were copied into an Excel spreadsheet that identified the J_{sc} and V_{OC} values and calculated the fill factor and power conversion efficiency.

Series and shunt resistances cause slopes in the JV curve, as illustrated in figure 3-4. They are found by taking the derivative of the curve at $V=V_{oc}$ and V=0, respectively then applying the approximations given in equations 3-4 and 3-5.

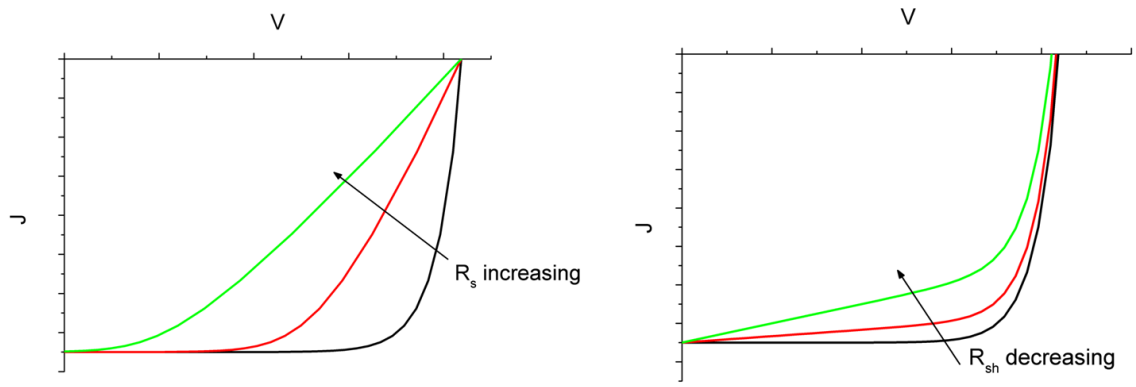

Figure 3-4: Effects of series resistance (R_s) and shunt resistance (R_{sh}) on JV curves

$$\frac{1}{R_s} \approx \left.\frac{dJ}{dV}\right|_{V=V_{oc}}$$

Equation 3-4

$$\frac{1}{R_{sh}} \approx \left.\frac{dJ}{dV}\right|_{V=0}$$

Equation 3-5

The derivation of this result is described in *The Physics of Solar Cells*[174]. The error values for R_s and R_{sh} in this thesis derive from the precision in calculating the differential of the curve at $V=V_{OC}$ and V=0. The error value obtained depends on how smooth the data points are. For this reason the error is given as the difference between the values of R_{sh} and R_s at the data points at 0.05 V either side of the relevant bias.

To obtain the ideality factor (n) and reverse saturation current (J_0) from dark JV curves, the software 'Origin' was used to perform a fit to the diode equation (equation 3-6). This equation is not

complete; the full form takes parasitic resistances into account. However, these dominate the curve only at low biases (shunt resistance) and high biases (series resistance) so, for the fit, only the exponential portion of the curve is used, where it is assumed the parasitic resistances have negligible effect. Errors given in this thesis for values of J_0 and n are those calculated as fitting errors by Origin.

$$J_{dark} = J_0\left(e^{\frac{qV}{nk_BT}} - 1\right)$$

Equation 3-6

3.4 External quantum efficiency

External quantum efficiency (EQE) measurements determine which incident wavelengths of light are absorbed to create charges that contribute to the short-circuit current. EQE is defined as in equation 3-7 and is the ratio of the number of charge carriers extracted from the solar cell to the number of photons incident upon the solar cell, all as a function of photon wavelength (λ).

$$EQE(\lambda) = \frac{charges\ extracted}{photons\ input} = \frac{current}{\#\ photons/second}$$

Equation 3-7

3.4.1 Experimental setup

To perform this experiment, I built a setup as shown in the schematic of figure 3.5. The light source for the EQE measurements was a tungsten halogen lamp, which was fed into an Oriel Cornerstone 130 1/8m monochromator. Long pass filters of 400 nm, 610 nm and 1000 nm were used to block second harmonics of light when the sample was exposed to light of long wavelengths. The lamp was allowed at least half an hour to warm up before any measurements were taken. This was found to be long enough to produce a stable current output from a GaAs solar cell. To measure the input

number of photons per second, the light was passed through any windows that the samples would be behind in their testing holders, and was sensed by a Newport 818UV silicon photodetector for the visible range and a Newport 918IR germanium photodetector for the IR range. The photodetector output was detected by a Keithley 6485 picoammeter. The measured output current was adjusted for detector spectral sensitivity (this data obtained from the manufacturer) before calculating the number of output photons per second at each wavelength.

Samples are held in the same testing holders as used for JV measurements, with nitrogen purging through for the PbS and organic solar cells (chapters 5 and 6). A lens was used to focus the light from the monochromator onto the cell, with the current output of the cell monitored during alignment to ensure optimum positioning. The setup is given in figure 3-5. The current output of the solar cell at each wavelength of light was recorded by a Keithley 6485 picoammeter. After each wavelength step, a pause of 0.1 s was taken before three successive current readings were taken. The pause ensures that the system has settled at that wavelength. The three current readings are then averaged to reduce the effects of noise. A custom-built LabVIEW program is used to run the monochromator, collect the picoammeter readings, perform the averaging and output the results. The total integrated area under the EQE spectrum, calibrated to the solar spectrum, gives the short circuit current, which can be compared to the value obtained from JV measurements as a check of the setup.

3.4.2 External quantum efficiency as a function of voltage

In chapter 6, a voltage was applied to a solar cell whilst EQE measurements were being performed. This technique is helpful to determine how different electric fields in the device affect the current output.

For these measurements, the Keithley 6485 picoammeter was replaced by the Keithley 2400 SMU (as used for JV measurements). The SMU has the advantage of being able to apply a bias concurrently with recording current. Although the SMU does not have the precision of the picoammeter, it was found that large enough currents were obtained for this not to be a problem. As forward bias increased it was noticed that the current output of the cells took increasingly longer to stabilise. Current output as a function of time was recorded to identify the stabilisation time for each bias.

3.4.3 External quantum efficiency with additional infrared light source

In chapter 4, EQE was performed with an additional infrared light source, to try to determine whether an infrared photon transition was producing current. It was carried out in the same way as a standard EQE measurement with two modifications**.** Firstly the EQE light source was dimmed with a neutral density filter of optical density 3.0, to prevent there being enough photons to induce all the infrared transitions as well. Secondly, a xenon lamp was added (Cermax Xenon Fiberoptic Lightsource) with the light passed through an infrared longpass filter (at 1350 nm) to provide the extra IR light. The setup is shown in figure 3-5.

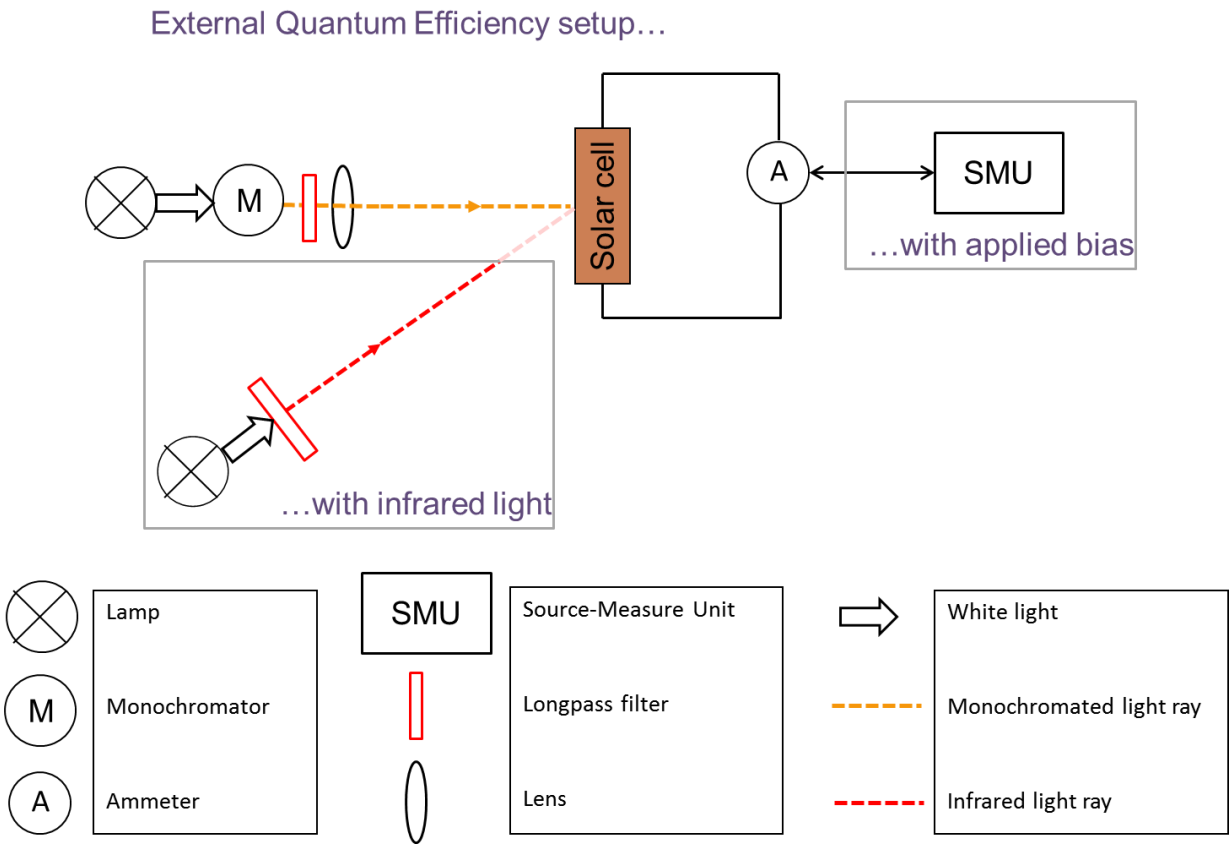

Figure 3-5: Diagram of the setup of the external quantum efficiency measurements. The sections in grey boxes give the extended EQE experiments, specifically, EQE as a function of voltage and EQE with additional infrared light.

3.5 Photoluminescence

Photoluminescence (PL) is a technique used to identify wavelength spread and intensity of radiative recombination in semiconductors.

3.5.1 Experimental setup

GaAs samples were illuminated by a 632 nm HeNe laser of 15 mW power and PbS samples were illuminated with a 405 nm laser with power rating < 10 mW. Both of these had a much higher photon energy than the transitions of interest so could easily excite them.

Samples were placed at an angle to the laser and the spectrometer. The spectrometer used was a Princeton Instruments 'Acton SP2300' model. This was attached to a Princeton Instruments Pixis 100 CCD detector. The slit width of the spectrometer aperture was optimised. A greater slit width gives higher signal, yet too high a signal was seen to saturate the detector. The wider slit also reduces the resolution of the spectrum: I observed that the full-width half-maximum of indium arsenide quantum dot emission was 10 % larger when the slit was fully open compared to when it was 1/10 the width. Optimisation also occurred for the acquisition time: too long an acquisition time could saturate the detector but the greater acquisition time gives less noisy results. Once the ideal slit width/ acquisition time combination was chosen, these values were kept the same for all the experiments which would be compared to each other. It was ensured that the same distance to the detector and laser and same angles between all components were used for each complete set of data. Measurements were performed to test the effect of sample angle on photoluminescence and variations of ± 10 nm were seen if the angle changed ± 10 degrees about its optimum point. For temperature-dependent measurements samples were kept in a nitrogen vacuum cryostat held at a fixed position. For samples not kept in the cryostat, a protractor that was fixed to the optical bench was used to check that sample angle was constant. These samples were usually held in air during the experiments, after storage in a nitrogen atmosphere. The setup is shown in figure 3-6. The spectra take a couple of minutes each (to set up and run) with no evidence of sample degradation in that time for PbS. Degradation of quantum dots via oxidation would manifest itself as a blueshift in PL emission over time as the effective quantum dot size would decrease[175]. Films of PbS with1,2-ethanedithiol ligands showed no blueshift after 20 minutes air exposure. Degradation was not an issue for the GaAs samples.

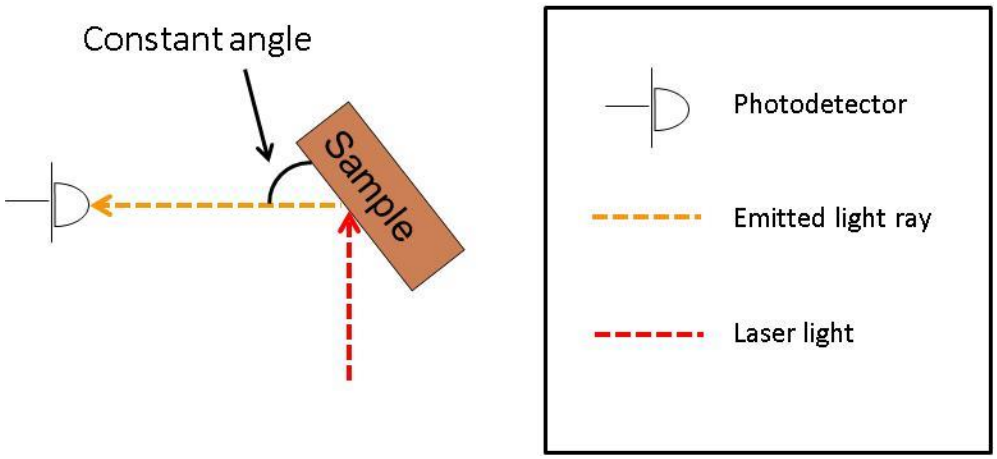

Figure 3-6: Setup of the photoluminescence experiment

3.6 Temperature-dependent measurements

Various low-temperature measurements were performed in chapter 4. There were various reasons for this, including examining the charge escape mechanism and utilising the fact that low temperatures give sharper spectra, as thermal broadening is reduced.

For all temperature dependent measurements (ER, EQE and PL), samples were placed in an Oxford Instruments nitrogen vacuum cryostat with windows allowing optical access to the sample and electrical connections in place. This was controlled by an Oxford Instruments ITC 502 temperature controller. The cryostat was cooled to its minimum temperature (77K) and held at this temperature for an hour before being topped up with liquid nitrogen in preparation for the run of temperature measurements, which were always taken from cold to hot as this produces more stable and accurate temperatures. At each temperature the cryostat was held for ten minutes after the temperature was set, to ensure correct temperature was reached.

3.7 Capacitance-voltage measurements

Capacitance-voltage measurements were used (chapter 4) to identify the biases at which charge accumulation and charge release occurred in quantum dot states. The capacitance of the devices was evaluated by modelling them on parallel plate capacitors, with the active layer being the dielectric and the electrodes representing the metal plates. With this representation, capacitance, C, is given by equation 3-8, where Q is the stored charge and V is the potential difference between the electrodes:

$$C = \frac{dQ}{dV}$$

Equation 3-8

The capacitance was measured across a series of applied biases from -2 V to +2 V. The capacitance was determined from current and voltage measurements, as now explained. A small modulating voltage is applied to the sample ($V_0 \sin(\omega t)$) where V_0 is the amplitude of modulation, ω is the modulation frequency and t is time. This induces a change in current in the diode ($I_0 \sin(\omega t + \varphi)$) where I_0 is the amplitude of the current and φ is the phase shift from the perturbing signal. Applying a bias to a diode gives an exponential current response (as seen in JV curves). However, CV analysis relies on linearity. Thus, V_0 was kept small (25 mV) to ensure a linear approximation to the current response. The modulating frequency was chosen so that all carriers could respond to the perturbation. 5 kHz was used, which is within the standard range used for probing charging and discharging in InAs QDs[176,177]. The sinusoidal voltage and current give the complex impedance, Z, according to equation 3-9:

$$Z = \frac{V_0 \sin(\omega t)}{I_0 \sin(\omega t + \varphi)}$$

Equation 3-9

From this, the capacitance is calculated via equation 3-10:

$$Z = \frac{1}{i\omega C}$$

Equation 3-10

CV measurements were taken on an Agilent E4980A option 001 Precision LCR Meter. This instrument both applied the modulating bias and then measured the responding current. A LabVIEW program was used to control measurements, record readings and calculate capacitance. Samples were kept in the dark under ambient conditions, in the same sample holder used for JV and EQE measurements.

4. AlAs/InAs/ GaAs quantum dot intermediate band solar cells

4.1 Introduction

Intermediate band solar cells (IBSCs) have an electronic band between the valence band and conduction band. This extends the range of photon energies that can be absorbed (see figure 4-1) and theoretically raises the Shockley-Queisser efficiency limit from 40.7%, for a single junction solar cell, to 63.1%[50].

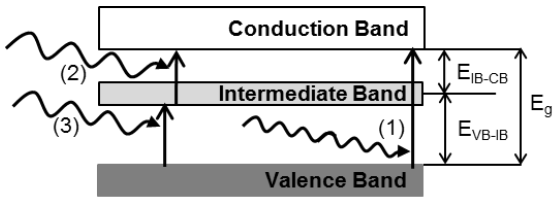

Figure 4-1: Schematic band structure of an intermediate band solar cell (IBSC) of bulk band gap Eg. As well as valence band (VB) – conduction band (CB) photon absorption (1), photons of energy less than Eg can be used in a two-step process ((2) and (3)) to generate current. These low energy photons must have energy greater than E_{VB-IB} to promote an electron to the intermediate band and energy greater than E_{IB-CB} to promote an electron to the conduction band.

In 2000, Marti et al.[53] proposed that an array of discrete quantum dot (QD) energy levels embedded in the intrinsic region of a wider band gap p-i-n solar cell could potentially form an intermediate energy band (figure 4-2A). To date, QD IBSCs have performed worse than their p-i-n counterparts devoid of quantum structures, due mainly to a reduction in open circuit voltage, V_{OC}. How the quantum dots interact with the energy bands of the bulk host material is key to controlling V_{OC}. V_{OC} is determined by the difference between the bulk electron and hole quasi-Fermi levels[22], E_{Fe} and E_{Fh} (figure 4-2A). As shown in figure 4-2B, electronic states can form between the intermediate band and host material energy bands. The presence of these "ladder states" leads to Fermi level pinning of E_{Fe} to the quasi-Fermi level of the intermediate band, E_{FIB}, as charge populations of the host and quantum dots can now interact via thermalisation of carriers[178,179] or tunnelling[54,180].

The aim of the work in this chapter is to assess whether the QDs can be electrically isolated from the host by inserting a wide band gap semiconductor between them. Indium arsenide (InAs) QDs embedded in a gallium arsenide (GaAs) p-i-n solar cell are used to test this hypothesis. The quantum confinement in the InAs QDs increases the band gap to ~1.1 eV from the bulk value of 0.37 eV[181]. GaAs has a band gap of 1.42 eV[182]. The wide band gap barrier material is aluminium arsenide (AlAs), which has a band gap of 2.16 eV[182]. The proposed band diagram is shown in figure 4-2C.

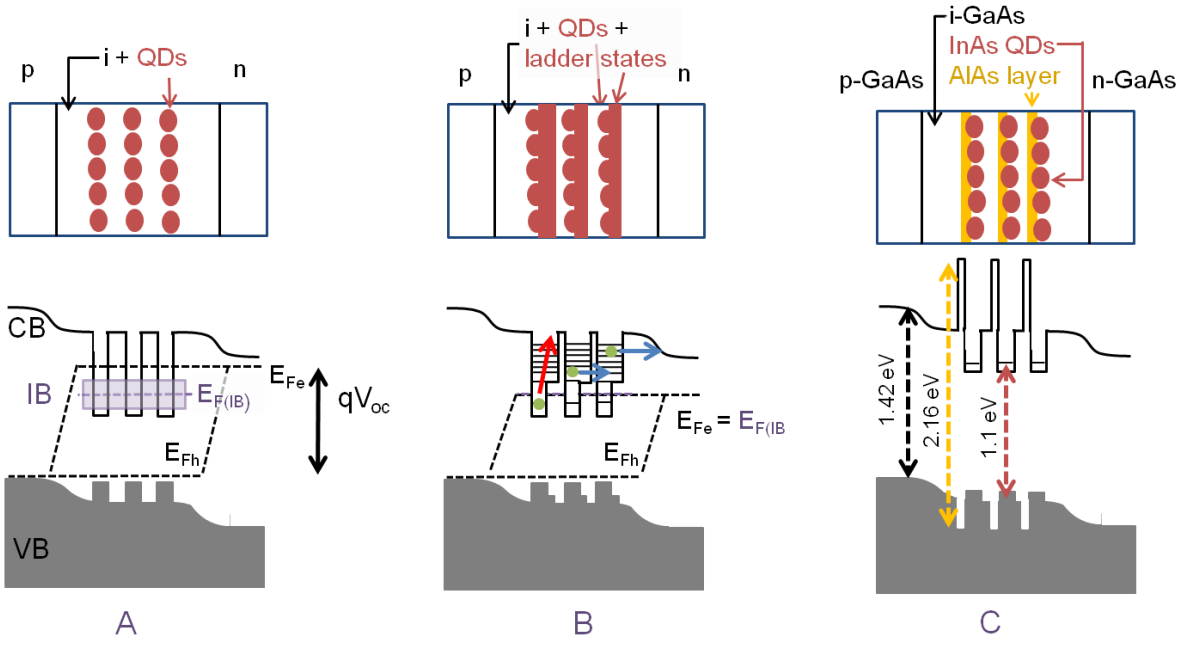

Figure 4-2: Schematic energy level diagrams of QDs within a p-i-n device with sketches of the corresponding p-i-n cell structures on the top row. A: Quantum dots forming an intermediate band (IB) between the conduction band (CB) and the valence band (VB) of the host material. Quasi Fermi levels of electrons (EF_e), holes (EF_h) and the IB (EF_{IB}) are shown. B: Quantum dots with ladder states. This causes thermal escape (red arrow) and tunnel escape (blue arrows) of electrons to the CB, which pins EF_e to EF_{IB} and reducing V_{OC}. C: InAs quantum dots covered with wide band gap AlAs in a GaAs p-i-n solar cell.

The AlAs addition is thought to have two potential benefits. Firstly, it has been seen to prevent the intermixing of indium and gallium at the quantum dot edge[81,83]. Such regions of InGaAs would be a cause of ladder states. Secondly, the wide band gap nature of AlAs might present an electronic barrier to charge carriers[54,183], isolating the intermediate band.

In this chapter, the origins of the efficiency difference of devices with and without the AlAs barrier are investigated. Variations in short circuit current are examined first, using electroabsorption and external quantum efficiency techniques. Next, the question of whether an isolated intermediate band forms in the device will be considered by testing possible quantum dot charge escape mechanisms: optical, thermal and tunnelling. Finally, changes in recombination in the cell as a result of the AlAs capping layer will be examined using dark current-voltage, capacitance-voltage and photocurrent-voltage measurements.

4.2 Devices

All p-i-n materials were fabricated by Mr Frank Tutu and Dr Hiuyun Liu at University College London. Devices were processed by Dr Ian Sellers of Sharp Laboratories of Europe. Subsequent characterisation was performed by the author unless explicitly stated.

Two types of device were grown for this study: a reference InAs QD/ GaAs device termed the 'control cell' and a device with AlAs capping layers, termed the 'AlAs cell'. In all respects other than the inclusion of the capping layer in the AlAs cell, both devices were identical. Both types of device were made with twenty InAs QD layers within the intrinsic layer of the GaAs p-i-n device. InAs is deposited onto GaAs using molecular beam epitaxy (MBE). As InAs and GaAs are lattice mismatched, strain builds up and after a wetting layer of InAs is created[84], the InAs self-assembles to form quantum dots. This strain-driven self-assembly process is termed Stranski-Krastanov growth[66]. AFM analysis by Frank Tutu suggested that the InAs QDs in the AlAs cell have a diameter of 46 nm, are 10 nm high and are packed to a density of 4.8×10^{10} cm^{-2}. In the case of the control cell, a GaAs spacer layer is directly deposited onto each layer of InAs QDs. The GaAs induces further strain imbalance and is found to induce significant indium and gallium intermixing resulting in the wetting layer and edges of dots consisting of InGaAs[84]. For the AlAs cell, 2 ML (~0.57 nm) of AlAs is deposited onto

each quantum dot layer before this GaAs spacer. The structure of the devices is illustrated in figure 4-3.

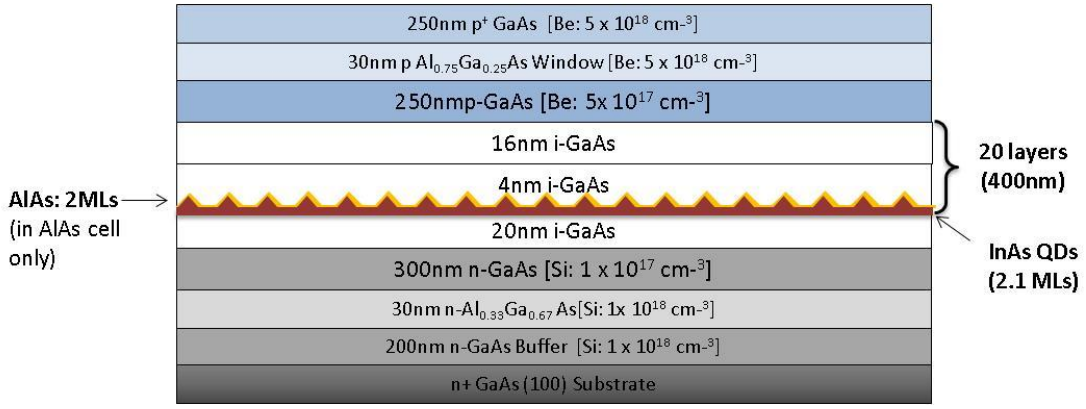

Figure 4-3: Device structure, giving thicknesses, doping information and the position of the AlAs layer in the case of the AlAs cell. Estimates of dot dimensions are given in the text.

4.3 Results

4.3.1 Device performance (Illuminated JV results)

Current density – voltage (JV) measurements were taken under AM 1.5 solar illumination to assess the effect of the AlAs layer on device performance. The JV curves and efficiency parameters calculated from the curve are shown in figure 4-4. An explanation of how the parameters were calculated can be found in section 1.2.4 .

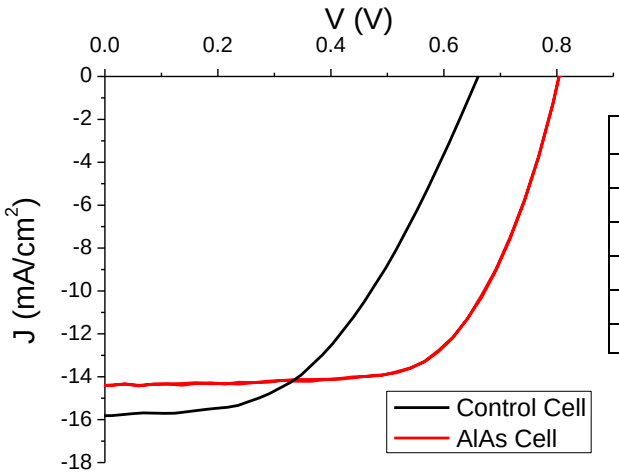

	Control	AlAs
J_{sc} (mA/cm^2)	15.70 ± 0.05	14.35 ± 0.15
V_{oc} (V)	0.66 ± 0.01	0.80 ± 0.01
Fill Factor (%)	48 ± 2	58 ± 3
PCE (%)	5.1 ± 0.1	6.5 ± 0.2
R_s(kΩ.cm^2)	0.016 ± 0.001	0.009 ± 0.001
R_{sh} (kΩ.cm^2)	0.91 ± 0.08	1.57 ± 0.15

Figure 4-4: Current Density – Voltage (JV) curves at AM 1.5 illumination for the control cell and the AlAs cell. The table gives the efficiency parameters, with errors being the standard deviation across three repeated measurements, and the parasitic resistances, with errors as explained in section 3.3.2.

The most striking difference between the two curves is that the open circuit voltage (V_{OC}) is much higher for the AlAs cell than that of the control cell. The fill factor (FF) is also increased. Its improvement appears to be a consequence of both lower series resistance (R_S) and higher shunt resistance (R_{sh}). Unfortunately, the presence of the AlAs layer is detrimental to the short circuit current (J_{sc}), yet overall the AlAs has a positive impact on the power conversion efficiency (PCE).

The high parasitic current losses will not only decrease the FF but high R_s can reduce J_{sc} and low R_{sh} can reduce V_{OC}[184]. Thus it could be that the higher shunt resistance of the AlAs cell is acting to increase the V_{OC}. Dislocations in the structure have been shown to lead to low shunt resistance[185,186]. Dislocations are known to form in InAs/GaAs solar cells when strain becomes too great upon building up progressive InAs QD layers[72]. Thus a difference in dislocations gives one possible structural explanation for the difference in resistances between the two devices.

As the aim of the AlAs layers is to increase open circuit voltage, V_{oc}, most of the chapter (sections 4.3.3 and 4.3.4) will be devoted to this aspect of the performance change, starting by examining whether quasi-Fermi level pinning between the intermediate band and conduction band has been demonstrated. This will reveal itself if charges from the quantum dots escape to the GaAs bands via

thermal or tunnelling means rather than by optical excitation. The quasi-Fermi difference at open circuit is be influenced by the rate and mechanisms of recombination in the cell, which are reflected in dark JV measurements examined in section 4.3.4.

Firstly, however, the difference in J_{sc} is discussed. The lower J_{sc} of the AlAs cell could be due to reduced absorption or lower charge extraction as a result of the presence of AlAs. This is investigated in section 4.3.2 using electroreflectance (ER) and external quantum efficiency (EQE) to provide a spectral map of transitions from which current originates and to understand the effect of AlAs upon charge extraction.

4.3.2 Origin of J_{sc}

In order to understand the impact of the AlAs layer on J_{sc}, the contributing factors to this parameter are investigated, namely charge generation and extraction.

4.3.2.1 Charge generation

As discussed in section 3.2 one of the reasons electroreflectance is used over simple reflectance measurements without a modulating bias, and the reason it is used here, is because electroreflectance offers a higher resolution of optoelectronic spectral features.

Within the spectral range of the setup it was possible to probe all of the theoretical optical transitions, except that between the intermediate band and conduction band, which is estimated to have an energy of about 0.2 eV (6200 nm), which is beyond the range of our system. The remaining transitions of the control cell can be identified in the low temperature spectra shown in figure 4-5.

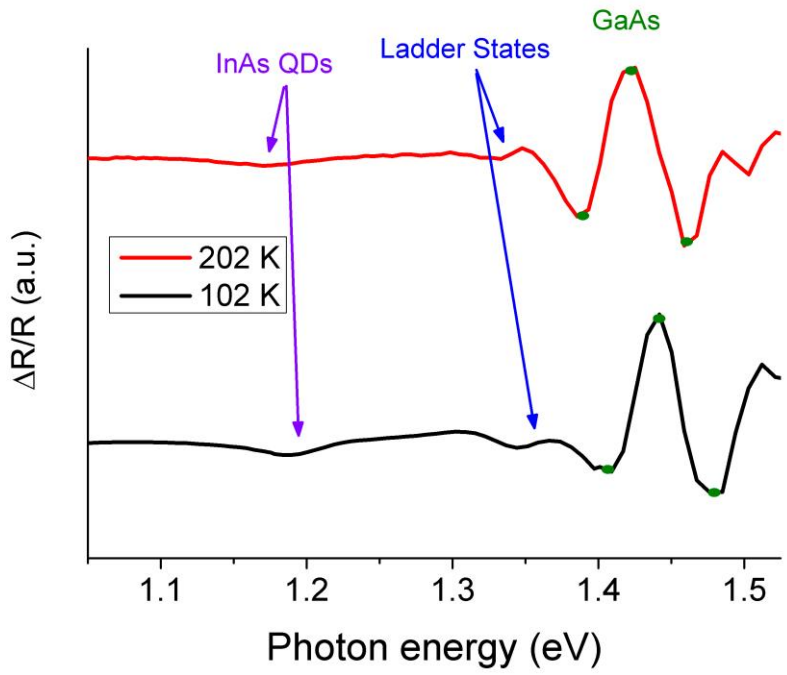

Figure 4-5: Electroreflectance spectra of the control cell, taken whilst the cell was held at temperatures of 102 K and 202 K. Possible optoelectronic transitions are identified on the graph. The green dots are the points used to calculate the position of the GaAs transition.

The most prominent feature in figure 4-5 is the GaAs transition, at 1.44 eV (102 K) and 1.42 eV (202 K). These positions were found using the Aspnes three point method[164], with the extrema used in the calculation shown on the graph as green dots. The room temperature spectrum places the GaAs transition at 1.40 eV (figure 4-6), confirming the trend that the transition redshifts as temperature increases. This is to be expected as the band gap narrows with temperature[187]. This is because thermal expansion of the GaAs increases the distance between atoms and, consequently, the potential between atoms decreases. As the band gap is proportional to this potential[187], the band gap decreases. The transition at around 1.34 eV can be assigned to ladder state transitions arising from an InGaAs alloy forming at the InAs surface[84]. At energies higher than the band gap are Franz-Keldysh oscillations, which are a manifestation of the electric field interacting with the continuum of states in the conduction band[188].

At lower energies (down to 0.9 eV at least; the spectra were cropped for presentation here), the spectra show oscillations, likened to the interference oscillations investigated by Blume[167]. These

occur whenever optical interference can occur between light reflected from different interfaces within the structure. The period of these oscillations gives the distance between the upper and lower reflecting surfaces[189]: this was calculated from both AlAs and control spectra and found to be around (940 ± 30) nm. Examination of the device structure (figure 4-3) reveals that this separation is valid for multiple pairs of interfaces in the devices. Another test of whether these oscillations are due to interference was to record control cell spectra taken at six angles of incidence from 37° to 62°, as the change in position of oscillation peaks and troughs for different angles reveals the refractive index[167,189] A refractive index of 3.45 ± 0.25 was obtained, which matches that of GaAs, suggesting that these oscillations are a result of interference.

Within this energy region is a trough at about 1.19 eV at 102 K and 1.17 eV at 202 K. Based on reports from similar systems[77,190,191], this is thought to be due to QD absorption, which is enhanced and narrowed at low temperatures because of a reduction in electron-phonon interaction at these temperatures.

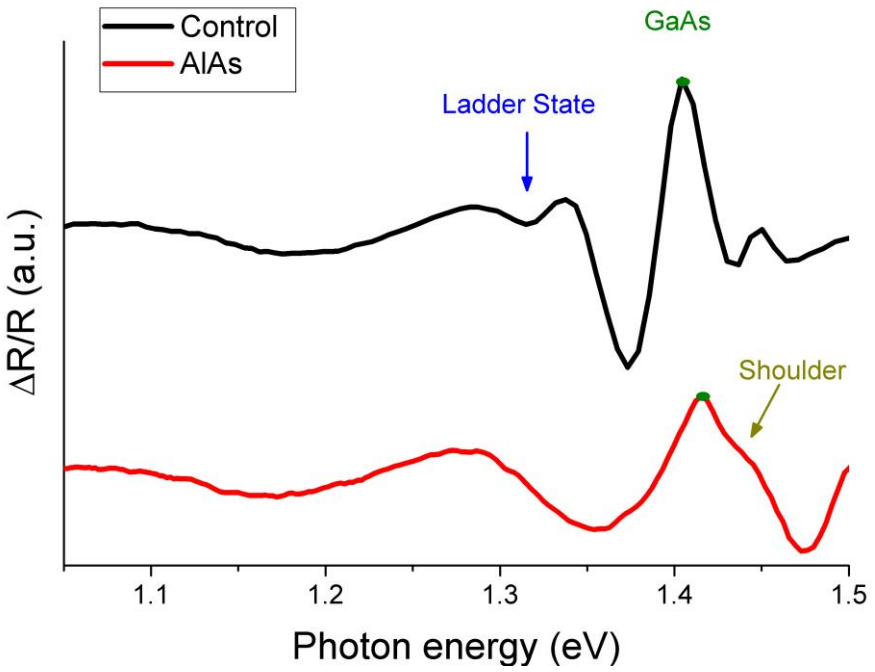

Figure 4-6: Electroreflectance of the control cell (black) and AlAs cell (red)

Comparing the room temperature spectra of the control cell with the AlAs cell (figure 4-6) the quantum dot transition is not seen in either: possibly it is too small, and/or it is swamped by the interference oscillations. The main GaAs transition is again shown by a green dot and is seen in both cells, as expected. The AlAs cell also has a "shoulder" at around 1.44 eV. There are two possible reasons for this. Either it is a convolution of the transition ER peaks with the Franz-Keldysh oscillations[192] or it is a manifestation of GaAs and AlAs interaction[85], which has been shown to arise from gallium and aluminium interdiffusion[193]. A ladder state transition is seen in the control cell as a trough at the beginning of the interference oscillation but this is not visible in the AlAs cell. The reduction in ladder states in the AlAs cell supports the hypothesis that AlAs has reduced In/ Ga intermixing and thus reduced InGaAs states. The impact of the reduced InGaAs states on current extraction becomes clearer when considered with external quantum efficiency measurements.

4.3.2.2 The effect of reduced InGaAs states on current output

External quantum efficiency (EQE) measurements spectrally map the short circuit current, so is ideal for determining the contribution from each part of the solar cell.

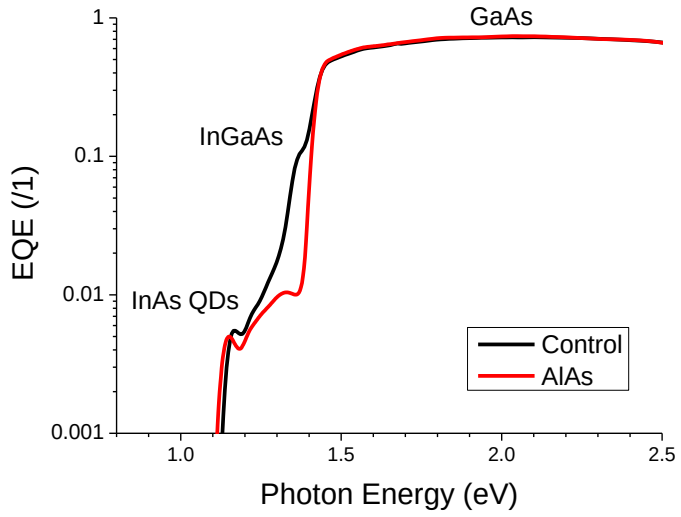

Figure 4-7: External quantum efficiency at 295 K for the control cell and the AlAs cell

The spectra in figure 4-7 can be divided into three distinct regions which correlate well with the transitions observed in the electroreflectance spectra:

1. Current from GaAs transitions at energies greater than 1.4 eV
2. InGaAs ladder state transitions between 1.2 and 1.4 eV
3. The transition across the QD energy gap between 1.1 and 1.2 eV.

The change in the ladder state region is most striking. Comparison of the integrated EQE of this region for both devices showed that the lower J_{sc} for the AlAs device is attributed almost entirely to the reduction in current from these ladder states. A suppression of current from these transitions was observed by Sablon et al. in a device containing InAs QDs with 1.2 nm thick AlGaAs barriers[80]. They argued that lower current was evidence that the energy barrier was impeding charge extraction, yet current from QDs was not always suppressed. In the data presented in figure 4-7 the QD EQE of the AlAs cell is 89% that of the control cell, suggesting that the AlAs barriers do little to inhibit charge extraction. Instead, as shown by the electroreflectance, there is a reduction in InGaAs current because there is less InGaAs.

In support of this argument, the quantum dot peak for the AlAs is redshifted compared with that of the control cell. This infers that the AlAs has reduced GaAs/InAs intermixing, as purer InAs quantum dots (with less intermixed gallium) would have a band gap further from that of GaAs, i.e. it would redshift[81,191]. In opposition to this, the AlAs energy barrier can work to induce more confinement in the quantum dot, which would result in a blue-shift of the quantum dot peak[81,183,194]. This confinement effect appears to be the weaker process, possibly because the AlAs barriers are thin (or do not confine in all directions) and do not prevent charges tunnelling between quantum dots[180]. This explanation will be considered again section 4.3.3.3.

From the ER and EQE results I conclude that the presence of AlAs reduces gallium and indium intermixing, so less InGaAs alloy is formed. In the control device, this alloy contributes to photon

absorption so its reduction in the AlAs device results in a lower J_{sc}. Although AlAs is therefore detrimental to J_{sc} the incorporation of AlAs increases the V_{oc} considerably and this will now be investigated.

4.3.3 Charge extraction from the intermediate band

With fewer ladder states, thermal and tunnelling escape from the IB to the CB should be less likely[180]. Optical, thermal and tunnelling mechanisms of QD carrier extraction will be examined. This will identify whether the intermediate band is electrically isolated such that secondary infrared (IR) photons are required to excite electrons from the intermediate band to the conduction band (optical carrier extraction), as per the model proposed by Luque et al.[195].

4.3.3.1 Optical escape

If photocurrent is extracted from the IB by optical pumping then two testable phenomena should be observed. Firstly, once electrons are in the intermediate band, then exposing the device to light that excites the IB – CB transition should help to extract this charge[196]. If the energy of this light is chosen to be a low enough to excite *only* the IB – CB transition, then the presence of extra current resulting from the extra light would show that charge from the QDs is extracted by this optical transition. Secondly, for an optical IB – CB transition, one electron must be promoted to the IB and then another photon must promote it to the CB before it recombines (timescale of the order of 1 ns [197]). The likelihood of this 'two photon to one electron' process occurring in this timeframe increases with greater intensity of light, so I expect a superlinear current trend with increasing intensity would be evident.

The first phenomenon was examined by recording the spectral response of the AlAs device both with and without exposure to extra infrared (IR) light of energy < 0.92 eV, which has

energy only to excite the optoelectronic IB - CB transition. The setup of this experiment is explained in section 3.4.3. The results are shown in figure 4-8 along with the difference between the 'with IR' and 'without IR' spectra. The IR light increases the current uniformly across the spectrum, increasing current from GaAs transitions (< 1.38eV) to the QD transition (1.15 eV). The small increase is attributed to light with energy greater than the GaAs band gap leaking through the IR filter. Transmission of leakage light through the filter was measured to be 0.5 % at 1.55 eV and rising with lower energy to 1.3 % at 1.4 eV. This might seem small but with all energies of leakage light being absorbed alongside the chosen monochromatic energy, the rise in current could be (and is seen to be) significant. Figure 4-8 shows that no enhancement specific to quantum dot current is detected.

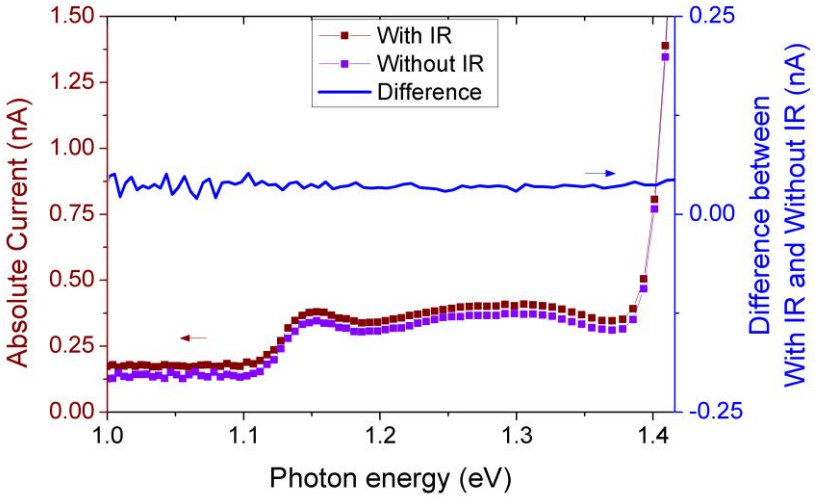

Figure 4-4-8: Current output with and without IR light (red curves). No greater current difference is seen in the quantum dot than for the other transitions (blue line)

The second phenomenon was tested by examining the current output as function of incident light intensity. This was performed at a few specific wavelengths of incident light, representing different electronic transitions in the solar cell: 1.38 eV corresponds to the GaAs transition, 1.16 eV to the InAs QD transition and 1.0 eV, from which no transition occurs, serves as a control wavelength. Plots of light intensity vs. current output for these transitions (Figure 4-9) show that a superlinear current

trend with intensity is not observed for current from the QD; instead a linear trend in quantum dot current is seen. This is identical to the trend seen from the GaAs current and is characteristic of one photon producing one electron. The 'control' wavelength where light is not absorbed varies little with intensity, as expected.

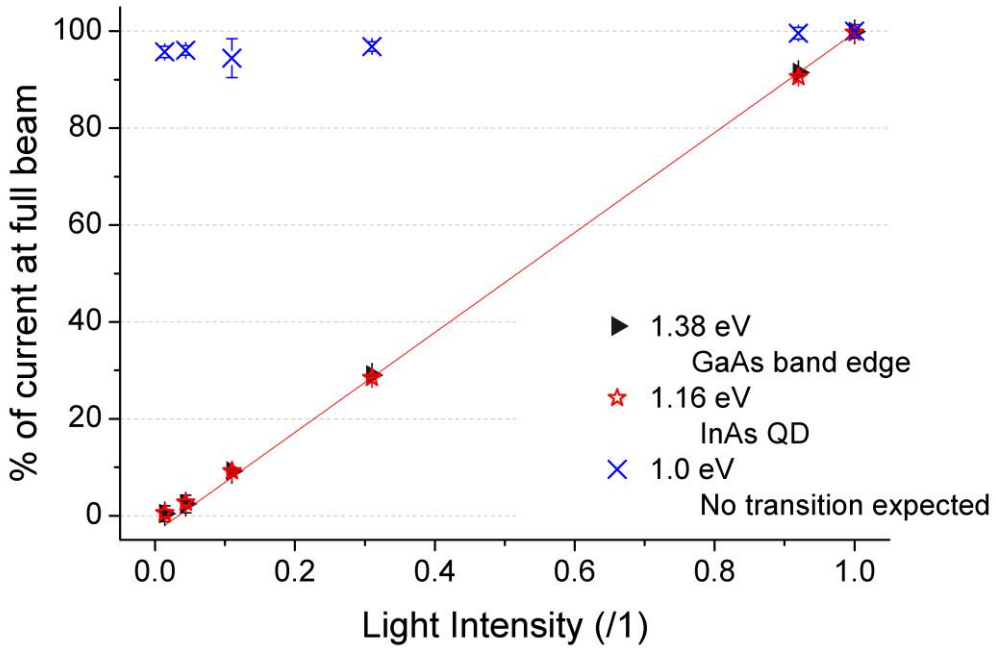

Figure 4-9: Current output on exposure of the cell to monochromatic light of energies: 1.38 eV, 1.16 eV and 1.0 eV, with 1.16 eV representing the QD transition. All values are shown as a percentage of current output at full light intensity. Values are the mean average over three repeated measurements and error bars give the standard deviation between these three measurements.

The results of these experiments suggest that there is no IB-CB optical transition. It can be concluded from this that the intermediate band is not isolated from the GaAs conduction band, in other words, Fermi level pinning does takes place.

4.3.3.2 Thermal escape

If not optically excited to the conduction band, charges from the quantum dot must be thermally excited or tunnel through to it. External quantum efficiency (EQE) of the QD

transitions as a function of temperature was performed to determine whether thermally-assisted charge extraction is dominant. The spectra are shown in figure 4-10A.

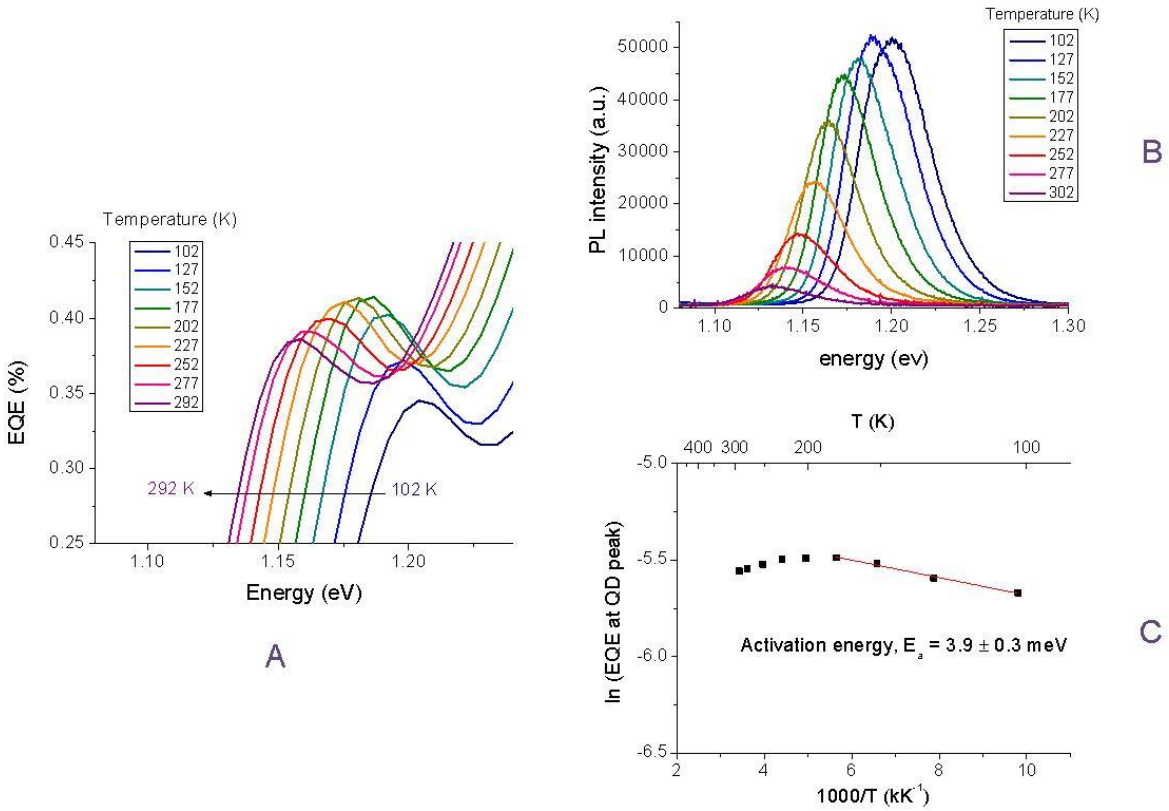

Figure 4-10: A: External quantum efficiency (EQE) around the QD excitation. B: Photoluminescence spectra of an AlAs wafer (i.e. an AlAs cell without contacts) taken at a range of temperatures. C: Plot of the natural log of the EQE of the QD peak vs inverse temperature. The gradient of the line gives the thermal activation energy.

The spectra are centred on the InAs QD transition, which is at 1.20 eV at 102 K and redshifts with increasing temperature as seen in electroreflectance (see section 4.3.2.1).

The most interesting revelation from the EQE curves is that there is significant current originating from the QDs even at the lowest temperature (102 K). This is unlikely to be wholly attributed to thermally-excited escape as k_BT at this temperature is 0.009 eV, yet the energy between the first excited state of the quantum dot and the GaAs conduction band is estimated to be at least 0.14 eV[198]. As temperature increases up to 200 K there is a rise in EQE, suggesting that temperature-assisted charge extraction does play a role.

After 200 K, efficiency falls slightly. This could partly be due to the escaping charges being spread across a wider range of energies as temperature increases, but the dominant effect could be an increase in non-radiative recombination with temperature[199], suggested by the photoluminescence (PL) as a function of temperature shown in figure 4-10B . These graphs spectrally map the radiative recombination from the QDs in an AlAs wafer excited by a 633 nm HeNe laser at 15mW. The rapid drop in radiative recombination after 127K, suggests the increase in non-radiative recombination.

The thermal escape most evident at low temperatures can be quantified by a thermal activation energy E_a, with thermal carrier escape being proportional to $e^{-\frac{E_a}{k_B T}}$. Similar devices which have primarily thermally assisted extraction have activation energies in the order of 100 meV[180]. The Arrhenius plot of the natural log of the quantum dot EQE as a function of inverse temperature (figure 4-10C) has a slope of $-\frac{E_a}{1000\,k_B}$ and gives an E_a of just 3.9 meV. If the process were purely thermal, a higher thermal activation energy would be expected alongside a low quantum dot current at 80 K. This suggests that other mechanisms are in place to extract current.

4.3.3.3 Tunnelling

As both optical excitation and thermal excitation do not have a key role in the AlAs device, then tunnelling from the QDs to the GaAs conduction band must prevail. This is feasible according to other studies in the literature with thin layers (< 15 nm) between dots[180,200]. This process may be aided in InAs/AlAs systems by low energy X-states in the AlAs barrier[197,201] or a greater coupling between quantum dots than when they are in a GaAs-only matrix[202,203]. Alternatively, the thin AlAs barrier and the lack of InGaAs states could inhibit tunnelling. To study this, the temperature dependent photoluminescence spectra are studied more closely.

The energy of PL emission and the full width half maximum (FWHM) of the spread of emission energies reveals information about the charge occupancy of the QDs. If charges are mobile between

QDs then the average emission energy across the QD band gap and the FWHM will both be small (figure 4-11A). If charges are not mobile between QDs then the FWHM and average PL energy will increase, as carriers cannot relax to the lowest energy states in the system before radiative recombination takes place (figure 4-11B).

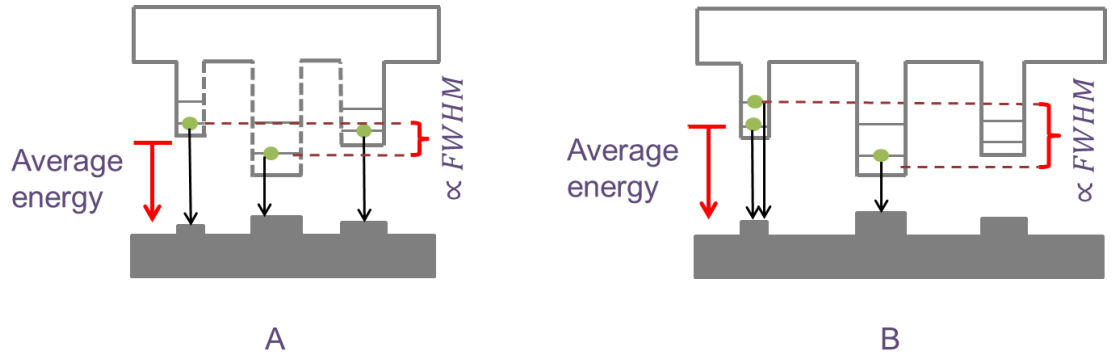

Figure 4-11 A: charge movement between QDs can occur so photogenerated charges can relax to the lowest energy states of the system before radiative recombination. B: charge movement between QDs cannot occur, so photogenerated charges are 'frozen' in whichever states they were initially excited.

In this case, I assume the dominant form of inter-dot charge movement to be tunnelling. Devices with different tunnelling rates will show different FWHM and Eg trends with temperature.

In the case of fast tunnelling the FWHM will vary little with temperature at low temperatures as all excited electrons can relax to the band edge without thermal assistance. FWHM might rise a little at high temperatures as thermal broadening can take place, with thermally redistributed charges able to be recaptured by dots of all sizes and levels of confinement[204]. The decrease in band gap with temperature, $E_g(T)$, will follow the Varshni equation[205] (equation 4-1):

$$E_g(T) = E_0 - \frac{\alpha T^2}{T + \beta}$$

Equation 4-1

with E_0 being the band gap at zero kelvin, and α and β being material specific constants.

In the opposite case of no inter-dot tunnelling, there will be three temperature regimes. At low temperatures, excited electrons will be frozen in the QDs[206], as per figure 4-11B, resulting in a large

FWHM and high average PL energy. As temperatures increase, the scenario of figure 4-11A is more likely as carriers can be thermally excited outside of the QD confinement and then redistributed to lower states in other QDs. Consequently the PL energy rapidly redshifts with temperature[206,207] alongside a fast decrease of FWHM[199,204,206]. This thermal redistribution reaches a point of maximum change before, at a higher temperature still, the PL-energy vs. temperature curve follows the Varshni equation, but following a lower E_g to that predicted at low temperatures. Concurrently, the FWHM can increase again[199,206] as a result of thermal broadening. Thus, a device exhibiting no inter-dot tunnelling will display a sigmoidal energy curve and a V-shaped FWHM graph[208].

Therefore the energy depth of this FWHM 'V' and sigmoidal shape of the PL peak energy indicates the strength of tunnelling[208].

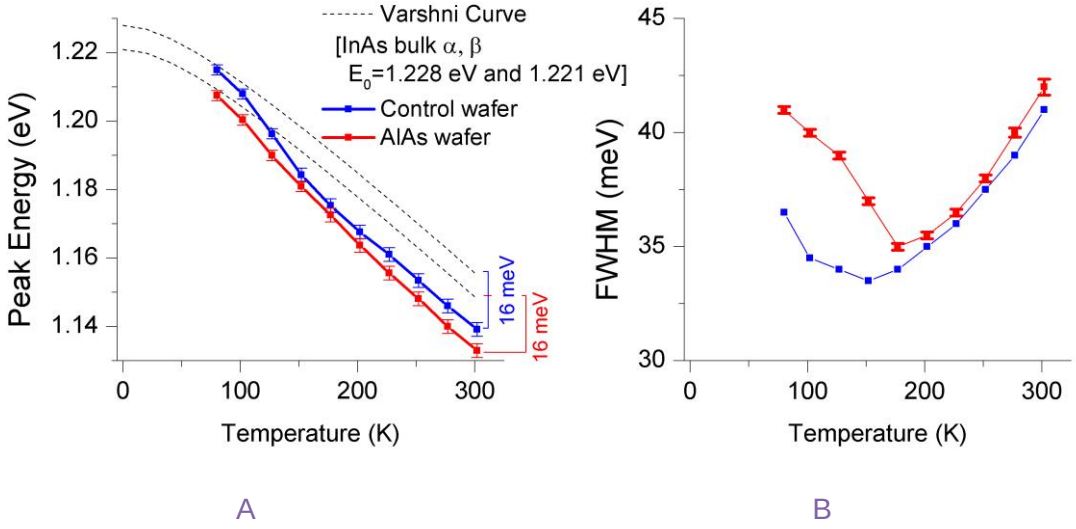

Figure 4-12: A: Peak PL energy of AlAs cell (red) and control cell (blue) along with the Varshni curve for InAs (dotted line). B: FWHM of PL lineshapes of AlAs cell and control cell as a function of temperature

Figure 4-12A shows the PL peak energies for both samples along with two InAs Varshni curves (with bulk parameters of α and β but shifted in the energy axis for comparison with the PL of the quantum dots). The fast redshift from the Varshni curve is evident in both structures up to temperatures of about 150 K. As the curves are both in the redshift phase at 80 K it is hard to determine the exact deviation from the Varshni equation but, as portrayed in the graph, the room temperature deviation

from the Varshni curves are 16 ± 2 meV for both devices. InAs QD systems with low tunnelling have shown a greater change in PL energy with temperature than either of these structures[199,206]. One interesting example in the literature performed PL on InAs dots with 20 nm-thick $Al_{0.6}Ga_{0.4}As$ barriers[209], in which the deviation from the room temperature Varshni curve was 120 meV compared to just 30 meV for QDs within 20 nm GaAs barriers.

Figure 4-12B shows the FWHM with temperature with a distinct V-shaped dependency seen with a 80 K – 177 K energy range of 6 meV for the AlAs sample compared with 3 meV for the control sample. This suggests that charge movement between QDs is easier in the control sample than the AlAs sample. Furthermore, the lowest FWHM is at a lower temperature for the control sample. This indicates that there is a lower energy barrier around the QD in the control sample, so a lower thermal energy is required for charge equalisation amongst quantum dots[209]. The FWHM energy ranges for both of these samples are low in comparison to similar systems which have claimed no tunnelling[199,208], inferring that there is some tunnelling occurring in both samples. For example, Polimeni et al[209] observed a 20 meV FWHM range for InAs QDs in GaAs and about 30 meV when $Al_{0.}3Ga_{0.7}As$ was the barrier.

In summary, the slight departure of the PL energy from the Varshni curve and low-energy-range V-shaped FWHM dependence with temperature indicates moderate tunnelling in both devices. The thermal activation energy and low-temperature FWHM trend indicate a thermal and tunnelling hindrance for the AlAs cell.

The optical and thermal results of sections 4.3.3.1 and 4.3.3.2 showed that an isolated intermediate band is not formed in these devices and that tunnelling must be the main escape mechanism from the QDs to the conduction and valence bands. The PL analysis of this section concludes that although the lack of InGaAs states and presence of AlAs barrier may restrict tunnelling somewhat, they do not hinder charge movement greatly. This is good in one respect, as tunnelling between dots is desired to limit the traps acting as recombination centres[195]. However, further modifications of this device

should include perhaps thicker spacer layers at the edge of the intrinsic region to prevent tunnelling into the conduction band.

4.3.4 Origin of the V_{OC} increase

Open-circuit voltage (V_{OC}) is the point at which charge generation and recombination are balanced. At forward bias, charges are injected into the device from the electrodes, which acts to split the quasi-Fermi levels[210]. After crossing the junction, these charges become minority carriers and recombine. Illumination causes a generation current, acting in the opposite direction to the recombination current. The bias which causes enough recombination to balance the generation is the open circuit voltage and is equal to the quasi-Fermi level difference at that point[22,57]. A higher rate of recombination will result in a lower bias being required to balance photocurrent, and thus a lower V_{OC}. Changes in injection and recombination are examined here using capacitance-voltage and dark current-voltage measurements.

4.3.4.1 Charge injection

Figure 4-13 shows the dark JV curves, which plot the injection current at different applied forward biases. The turn-on voltage is given here as the x-axis intercept of the extrapolation of the JV curve at 1 V and indicates the bias that must be applied for the diode to start rapidly injecting. The AlAs cell 'turns-on' at a higher voltage than the control cell, which suggests that the presence of AlAs reduces the injection rate.

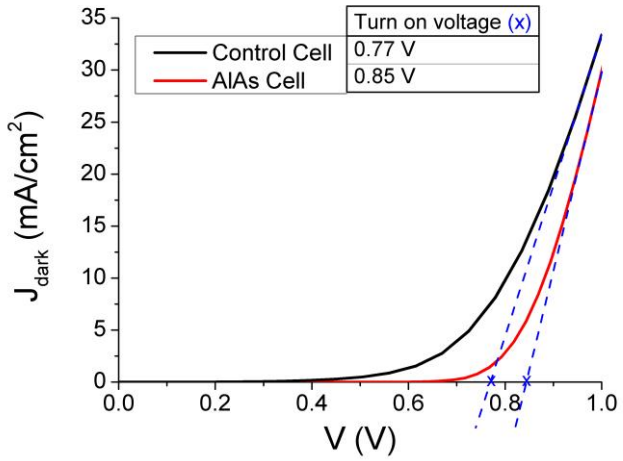

Figure 4-13 Dark J-V curves of the control cell (black) and AlAs cell (red) with the turn-on voltage (marked by a blue cross) given by the x-intercept of the extrapolation of the curves at 1 V.

Figure 4-14 shows the capacitance-voltage (CV) curves for the two devices. CV at reverse and low forward biases reveals information about charge accumulation and extraction within the depletion region of the device. CV measurements are shown for a modulation amplitude of 25 mV and a modulation frequency of 5 kHz, which was chosen to be a compromise between noisy low frequency measurements and high frequencies, which prevent some charges from being able to react and contribute to capacitance in time[211].

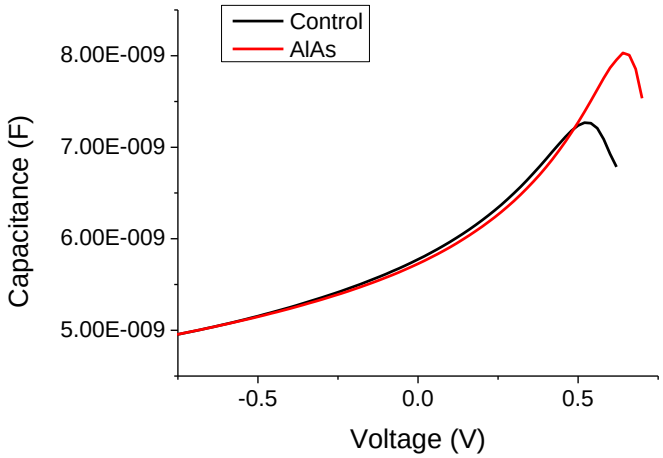

Figure 4-14 Capacitance – voltage curves for the control cell (black) and AlAs cell (red) taken in the dark.

Both devices show an increase in capacitance with increasing forward bias as injected charges accumulate in the depletion region. The capacitance peaks at 0.64 V for the AlAs cell and 0.53 V for the control cell. At biases higher than the capacitance peak, stored charges are now able to be extracted or to recombine.

The reason this accumulation and subsequent extraction/recombination occurs varies according to cell structure. In a p-i-n structure, as being used here, the depletion width should not diminish with bias[212], so the rise and fall in capacitance is unlikely to result from changes in the packing density of injected charges, as it does for p-n junction or Schottky cells[213,214]. More likely, the rise in capacitance mirrors charge accumulation within traps[215], including QDs[216], with the peak being the bias at which trapped charges are released. Therefore charges are released at a higher bias for the AlAs cell, suggesting that recombination is lower in the AlAs device or that extraction is more difficult. Lack of InGaAs states would remove a stepping stone that would have facilitated extraction from traps.

Also, the AlAs energy barrier could delay charge injection, as suggested can happen with AlGaAs barriers[217]. If the injection of one type of carrier is hindered until a higher bias than for the other carrier type, then recombination will not easily occur until that higher bias. A higher injection bias of the second carrier produces the higher bias capacitance peak and greater peak capacitance[218] , which is seen in the AlAs cell and control cell CV comparison. The energy level alignment (figure 4-2) suggests that the AlAs barriers would delay electron injection from the n-type conduction band before hole injection from the p-type valence band. However, the EQE measurements presented earlier showed that the EQE of the AlAs cell is 89% that of the control cell so if charge extraction from the QDs is not limited by the AlAs barrier by much, then charge injection would be similarly only slightly affected by it.

Dark JV and CV show slower injection in the AlAs cell. The AlAs barrier could limit injection but, based on EQE results, I do not expect the effect to be great. Alternatively, the slower injection could

suggest more recombination or charge extraction pathways in the control cell. Dark JV parameters will explore recombination differences in more depth.

4.3.4.2 Diode parameters

The dark current parameters, namely ideality factor (n) and reverse saturation current (J_0) are given by the non-ideal diode equation[23]:

$$J_{dark} = J_0\left(e^{\frac{qV}{nk_BT}} - 1\right)$$

Equation 4-2

The ideality factor gives the type of recombination with values usually between 1 (for ideal diode with only band-to-band recombination) and 2 (for depletion region or trap-assisted recombination)[219]**.** J_0 gives the magnitude of this recombination.

Equating J_{dark} to photocurrent (as is the case at open circuit), and rearranging, gives the expression for V_{OC} as**:**

$$V_{OC} = \frac{nk_BT}{q}\ln\left(\frac{J_{ph}}{J_0} + 1\right)$$

Equation 4-3

The equation shows V_{OC} will increase if J_0 decreases (decreasing recombination) or if n increases (and recombination is limited by more types of carriers). Thus the extent of the J_0 change compared with the change in n determines the resultant V_{OC}. Furthermore, if photocurrent, J_{ph}, decreases, V_{OC} will decrease. The effect of changing each of these parameters is illustrated in figure 4-15. The dark parameters individually could alter V_{OC} by values far greater than is likely from a smaller J_{ph}. Nevertheless, it should be remembered that n and J_0 can increase or decrease together and thus each will mitigate the effects of the other[220].

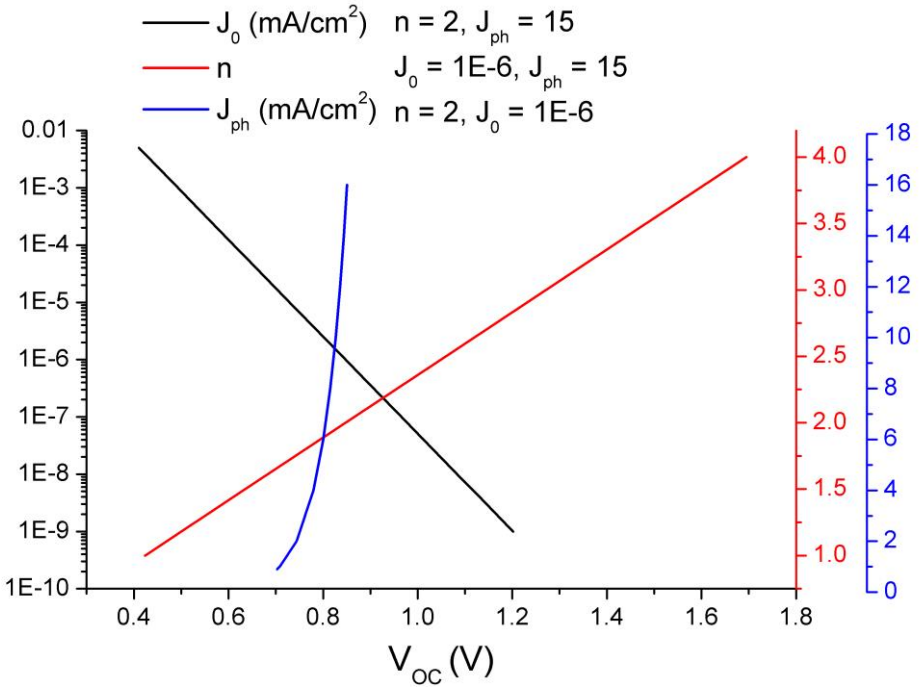

Figure 4-15: Effect of changing J_0, n and J_{ph} on the V_{OC}. Whilst changing one parameter the other parameters are kept constant, with values shown above the graph.

Dark JV parameters

The exponential portions of the dark JV curves were fitted to the dark current equation[23] (equation 4-2), with fitted parameters shown in table 4-1.

Cell	Ideality Factor	Saturation Current (mA/cm^2)
Control	3.74 ± 0.10	(2.4 ± 0.1) E-3
AlAs	1.46 ± 0.06	(5.3 ± 1.2) E-9

Table 4-1: Dark JV parameters, with fitting errors, for the AlAs and control solar cells

Both devices have ideality factors that deviate from unity, perhaps because the QDs can act as recombination centres as well as current generation centres. However the value of 1.46 for the AlAs cell is comparable to imperfect GaAs p-i-n structures[75]. The ideality factor greater than 2 for the control cell is abnormally high. Such high values have been taken as a sign of recombination via dislocations[75], increasing with the density of defects in the solar cell[221]. Defects are known to form

when strain builds up in the device[86,222,223]. This tallies with the low shunt resistance of the control cell discovered after examining the light JV curves (section 4.3.1), which were thought to suggest misfit dislocations.

The lower reverse saturation current for the AlAs cell, combined with the lower ideality factor indicate decreased recombination in this device, which would lower the injection rate as seen in the dark JV and CV curves (section 4.3.4.1). J_0 decreases by six orders of magnitude, which must dominate to cause the V_{OC} decrease (equation 4-3). In QD IBSCs, a high J_0, such as that seen for the control cell, has been attributed to high defect density [75,79,224], in line with theories relating to the ideality factor.

A morphological study would be required to pinpoint the useful structural changes caused by the AlAs layer, which, seem to play a significant role in the V_{oc} enhancement via the lower J_0.

Photocurrent

The changes in recombination mechanisms that affect the dark current, might also affect the photocurrent. It is often assumed that the photocurrent is bias-independent and thus equal to the short circuit current[225]. However, in some cases a reduction in J_{ph} with increasing bias has been observed[226–228]. Such a phenomenon points to a poor charge extraction at high biases, possibly because of low charge carrier mobility and high recombination[227]. Additionally, the presence of photogenerated charges could further increase the probability of recombination. In this case, illumination will not only result in a generation current but also a recombination current, which will add to the dark current, resulting in an apparent positive photocurrent at high biases.

Subtracting the light JV from the dark JV gives the photocurrent density-voltage curves (figure 4-16). It is evident that photocurrent decreases with increasing bias for both devices. The decrease in

photocurrent starts at a lower bias in the control cell than the AlAs cell. This earlier diminishing of photocurrent could be linked to the poor parasitic resistances of the control cell, which act to lower charge mobility and to channel photocurrent into shunt pathways. At around 0.7 V the photocurrent decrease slows, as at a high enough forward bias, all photogenerated charge is channelled into another route. The fact it does not slow to zero could possibly be due to slight differences in measurement conditions whilst taking the light and dark measurements.

As confirmed by EQE (figure 4-7), the AlAs barriers do not hinder the majority of photocurrent extraction (which comes mainly from GaAs transitions). I thus assume that the parameters that are responsible for increases in dark current also seem to degrade the photocurrent. In contrast to the shape of the control cell curves, the light and dark JV curves of the AlAs cell exhibit a clear crossover at 0.85 V. So, although recombination is lower in the AlAs cell, the presence of photogenerated charges does seem to increase likelihood of recombination. This is probably more apparent in the AlAs cell than the control cell because photogenerated charges in the AlAs cell are not as hindered by the parasitic resistances as they are in the control cell.

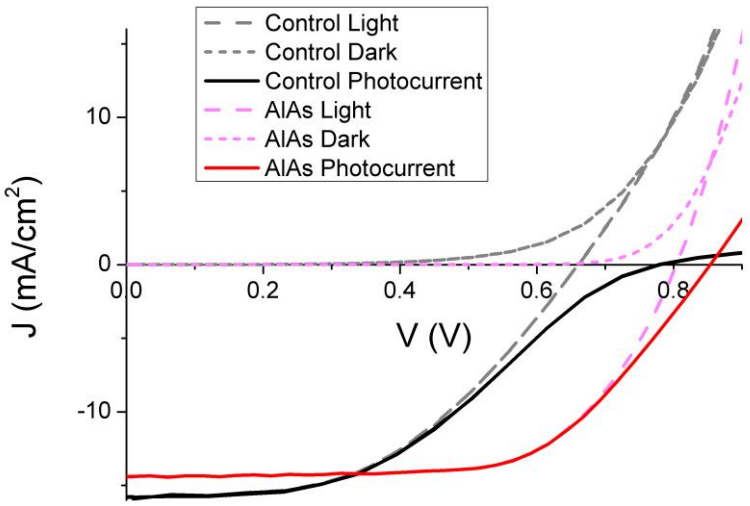

Figure 4-16: Photocurrent density-voltage curves (solid lines) for AlAs (red) and control (black) devices. These are the difference between the light JV curves (long dashes) and the dark JV curves (short dashes).

The dark JV, CV and photocurrent all point to the V_{OC} being improved in the AlAs cell as a result of reduced charge recombination. The high energy barrier property of the AlAs is unlikely to be the cause as current from the device is not limited much. The reason for the lower recombination may instead be that the AlAs layer results in fewer defects within the device or that the lack of InGaAs states help to reduce recombination. The increase in shunt resistance seen in the JV curves (figure 4-4) hints towards the former explanation and it would be interesting to investigate this further.

4.4 Conclusions

An AlAs barrier was incorporated into InAs QD/GaAs solar cells to try to isolate the InAs intermediate band from the conduction and valence band of the GaAs. The aim of this was to increase the V_{OC}. It was hoped isolation would be achieved because: firstly, AlAs is a wide band gap material and secondly placing AlAs between InAs and GaAs will reduce indium gallium intermixing. Both of these things would limit interaction between the GaAs conduction and valence bands and the QD energy states.

JV parameters (figure 4-4) showed an increase in V_{OC} from 0.66 V to 0.80 V, but this was at the expense of the J_{sc}. Electroreflectance (figure 4-6) and external quantum efficiency measurements (figure 4-7) showed that the J_{sc} reduction was due to the lack of InGaAs states in the AlAs cell, as AlAs had successfully prevented intermixing of gallium and indium. The AlAs does reduce the current from the QD but only by 11 %, suggesting that the thickness of the barrier is such that charge movement is not greatly blocked.

The increase in V_{OC} was not because of isolation of the intermediate band. This would have been demonstrated by an optical transition from the QD excited state to the GaAs conduction band. Thermal charge escape was also shown not to prevail and, instead, tunnelling is the dominant extraction mechanism. Photoluminescence measurements showed that although tunnelling is restricted in the AlAs cell at low temperatures, at room temperature the difference between the AlAs cell and the control cell is small and, as EQE demonstrated, the AlAs barrier does not prevent charge movement from the QDs.

Dark current measurements showed that the V_{OC} improvement is because of reduced recombination in the AlAs cell. This and increased R_{sh} suggest a lower defect density in the AlAs. The factors influencing this recombination seem to reduce J_{ph} at a lower forward bias in the control cell than the AlAs cell. This reduces V_{OC} more than it would for stable photocurrents. A morphological study is required to investigate why the ideality factor of the control cell is so much higher than the AlAs cell and whether the AlAs reduces the presence of dislocations.

From this work, future design considerations and study points are put forward:

- The significance of the absorption from InGaAs cannot be neglected. As the lack of InGaAs is important to try to isolate the intermediate band, it is best to not reinstate it. However, to lessen the effect of reduced InGaAs absorption, absorption from the QDs could be

enhanced. This could involve increasing dot density[53] or by delta-doping the QDs so there is already an electron population within them[51,229].

- The isolated intermediate band is not formed because tunnelling can take place from the QDs to the conduction and valence bands. With a more ideal choice of host material/ QD energy alignment this would diminish. However, to use the InAs/GaAs system, spacers could be used either side of the quantum dot region as, if they are thick enough or wide enough, tunnelling will be reduced[79,230].

5. PbS:ZnO Colloidal Quantum Dot Bulk Heterojunction Solar Cells

5.1 Introduction

Colloidal quantum dots (CQDs) are an emerging photovoltaic technology. In the last eight years, efficiencies of CQD-based photovoltaic devices have increased from around 0.1 %[231] to 7 %[232]. CQDs have quantum tuneable band gaps meaning they can be tailored to absorb across the whole solar spectrum[100] and only require low temperature processing which has the potential to substantially lower the cost of production[94,95]. Attempts are being made to improve the efficiency of heterojunction CQD PV by fabricating PbS:ZnO solar cells with a large interfacial area, via colloidal phase segregation during processing[233]. The challenge addressed in this chapter is to understand the optoelectronic properties of this system, examining the mechanisms for separation and collection of photogenerated excitons and how this impacts upon JV characteristics. From this understanding a strategy to improve next generation CQD devices will be developed.

Power conversion efficiencies of bilayer heterojunctions are limited by their thickness[161,234–236]. Photogenerated electron-hole pairs cannot contribute to current if they are generated more than their diffusion length away from the heterojunction in an excitonic solar cell[161,234] (figure 5-1A) or from the depletion region in a p-n junction solar cell[236] (figure 5-1B). To overcome this diffusion length limitation in organic photovoltaics, the bulk heterojunction (BHJ) structure was conceived[87]. In this BHJ structure, the electron and hole transport materials form interpenetrating phase segregated networks at the length scale of the exciton diffusion length[87] as shown in figures 5-1C and 5-1D. This results in a greatly improved interfacial area, which could improve the efficiency of charge carrier collection.

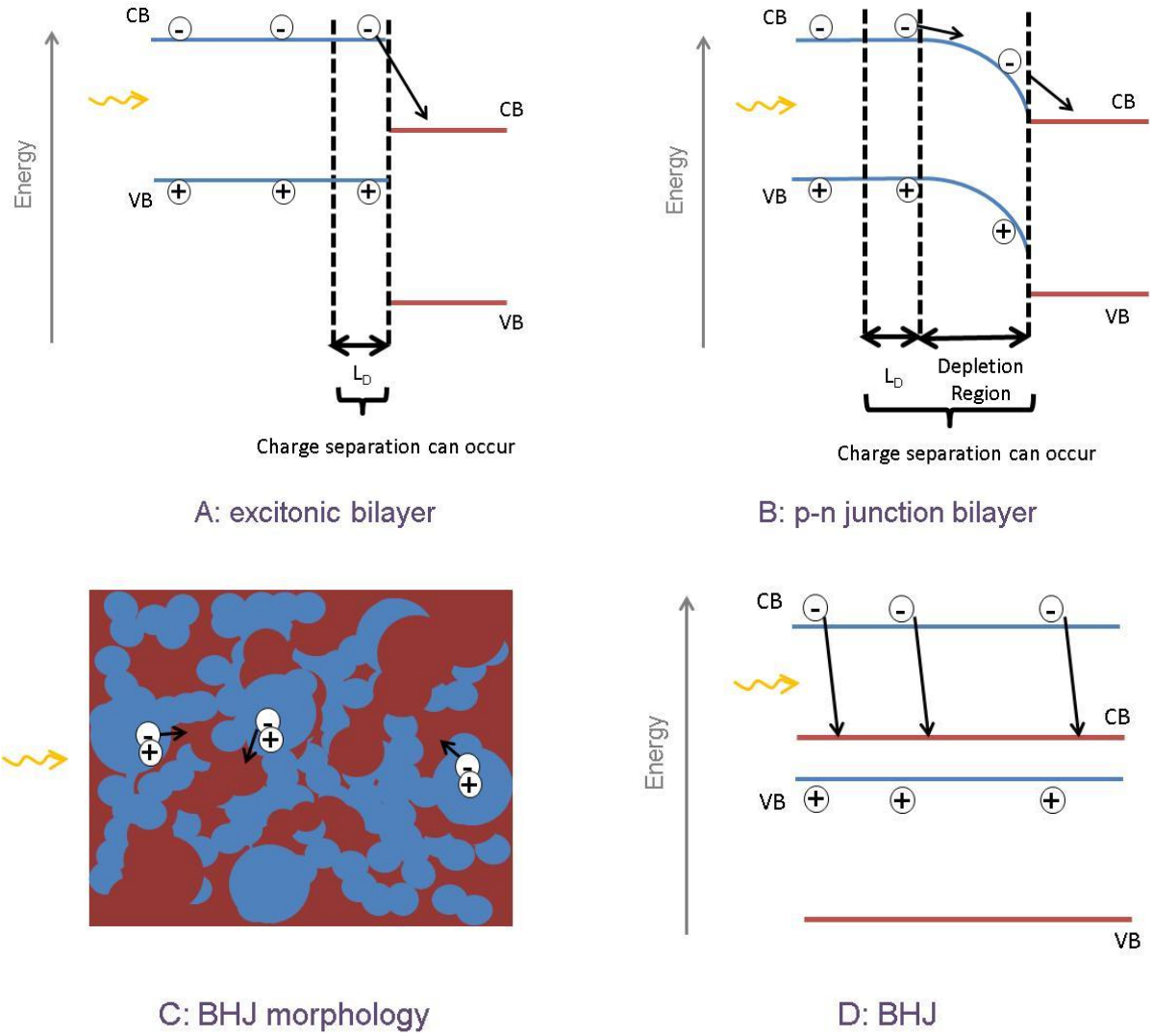

Figure 5-1: Various forms of heterojunctions, with light being absorbed and excitons being generated in the 'blue' phase. In the electronic energy diagrams, the horizontal lines represent conduction bands (CB) and valence bands (VB). A: electronic energy structure of an excitonic bilayer solar cell, in which charge separation can occur only within one diffusion length (L_D) of the heterojunction. B: electronic energy structure of a p-n junction solar cell, in which charge separation can occur within the depletion region and one diffusion length away from it. C: Morphological structure of a bulk heterojunction (BHJ) solar cell, with interpenetrating phases in which excitons can be generated within one diffusion length of an interface. D: electronic energy structure of a bulk heterojunction solar cell, in which excitons can dissociate throughout the active layer of the solar cell.

This study explores composites of 2.8 nm-diameter lead sulphide (PbS) CQDs with 5-10 nm zinc oxide (ZnO) nanoparticles. Via quantum confinement the PbS band gap is reduced from 3020 nm (0.41 eV)[97] to 990 nm (1.25 eV). The ZnO retains bulk properties as the particles are larger than the Bohr radius which is 2.43 nm[237]. There has been some controversy in the literature as to whether lead chalcogenide/ ZnO bilayer structures are either excitonic[238,239], p-n [112] or a combination of both[117]. Willis et al.[117] showed that both excitonic and p-n mechanisms have a role, with the

dominant mechanism determined by the carrier concentration of the ZnO, which could be modified by photodoping. They further demonstrated that a small charge separation region severely limits the efficiency of the device. In particular, the maximum external quantum efficiency measured when the device behaved excitonically is 5%, increasing to 37% when a large p-n depletion region had formed after photodoping[117]. For either mechanism it has been shown that it is possible to improve charge collection efficiency by increasing interface area with a BHJ device[87,92,93].

To determine whether the increased interface area of the bulk heterojunction solar cell improves cell performance in this case, I use a combination of photoluminescence, external quantum efficiency, and current-voltage measurements to probe charge extraction and recombination mechanisms of PbS/ZnO BHJ solar cells. A series of devices are tested, with varying relative weight percentages of the two components.

5.2 Devices

Devices in this chapter were made by Mr Cheng Cheng and Mr Darren Neo of the materials department of Oxford University. I then performed all device characterisation and analysis unless explicitly stated. In particular, the modelling of the composites (section 5.4.3.2) was performed by Mr Francesco de Cola and Mr Simone Falco of the engineering department of Oxford University.

The structure of the semiconductors in all devices was: PbS – PbS:ZnO composite – ZnO. Cells of different PbS:ZnO blend ratios were fabricated, always including one cell without ZnO in the composite, which acted as a control bilayer solar cell. PbS quantum dots capped with oleic acid ligands were synthesised via a method described by Hines and Scholes[240]. ZnO nanoparticles were synthesised according to the method explained by Pacholski et al.[114]. Mr Cheng Cheng used transmission electron microscopy (TEM) to determine PbS QD diameters as 2.8 nm and the ZnO

nanoparticle diameters as 5-10 nm. The PbS and ZnO were combined in toluene solution for casting into the bulk heterojunctions.

Indium tin oxide (ITO) on glass substrates was used as the transparent front electrode for all types of cell, with a poly(3,4-ethylenedioxythiophene):poly(styrene sulphonate) (PEDOT:PSS) layer on top to smooth the ITO surface. Onto this, one layer of PbS was spin coated from toluene solution to act as the electron blocking layer. Following this, layers of PbS: ZnO nanocomposite were spin coated. Generally four of these extra layers were deposited, unless otherwise stated in the text. For the bilayer control cell, a PbS-only solution was spin coated rather than the composite solution. After deposition of each layer of PbS or PbS: ZnO nanocomposite, a ligand exchange treatment was performed to remove oleic acid (OA) ligands and replace them with shorter 1,2-ethanedithiol (EDT) ligands[241]. This involves dropping EDT onto the spinning films and then washing away residual EDT and OA with drops of methanol and then toluene. After the deposition of all the active layers one layer of ZnO was spin coated atop the rest of the cell, to act as a hole blocking layer. Finally, three aluminium electrodes were evaporated onto the surface, resulting in three individual solar cell 'pixels', as shown in figure 5-2. Devices were tested in a nitrogen atmosphere as soon as possible after manufacture and stored in a nitrogen dry-box between tests.

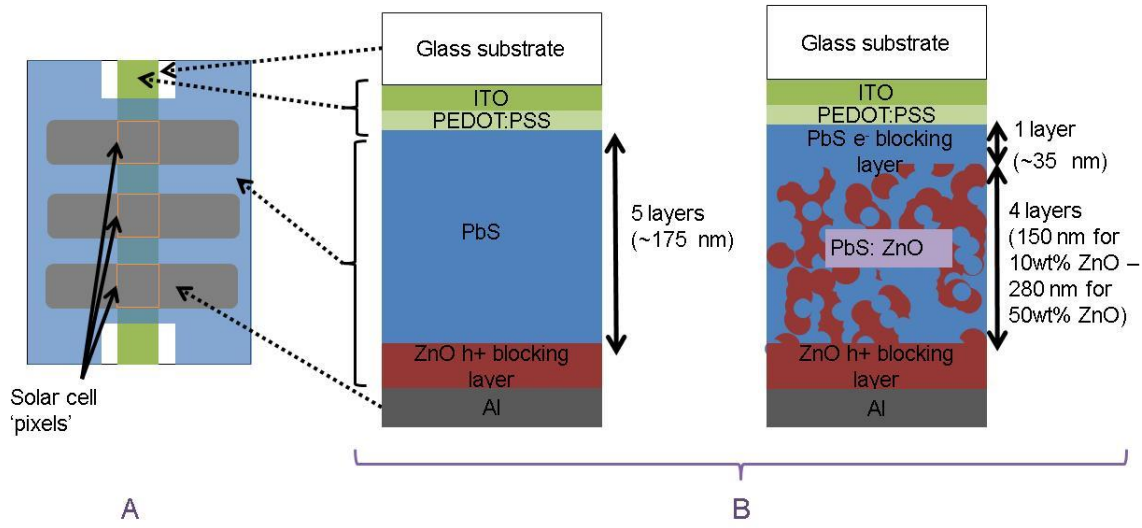

Figure 5-2: A: Plan view diagram of the solar cell with the active layer (blue) sandwiched between the ITO/ PEDOT:PSS (green) and Al electrodes (grey). The three 'pixels' where the electrodes overlap are indicated with orange outlines. B: Schematic cross-sections of pixels with 5 spun active layers. On the left is a bilayer device of 5L PbS. On the right is depicted the bulk heterojunction structure consisting of 1layer of PbS + 4 layers of PbS:ZnO nanocomposite. The thicknesses of the layers were measured by a DEKTAK profilometer. The electrodes and ZnO blocking layer are the same for both types of device.

Absorbance measurements in the region of the first excitonic transition were taken to determine the PbS quantum-confined band gap. The PbS in the post-ligand-exchange final device absorbs at a higher wavelength than the PbS in toluene solution (figure 5-3) indicating that band gap is smaller in the final device. This difference arises because of the difference in QD separation when QDs are in solution compared to when they are deposited in the device. In the device, the shorter EDT ligands surrounding the QDs enable the QDs to get close to each other, which results in greater electron wavefunction overlap[241], which in turn reduces the energy level of the lowest QD energy state[242]. Note that CQDs also absorb at shorter wavelengths than the transition shown - corresponding to higher level excitonic transitions[243] - but these were not shown here. The average band gap taken from the spectra of PbS dots in eight devices or films was 990 ± 20 nm (1.25 ± 0.02 eV), with errors giving the standard deviation of the band gaps across the samples. Discussion of whether or not the ZnO in the blend affects the PbS band gap is considered in section 5.5.1. ZnO has a band gap of 375 nm[244] (3.3 eV) so does not absorb in the visible region. Figure 5-4 shows the expected energy level diagram, with conduction band (CB) and valence band (VB) levels from the literature[238,245]. The

conduction band offset of 0.5 eV should be enough to overcome the PbS exciton binding energy which literature proposes to be up to 0.3 eV[246,247].

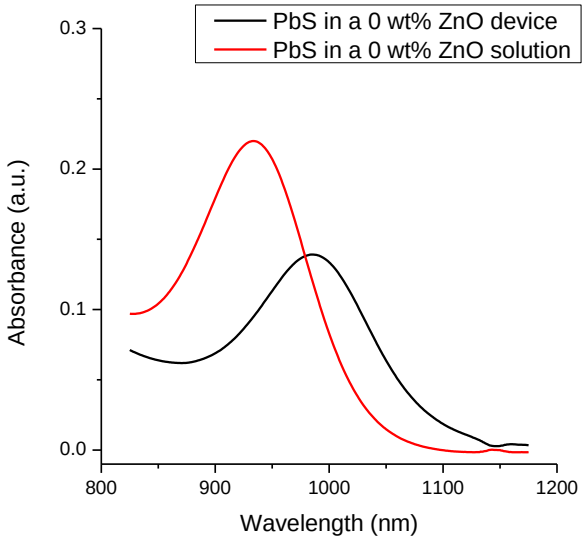

Figure 5-3: Absorbance spectra of PbS-OA-toluene solution (red) and PbS-EDT in a PbS/ ZnO bilayer device (black).

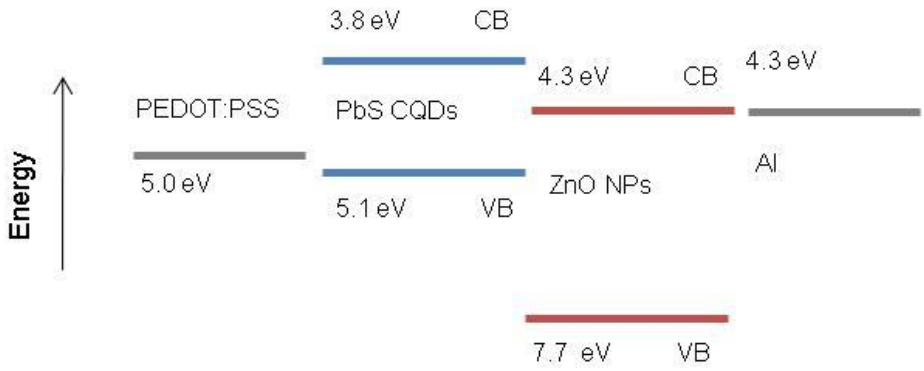

Figure 5-4: Proposed energy level diagram of the system, based on values from the literature, with each material in isolation.

The thicknesses of the active layers was measured by a DEKTAK profilometer and, as expected, increased as more ZnO is added to the composite. Average values are 35 ± 10 nm for a pure PbS layer to 70 ± 8 nm for a 50wt% ZnO layer, as shown in figure 5-5.

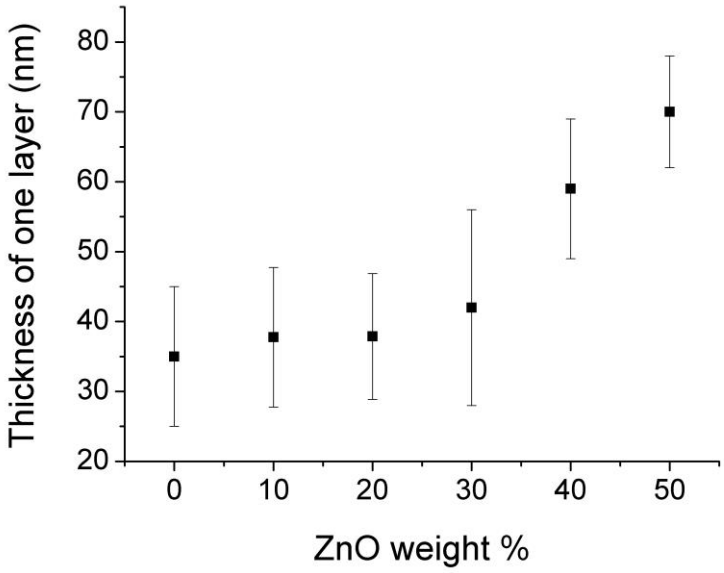

Figure 5-5: Thicknesses of one layer of PbS:ZnO films of different ZnO concentrations, with error bars reflecting the standard deviation of thicknesses across multiple films and locations on the films, totalling about 15 measurements per ZnO weight percentage.

Over a period of 10 months a number of device batches were made, each with a series of different PbS/ZnO compositions, totalling over 50 devices. Unfortunately there was a spread of overall device performance between the batches. This was due to differences in processing: particularly in electrode evaporation and dry-box environment over the course of the project. However the device behaviour trends with composition were the same and it was decided to use normalised measured parameters to give a representative and statistical understanding of device behaviour. In practice this was achieved for each parameter by firstly identifying which composition had the maximum value of this parameter in each batch. This value was then set to equal 1 with parameter values from other compositions in the batch being scaled accordingly. Once this was done, the normalised parameter values at each composition were averaged across the batches. There are three solar cell 'pixels' on each substrate and the standard deviation of measurements from these three pixels provided the error value for that composition for that batch. These error values were then scaled alongside the parameter value to which they correspond. Errors from each composition across all batches were then added in quadrature to give the errors for the normalised parameters.

5.3 Device performance

To examine how increasing the ZnO concentration in the active layer changes device efficiency, the current density-voltage (JV) characteristics were examined. Average power conversion efficiency (PCE) values obtained from these measurements are given in table 5-1, with their associated standard deviation across all device batches, which are large due to batch-batch variations.

Weight percentage of ZnO in the PbS:ZnO blend (wt%)	0 wt%	10 wt%	20 wt%	30 wt%	40 wt%	50 wt%
Mean average PCE (%)	0.69	0.74	0.77	0.84	0.60	0.30
Population standard deviation of PCE (%)	0.50	0.61	0.53	0.59	0.48	0.24
Number of samples over which the average PCE is taken	12	6	9	12	3	9

Table 5-1: Calibrated values of power conversion efficiency (PCE) averaged over all samples used. The standard deviation of the values gives an indication of the large spread of values obtained.

Parameters that feed into these PCE values, namely short circuit current density (J_{sc}), open circuit voltage (V_{OC}) and fill factor (FF) are shown in figure 5-6. The fill factor is dependent on the parasitic resistances (series resistance (R_s) and shunt resistance (R_{sh})) so the normalised values of these are also shown. V_{OC} values are not normalised, with actual mean values used instead, as these remained the same between batches, but for all other parameters, the batch-to-batch variations were normalised.

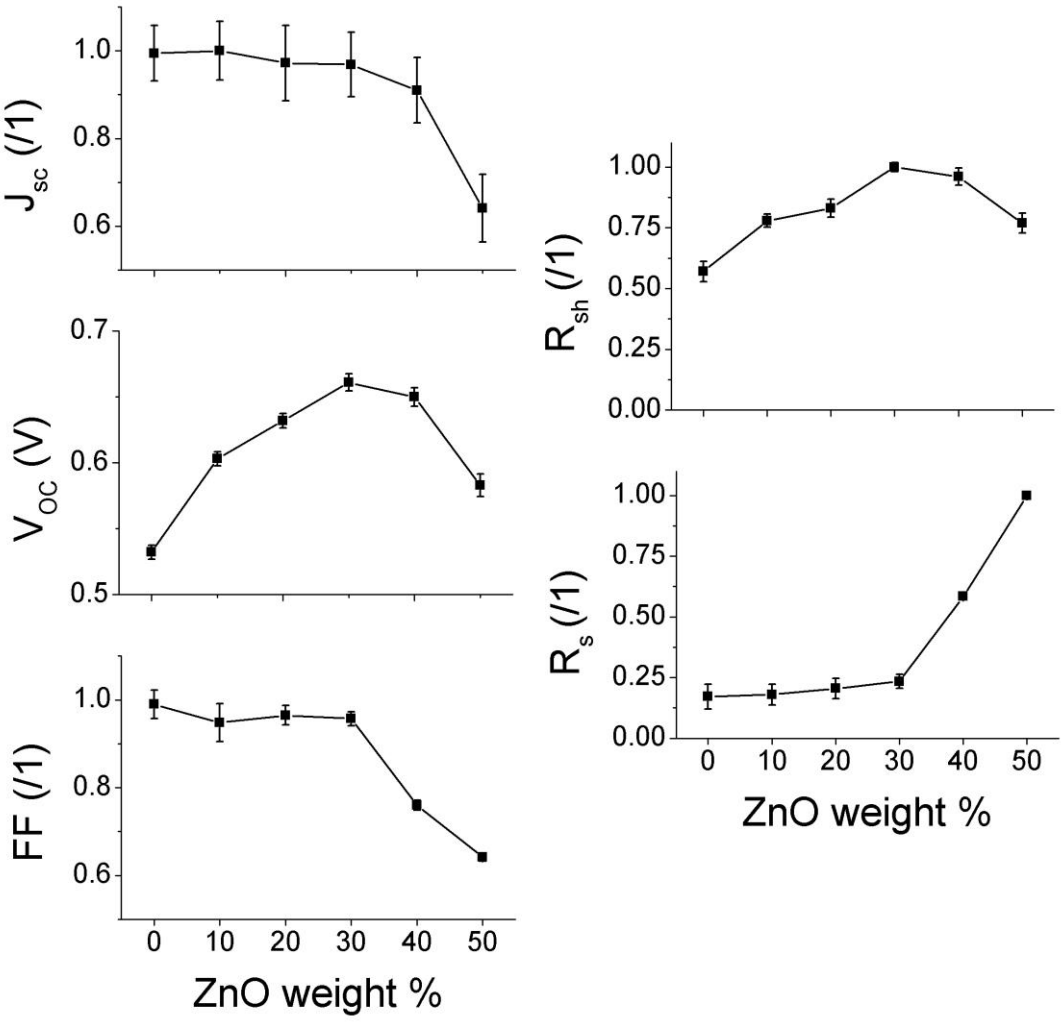

Figure 5-6: Parameters extracted from the JV curves of a series of devices of different PbS:ZnO compositions. The parameters are short circuit current density (J_{sc}), open circuit voltage (V_{OC}), fill factor (FF), shunt resistance (R_{ah}) and series resistance (R_s). Batches were calibrated to the same scale (where the maximum value equals 1) and then values for each composition were averaged. The exception to this is V_{OC} with values that did not vary much from batch to batch, so average values are given. Error bars shown reflect the standard deviation of values over the three pixels of one substrate, as explained further in the text. Lines on the graph joining the data points are guides to the eye.

The aim of the bulk heterojunction device was to improve charge extraction by creating a larger area of PbS/ZnO charge-separating interface. Surprisingly, J_{sc} does not improve for the bulk heterojunction devices and in fact decreases for the highest ZnO concentrations, as does FF. The origin of this in the first instance lies with the parasitic resistances, and it seems likely that the decrease in short-circuit current and fill factor at high ZnO concentrations is linked to the dramatic

rise in series resistance. The lack of J_{sc} improvement limits the potential efficiency improvements in bulk heterojunction solar cells.

On the positive side, V_{OC} is higher for the bulk cells than the bilayer devices. V_{OC} rises with increasing ZnO concentration but the value falls after 30 wt%. The higher V_{OC} increases the PCE of the 30wt% ZnO devices to above those of their bilayer counterparts. This thesis will now go on to understand device operation in more detail, focussing on identifying what determines the JV parameters and thus how device efficiency is limited.

5.4 Origins of the short circuit current

To identify the root of changes in J_{sc}, each of the stages of current generation are considered: photon absorption/ exciton creation, exciton dissociation and charge transport.

5.4.1 Photon absorption

Absorbance spectra of PbS:ZnO devices of 0 wt%, 30wt% and 50 wt% ZnO are shown in figure 5-7. Unfortunately it is hard to read anything meaningful into the spectra as they exhibit many bumps and a rise in absorption at wavelengths longer than 1050 nm, which is below the PbS band gap. It is unlikely that the bumps are from thin-film optical interference: although there are many interfaces where reflection could happen, light reflected from the air/ ZnO, ZnO/ PbS:ZnO or PbS:ZnO/ PbS interfaces is likely to be reabsorbed by the PbS and thus not contribute to absorbance spectra interference. Reflections from the ITO and glass layers have already been accounted for as the ITO + glass absorbance spectrum is subtracted from the absorbance spectra of figure 5-7. The bumps could be due to scattering of light[248]. Scattering indicates the presence of large particles in the film as the intensity of scattered light is proportional to the cube of the nanoparticle radius[249]. The

nanoparticles used in this study are less than 10 nm in diameter, and with particles on the order of 100 nm required to noticeably scatter light[250], it seems likely that agglomeration has occurred. Atomic force microscopy (AFM) images taken by Dr Peter Kovacik verify this: in a PbS film, PbS clusters of around 35 nm were visible and ZnO in PbS:ZnO blend films cluster to around 120 nm. In addition to being an effect of scattering, the absorption of light with energies lower than the PbS band gap could indicate the presence of mid-band gap traps in the device

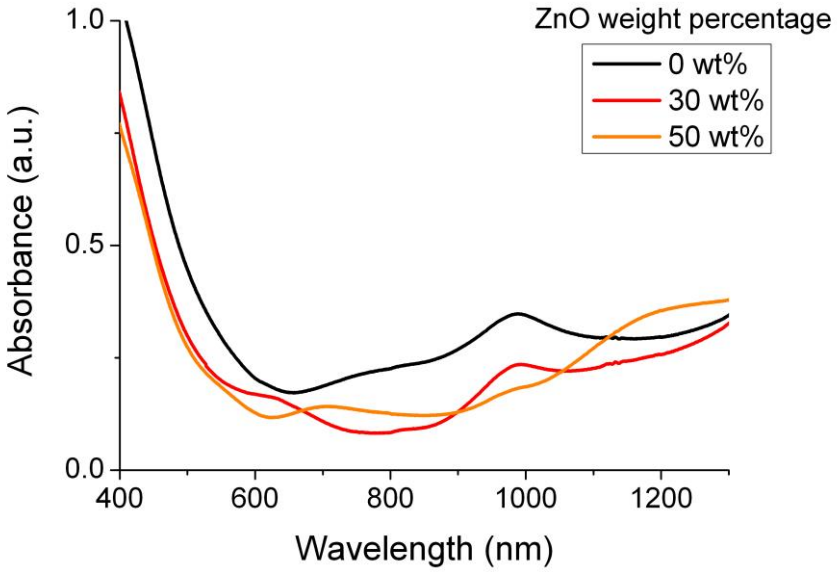

Figure 5-7: Absorption spectra of devices with different ZnO concentrations: 0 wt% black, 30wt% red 50wt% orange.

A solution to the scattering problem would be to use an integrating sphere; however there was unfortunately no access to this facility during this project. Without this, it is hard to relate absorption to device performance. To understand whether the electron-hole pairs created upon photon absorption end up as free charge carriers EQE and photoluminescence are now used.

5.4.2 Separation of electron-hole pairs

5.4.2.1 Photoluminescence

Photoluminescence (PL) spectroscopy provides a spectral map of the electronic transitions that result in radiative recombination. Photoluminescence quenching has previously been presented as evidence for electron transfer from a donor to an acceptor material[251–253]. Thus if the bulk heterojunction aids charge separation and electrons are transferred to the ZnO, then PL quenching is expected compared with the bilayer.

PL spectra from PbS:ZnO films of a range of compositions are shown in figure 5-8. Samples were excited by a 405 nm laser of strength < 10 mW. The emission comes from the first excitonic transition with the long wavelength shoulder (~1195 nm in the 50 wt% ZnO film) possibly from emission caused by shallow trap states in the PbS[254].

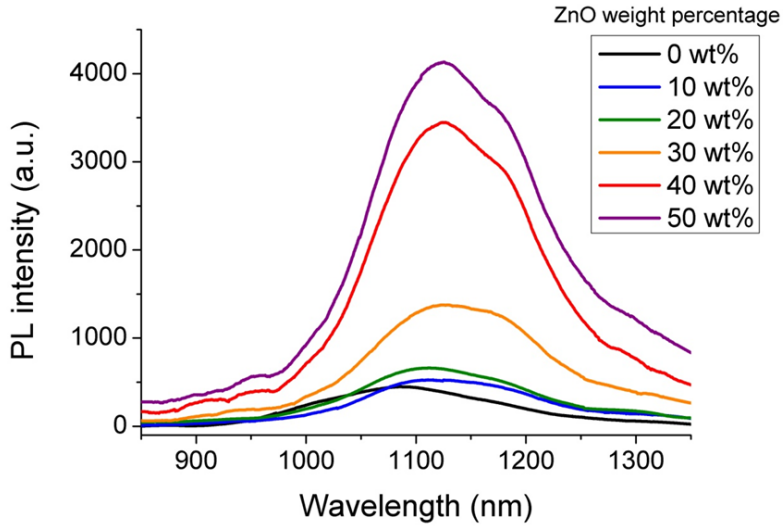

ZnO weight percentage (%)	Peak wavelength (nm)
0	1090 ± 6
10	1118 ± 7
20	1114 ± 7
30	1126 ± 8
40	1125 ± 4
50	1126 ± 4

Figure 5-8: Photoluminescence of the first excitonic transition from 1 layer-thick films of PbS:ZnO composites of varying compositions (1 layer = 35 nm for the 0 wt% film , increasing to 70 nm for the 50 wt% film, as per figure 5-5). The table shows the peak wavelength of each spectrum with the erros associated with identifying the lateral position of the peak..

The graph shows a higher PL intensity with increasing ZnO, i.e. opposite to the quenching that was expected. It is assumed that three things can happen to an exciton after generation: exciton dissociation, radiative recombination and non-radiative recombination[99]. Thus in these samples, either exciton dissociation or non-radiative recombination decreases with increasing ZnO.

A decrease in dissociation could imply that the electric field at the PbS/ZnO interface in the composite is not sufficient to cause dissociation, in which case the electron-hole pair would have to reach the charge separation region formed at the composite/ZnO planar heterojunction to dissociate. If the ZnO in the composite were not acting as a dissociation site and electron transport conduit then its presence in the composite would only act to block the pathways of electron-hole pairs through the PbS on their way to the composite/ZnO heterojunction. This would increase the probability that they will recombine across the PbS band gap.

Non-radiative recombination in the PbS film occurs via deep traps within PbS[99,255,256], caused by sulphur dangling bonds at the PbS surface[257]. EDT passivates these deep traps[99] and all devices and films have undergone the same ligand exchange steps. If the ZnO had interfered with this ligand exchange, such that the oleic acid tended to remain on the QDs, the QDs would be more confined and a blueshift with increasing ZnO would be observed. The table of figure 5-8 shows that there is no blueshift. There might be a slight redshift but this is not very significant within the errors. Furthermore the peak in absorbance of the first excitonic transition (figure 5-7) shifts slightly between devices, so any shift in the PL could be due light emitted from different devices being reabsorbed at different wavelengths. Thus there is no firm evidence for a decrease in non-radiative recombination.

In summary, an increase in radiative recombination across the PbS band gap upon increasing the ZnO fraction in the blend is seen. This points to inefficient exciton dissociation in the bulk heterojunction, with ZnO confining excitons to the PbS rather than providing a site for exciton dissociation. To explore further the effect of this hypothesised poor dissociation in the composite and reduced transport of excitons through the PbS, external quantum efficiency was measured.

5.4.2.2 External quantum efficiency as a function of bulk heterojunction layer thickness

External quantum efficiency (EQE) is a spectral map of the electronic transitions that contribute to the photocurrent. EQE examines both exciton dissociation and charge transport and it can be difficult to separate the two. To overcome this, two series of EQE measurements were performed which should result in different spectral trends according to whether dissociation and charge transport are effective or not. The trends of both experiments will firstly be described before analysis is carried out of both of them together.

Experiment 1: Different ratios of PbS vs. PbS:ZnO composite layers

In experiment 1, the external quantum efficiency (EQE) is measured for a series of 30 wt% ZnO BHJ solar cells with different ratios of PbS vs. PbS:ZnO layer thickness. The number of layers deposited was kept constant to keep the overall thickness as uniform as possible. Diagrams of the layer structures are shown in figure 5-9A.

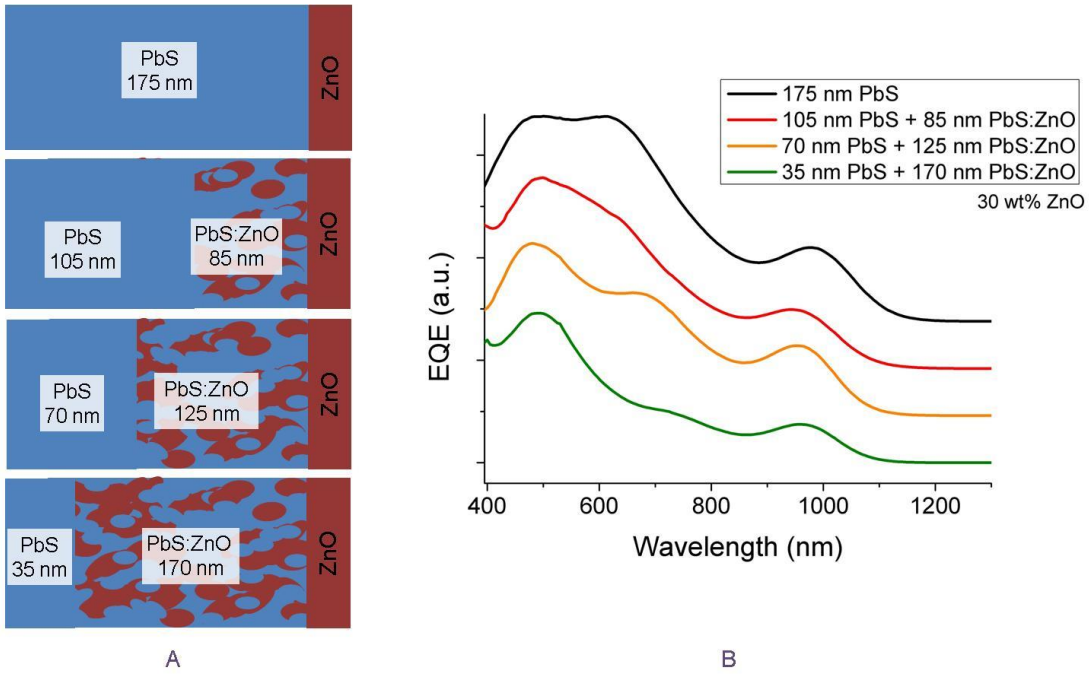

Figure 5-9: A: Structure of the active layers of the cells in experiment 1. Light enters through the PbS side. B: EQE of cells with different fractions of PbS:ZnO blend

The spectra are offset vertically to more clearly show differences in shape trends; however it should be noted that the EQE of the bilayer cell was higher overall than the ones with bulk layers, with a maximum of 15% for the bilayer device (175 nm PbS) compared with 11% for the 170 nm BHJ device. There seem to be three locations for EQE peaks. At 980 nm is the first excitonic peak, corresponding to the absorption across the PbS band gap. Extraction from higher energy states are seen at shorter wavelengths: one transition peak at around 500 nm and another at 650 – 750 nm, which decreases in magnitude and shifts to longer wavelengths with increasing BHJ thickness.

Experiment 2: Different thicknesses of PbS:ZnO composite layers

In experiment 2, the EQE is measured of a series of 30 wt% ZnO BHJ solar cells of different active layer thicknesses: 170 nm, 295 nm and 380 nm (figure 5-10A).

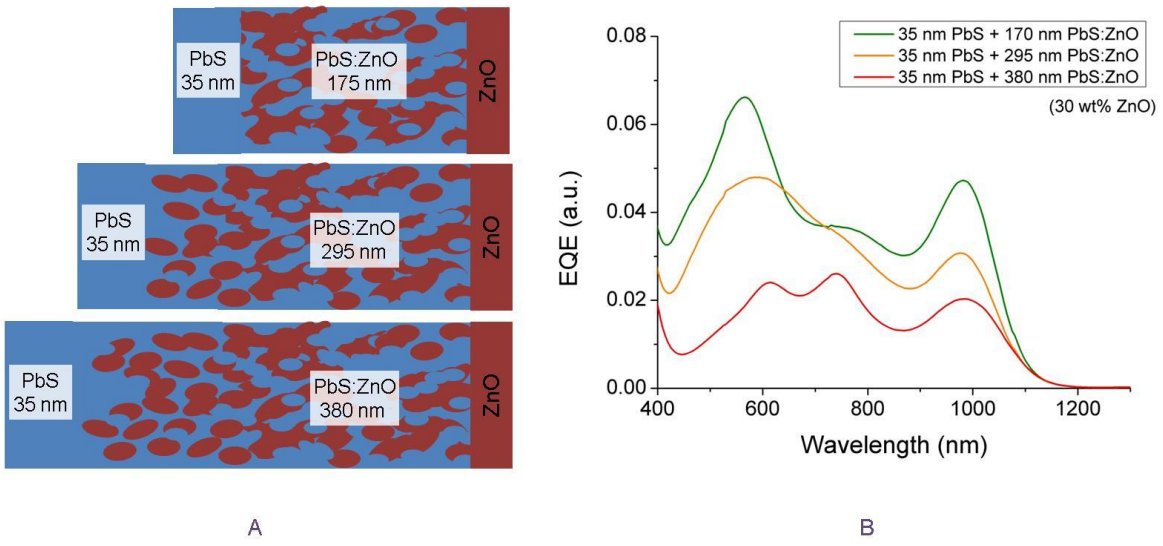

Figure 5-10: A: Structure of the devices in experiment 2. Light enters through the PbS side. B: External quantum efficiency of 30wt% ZnO BHJ solar cells as a function of device thickness.

As for experiment 1, the EQE spectra (figure 5-10B) show the PbS first excitonic peak at around 980 nm with extraction from higher PbS states seen at shorter wavelengths. All peaks decrease in intensity as the BHJ becomes thicker, but there seems to be proportionally less current from

shortest wavelength peak, with this peak also redshifting from 565 nm to 590 nm to 610 nm. In this case the peak at 750nm does not appear to shift in wavelength.

When considering EQE spectra, it is necessary to consider that photon absorption depth is wavelength dependent so different depths in the cell will absorb different wavelengths. Longer wavelength photons have a longer penetration depth than short wavelengths photons[258]. Literature values of PbS absorption coefficients[259,260] give a penetration depth of (59 ± 2) nm for 400 nm photons and (111 ± 7) nm for 900 nm photons. Penetration depths might be longer in these PbS:ZnO devices depending on the PbS QD packing density and the effect of the ZnO nanoparticles on photon path length. This phenomenon implies that cells of different of different thickness will have different absorption spectra. A thicker cell will absorb more light than a thinner one but also the absorption onset will be shifted to longer wavelengths (figures 5-11A and 5-11B). Absorbance spectra of films of different thicknesses clearly show this (figure 5-11C), with the 55 nm thick film having an absorption onset at 650 nm compared to the 280 nm thick film which starts to absorb at a wavelength of 780 nm. As before, the non-spectrally-uniform changes and long wavelengths absorption may be attributed to scattering by nanoparticle agglomerations[248] or absorption by trap states.

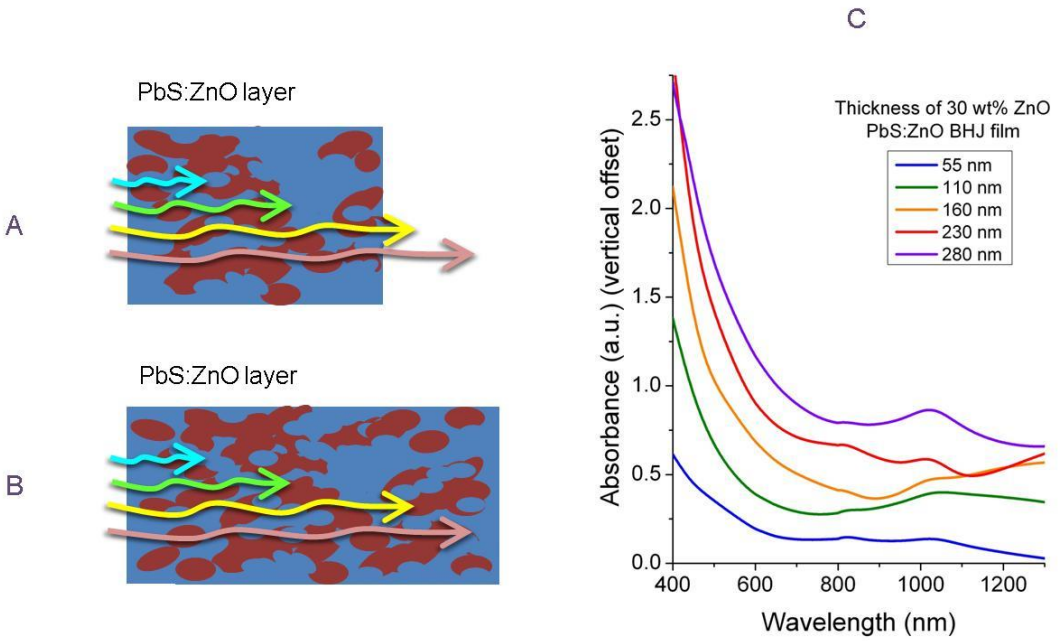

Figure 5-11: A: A thin absorbing film, in which only the short wavelength photons (blue and green arrows) are absorbed. Long wavelength photons (yellow and red arrows) pass through the film. B: A thicker absorbing film, in which longer wavelength photons are now more easily absorbed in the PbS. C: Absorbance spectra of 30wt% ZnO films (without PbS or ZnO blocking layers) as a function of film thickness. Thicknesses shown are the mean values (to the nearest 5 nm) of about 5 measurements taken on each film, measured with a DEKTAK profilometer. Standard deviations for measurements at each thickness ranged from 5 – 9 nm.

To explain the EQE spectra of both of these experiments, each wavelength range will be examined in turn. The peak in the EQE at 980 nm is associated with the peak in absorption by the PbS at that point, as this wavelength corresponds to the energy of the first excitonic transition in the PbS. In experiment 1 the peak height varies a little between samples but the, with the bilayer device having the highest peak and the complete bulk heterojunction device having the lowest peak, but with no discernible trend in between. In experiment 2 the peak height diminishes considerably as device thickness increases. If electron-hole pairs could separate at the interfaces in the BHJ and be transported efficiently to the electrodes, then an increase in this peak height would be expected. Hence, charge separation and/or transport are not efficient in the BHJ solar cells.

The peak at middle wavelengths (650 nm – 800 nm) is expected to arise from light absorbed closer to the ZnO (at least in relation to the shorter wavelength peak which is assumed to be from absorption nearer to the front of the cell). In experiment 2, the peak does not shift wavelength from

750 nm. As the devices in experiment 2 get thicker, the 750 nm wavelength photons should be absorbed further from the ZnO interface. However, the fact there are no great spectral changes in this peak (especially compared to the redshifting short wavelength peak around 600 nm) suggests that charge separation occurs, irrespective of the location of charge generation for these wavelengths. The EQE of this peak is, however, lower for the thicker cells, showing some suppression in charge separation or transport as cell thickness increases. This reduction in EQE is not as pronounced as for the strongly-absorbing first excitonic peak at 980 nm. To explain this, changes in the absorption onset are considered. Figure 5-9C shows an absorption onset at about 750 nm for a layer thickness of 280 nm. Considering the two thickest devices have greater thicknesses than this, it is likely that absorption is considerably enhanced in the middle wavelength region for the thicker cells, which will partially compensate for any increased difficulty in charge separation or transport.

In experiment 1, a much greater suppression of current is seen from this middle-wavelength region. This wavelength region corresponds to electron-hole pairs that are generated close to the charge-separating junction formed with the ZnO blocking layer, so they should have a greater probability of dissociation than those towards the front of the cell, which contribute to the EQE at around 500 nm. Yet, this 500 nm EQE peak does not change in intensity by as much as the middle-wavelength peak. So assuming that dissociation is effective for the electron-hole pairs at the back of the cell, the poor contribution to current output must relate to a problem with poor charge transport or higher recombination. Specifically, there would be poor transport of holes, which have to travel all the way through the PbS phase from the back of the cell to the PbS blocking layer (it is assumed that the ZnO interface is close enough for electrons to travel towards it). An increase in recombination could arise from the increase in PbS/ZnO interface as the PbS layer is increasingly substituted with BHJ. The proximity of hole-carrying species to electron-carrying species could result in carriers recombining after separation.

An additional feature of the middle wavelength peak in this experiment 1 is a redshift, from around 610 nm for the bilayer cell (with no BHJ) to around 700 nm for the device with 170 nm of BHJ. This could be because ZnO agglomerations are likely to scatter light[250], thus lengthening the path of light to the back of the device. This will facilitate the absorption of longer-wavelength photons. Hence, as the amount of ZnO increases in the PbS layer, charges can be generated from longer wavelength photons. This does not initially seem to agree with the lack of spectral shift seen for this peak in experiment 2, where the bulk heterojunction becomes considerably thicker. The discrepancy could be explained by the reason given for the charge suppression of experiment 1: the low charge transport in the PbS in the composite. As devices in experiment 2 become thicker, separated charges from the back of the cell (from long-wavelength photons) are unable to be extracted as there are fewer pathways through the PbS for holes to travel across the device, increasing the likelihood of recombination.

The peaks between 500 nm and 600 nm are expected to be from photons absorbed towards the front of the solar cell, closest to the PbS blocking layer (or maybe in the PbS blocking layer itself). Experiment 1 shows only a very small decrease in EQE from these peaks (from 15% to 11%). In the bilayer cell (the one with no composite layers), electron-hole pairs generated at the front of the device must diffuse to the charge separation region formed by the planar ZnO junction, or else they would not dissociate. This process does not appear to change much as the PbS is replaced with the PbS:ZnO composite. However, it must be remembered that photons are absorbed in the PbS QDs, so diffusion to the charge separation region takes place within the PbS. Considering that PbS transport seems to be poor when in the blend, it would be expected that this diffusion becomes more difficult as the ZnO fraction increases. If a depletion region in the device is in operation then charge separation might not be the issue but, still, separated electrons and holes would have to travel in the PbS phase until they reached their respective blocking layers. Therefore, it seems likely that electrons are transferred to ZnO within the blend. With this reasoning, charges generated nearer the PbS blocking layer will have more chance of extraction, as the holes do not have to travel

far to be extracted. This assumes that there are sufficient ZnO pathways for the electrons and also only a slim chance of recombination of charges in the blend. Another consideration that should be made is that dissociation could occur at the front of the cell at the PbS/ PEDOT:PSS interface in which case the ZnO must form good pathways to the cathode, however dissociation here seems unlikely given the small energy level difference between the PbS LUMO and the PEDOT:PSS work function.

Experiment 2, on the other hand, shows a marked decrease in current and redshift of EQE peaks from photons of the 500 – 600 nm region. This could occur because as the thickness of devices increases, it is more likely that charges generated at the front of the cell will recombine before reaching the composite/ ZnO interface. If charge separation can occur within the blend then this suggests that there are not enough ZnO pathways to transport the separated electrons (which is more likely as devices become thicker and pathways have to extend over a larger distance). This makes recombination of these 'long-distance' charges more feasible, as seemed to be the case for electrons travelling from the back of the device towards the PbS blocking layer.

To summarise, these EQE spectra suggest that exciton dissociation is possible in the BHJ as well as in the charge separating region caused by the junction with the ZnO blocking layer. This mix of dissociation mechanisms is supported by the work of Rath et al[93], which assumed a depletion region in a composite device but the BHJ region reduced recombination by promoting more dissociation of electron hole pairs. However, from the PL results, it seemed more likely that electron-hole pairs recombine in the PbS phase rather than dissociating via the ZnO. Maybe there is a fine balance in the BHJ between dissociation and recombination. Weaker exciton dissociation in the bulk region than at the planar junction region has been observed by Barkhouse et al.[92] and attributed to the BHJ being less able to keep charges separated than a planar heterojunction. Barkhouse proposed that a larger conduction band offset would be needed for the bulk heterojunction structure to be effective. Slight

differences in cell manufacture could mean that for one device this offset is great enough for dissociation and for another it is not.

It also seems that charge transport is poor in the bulk heterojunction devices and that there is a slight chance of interface recombination. Charge transport through the PbS phase seems to be worse than through the ZnO phase at this blend composition. This poor PbS transport theory agrees with the PL results. Charge transport is likely to be limited by morphological factors, and this will now be investigated by examining the JV characteristics and modelling percolation in the heterojunction.

5.4.3 Charge transport

External quantum efficiency has shown that charge transport seems to deteriorate with thicker bulk heterojunction layers. Transport involves diffusion of excitons to an interface or depletion region, then, once charges are separated, electrons and holes drift towards their respective electrodes. Carrier diffusion length (L_D) and carrier drift length, (L_{Dr}) are related to carrier mobility (μ) carrier lifetime (τ), thermal voltage (k_BT/q) and electric field (E) as shown in equations 5-1 and 5-2[261]:

$$L_D = \sqrt{\mu\tau\left(\frac{k_BT}{q}\right)}$$

Equation 5-1

$$L_{Dr} = \mu\tau E$$

Equation 5-2

The mobility-lifetime product is reliant upon active layer morphology and electronic trap states. Possible changes to these and the electric field upon creating a bulk heterojunction will now be discussed.

5.4.3.1 Electric field

The electric field is related to potential difference (V), by $E = \mathrm{V}/x$ where x is distance over which the potential is dropped. In a p-n junction the voltage drop of the depletion region is determined by the doping of the p- and n-sides[15]. In an excitonic cell the difference in electrode work functions dictates the voltage drop[262]. As the doping and electrode work functions are the same for all devices, the potential offset is expected to be identical for all compositions. However, this potential will be dropped across a wider area in the bulk devices as the active layers are thicker (figure 5-5). This would decrease the electric field and thus the drift length. It is also noted that a composite between two blocking layers can create a p-i-n junction[263,264], which means that the depletion region extends through the composite (but the electric field would be reduced).

These changes would result in a decrease in drift length, which should be considered alongside morphology.

5.4.3.2 Morphology

Separated charges require direct pathways without further interfaces of PbS and ZnO from the point of dissociation to the electrodes. In the BHJ, the ZnO nanoparticles could prevent a continuous network of PbS from forming and vice versa. This could lead to isolated islands of PbS or ZnO in the blend, which will decrease the mobility of carriers travelling to the electrodes. The high PL and poor EQE for BHJ structures suggest that this is happening to some extent. To study this further, series and shunt resistances through the devices will be examined to determine how conductivity changes between PbS and the PbS:ZnO blend.

Resistances

The parasitic resistance values presented in figure 5-6 are replotted here for easy reference (figure 5-12). Both resistances increase as ZnO is added; however R_{sh} seems to decrease after a cusp of

30wt% ZnO. The increase in series resistance implies that upon generation and separation, the pathway of charges to the electrodes is impeded[265], i.e. PbS percolation decreases through the cell with increasing fraction of ZnO. The shunt resistance can also reveal something about the percolation pathways through the active layer. A likely reason for a shunt current is pinholes and electrode protrusion through the absorber layers, enabling a continuous path between the electrodes[24,266], as shown in figure 5-13A. The figure shows shunt paths through the active layer and directly between electrodes. As shunt paths through the active layer depend significantly on active layer morphology, they are considered most likely to affect parasitic resistance trends. With the addition of ZnO (figure 5-13B), a continuous path via the PbS is less likely to form, so shunt resistance increases. At a critical concentration, a shunt path might be able to form via ZnO (figure 5-13C). At this point, shunt resistance can diminish. The R_{sh} trend suggests that this pattern is followed, with shunt paths forming via ZnO when it exceeds a concentration of 30 wt%.

Note that R_s does not decrease when ZnO paths form, indicating that photogenerated charge transport is limited by movement of excitons or holes through the PbS. ZnO prevents adequate PbS percolation at high ZnO weight percentages. This feature of ZnO is stronger than any benefit it might have by transporting separated electrons. Even good BHJ dissociation and perfect ZnO transport paths cannot improve short-circuit current if hole transport is poor through PbS.

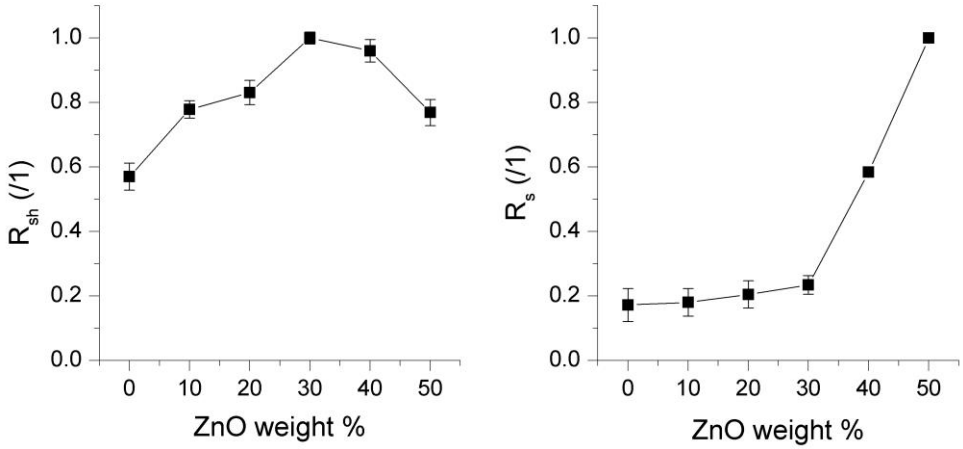

Figure 5-12: Shunt resistance (R_{sh}) and series resistance (R_s) under illumination as a function of ZnO weight percentage in the PbS:ZnO blend.

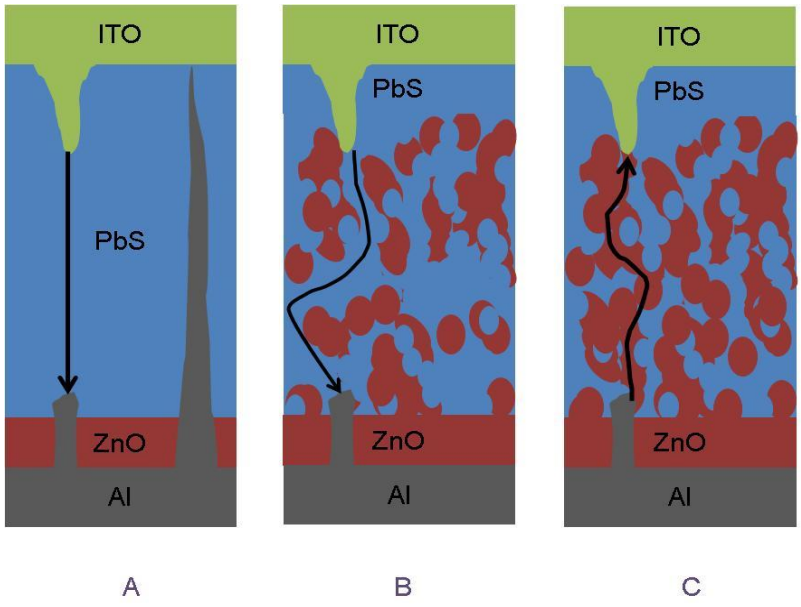

Figure 5-13 Solar cells with pinholes A: bilayer solar cell with one shunt path shown through the PbS and one directly between electrodes. B: Bulk heterojunction solar cell in which the ZnO reduces the number of the PbS pathways, so shunt paths are less likely to form. C: Enough ZnO is in the bulk heterojunction for shunt paths to form through the ZnO phase.

Percolation Model

To test this hypothesis about paths in each phase, a model of the active layers was created by Mr Simone Falco and Mr Francesco de Cola of the Department of Engineering at the University of Oxford. In the model, the PbS quantum dots and ZnO nanoparticles were represented as spheres with diameters 2.8 nm and 7.5 nm respectively, reflecting average sizes in reality. Six models were created, one for each composition tested. Each model had 4800 PbS spheres with the number of ZnO spheres varying according to composition, which represents how the PbS volume is constant whilst the ZnO varies in these devices. The spheres were packed according to a gravity model, in which the spheres were initially stacked up as shown in figure 5-14A and a model gravity was used to pull the spheres into the box at the bottom, which mimics the substrate (figures 5-14B – D). This means of packing is different from reality, in which both gravity and a centripetal force (spinning) result in the final configuration of the spheres. However it is hoped that it is still a useful model to consider. Images of each PbS:ZnO ratio are shown (figure 5-15), alongside their relative thickness, which increases non-linearly, reflecting the packing efficiency of each composition.

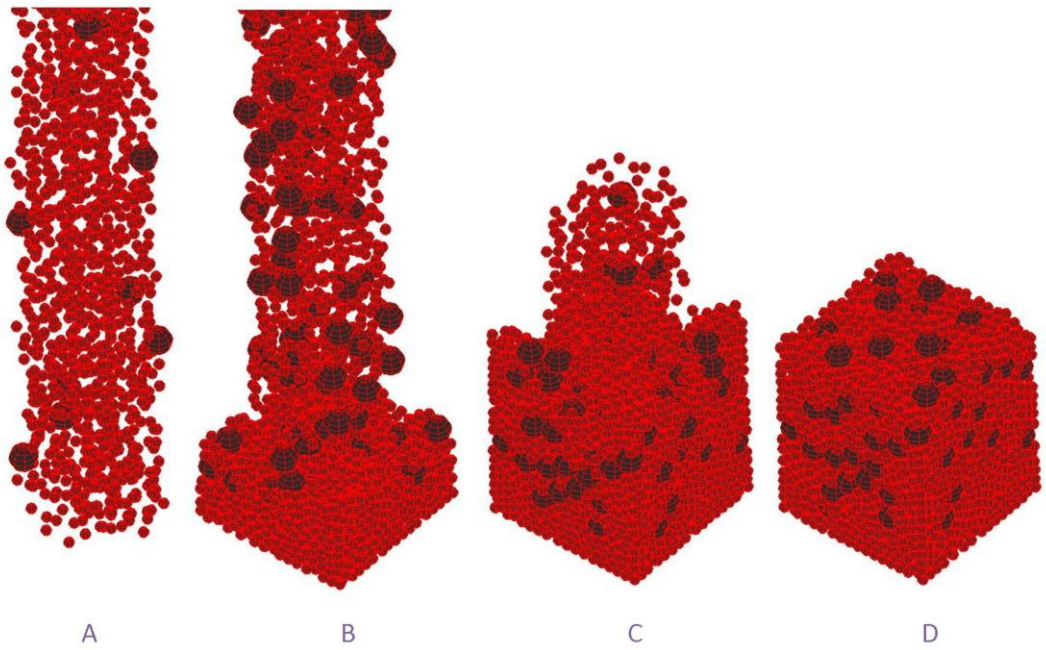

Figure 5-14: Images showing different stages of the packing process in the model, from initial condition (A) to final condition (D)

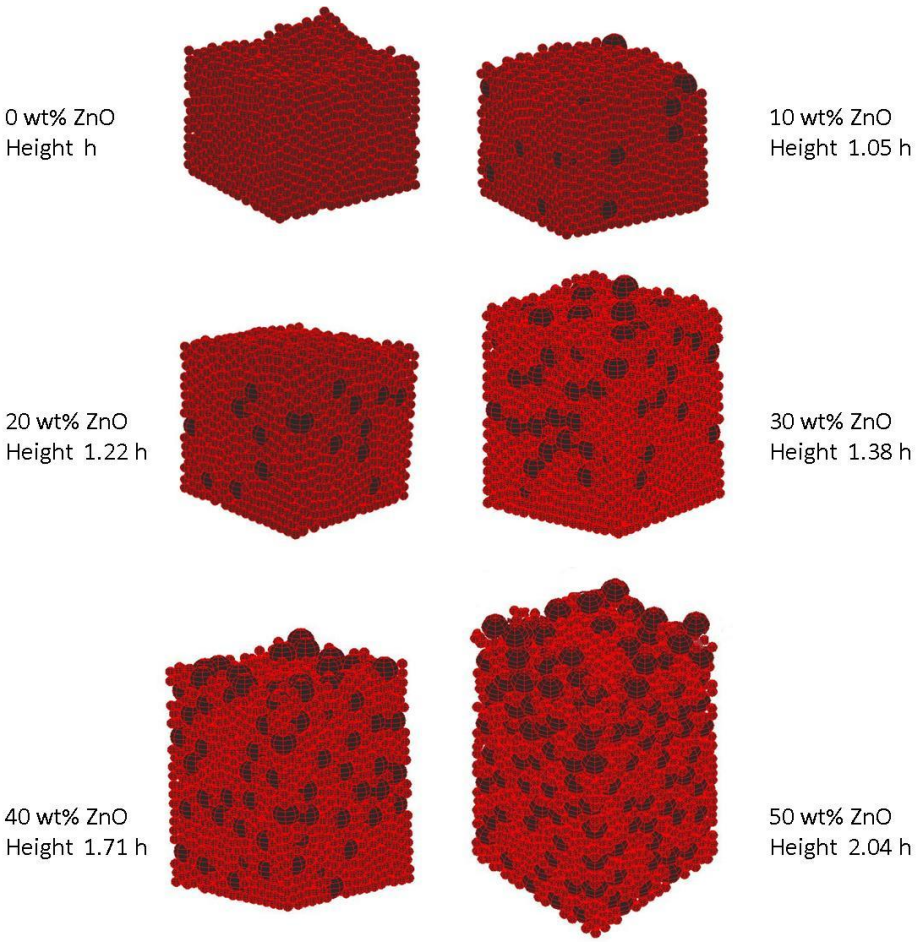

Figure 5-15: Model of bulk heterojunction active layers with the PbS shown as red particle and the ZnO shown as black particles. The weight percentage of ZnO and the relative heights of the layers are shown alongside.

Calculations performed by Scher and Zallen proposed that for a fully percolated path to form through one material phase, the volume fraction of that phase in relation to the total volume (material plus space in between particles) must exceed 15 %[267]. The expected volume fractions in the active layers of each device are shown in table 5-2. The volume fractions of each material and the total enclosing volume were obtained from the simulations. Presuming homogeneous distribution of particles suggests that continuous PbS pathways are always present in the device and that the first ZnO pathway is formed somewhere around 20 wt% ZnO. From the R_{sh} trend (figure 5-12) it is expected that the ZnO pathways would start to form after 30 wt%, suggesting non-model packing. One reason for this discrepancy could be non-homogenous dispersion of ZnO, which is a key assumption of Scher and Zallen's calculations[267] and particle agglomeration was indeed observed in AFM images (taken by Peter Kovacik). Another reason could be that even if ZnO pathways form in the 20 wt% ZnO blend, they could block more PbS pathways than the ZnO pathways that form.

Weight percentage of ZnO (%)	0	10	20	30	40	50
Volume fraction of PbS (%)	57.7	54.0	47.6	41.7	33.5	28.6
Volume fraction of ZnO (%)	0	8.3	16.2	24.2	30.5	38.4

Table 5-2: Volume fraction of PbS CQDs and ZnO nanoparticles

Examination of the parasitic resistances and the model of the composites suggest that at least 20 wt% ZnO is needed to create ZnO pathways between the blocking layers. Shunt resistance measurements show that the formation of ZnO pathways negates the blocking of PbS pathways at between 30 and 40 wt% ZnO. Despite the rise in dominance of ZnO pathways at this point, series resistance increases greatly, suggesting that charge transport is limited by the PbS phase. Thus the bulk heterojunction does limit charge mobility in the PbS and careful tuning of the components and structure is required to minimise the impacts of this.

5.4.3.3 Trap states

Another factor that reduces charge mobility is trap states[256], and PbS has both shallow and deep traps. If charges fall into shallow traps then they can be re-excited to the energy band, resulting in an increase in charge lifetime[261] and a net negligible impact on drift and diffusion length. In this system, the photoluminescence of section 5.4.2.1 seemed to indicate some radiative recombination from shallow traps rather than re-excitation, although the relative densities of shallow traps between different device compositions are difficult to determine from the PL spectra alone. If charge transport through the devices worsens as the ZnO content increases, as suggested by the PL and EQE, then a possible consequence is that charges instead recombine via these PbS shallow traps. Deep traps are passivated when the oleic ligands are replaced with 1,2-ethanedithiol (EDT) ligands[99]. If EDT were to react with ZnO[268] rather than PbS then fewer PbS deep traps would be passivated. However, the photoluminescence of section 5.4.2.1 did not show any evidence for the ligand exchange being poorer in ZnO-rich devices. In the ZnO phase, if electrons at an interface can be trapped by PbS mid-gap states[119] to subsequently recombine, then the mobility-lifetime product would be lower than if there were no PbS at all.

Despite no firm evidence yet of any change in trap state density, ideality factor values presented in section 5.5.2.2 will show that slightly more charge trapping does occur when there is more ZnO in the devices.. Whether these PbS/ZnO interfaces are favourable or unfavourable to device performance depends on whether the bulk heterojunction increases exciton dissociation and can transport more charges to the electrodes than can recombine at the interfaces or via more traps.

5.4.4 Summary

The bulk heterojunction structure was expected to increase short circuit current output by increasing the probability of exciton dissociation. The short circuit current was seen to be stable for ZnO fractions 0 – 30 wt% and then to decrease when the proportion of ZnO exceeded 30 wt%. Exciton dissociation and transport of charges to the electrodes were examined to identify the root of this decrease.

Photoluminescence showed more radiative recombination from PbS QDs when they were combined with ZnO, indicating reduced electron-hole pair separation and more recombination across the PbS band gap. However, the external quantum efficiency of 30 wt% ZnO BHJ devices did show some excitonic dissociation and transport of these separate charges in the BHJ (figure 5-9). As suggested by Barkhouse et al.[92], perhaps a greater conduction band offset is needed in the composite to counteract any increased recombination and modifying the materials to test this theory would be a good starting point.

Once excitons are dissociated, charges need pathways to travel to the electrodes. ZnO blocks PbS pathways, as shown by the increase in series resistance with increasing ZnO (figure 5-12) and as suggested by the EQE. The percolation model suggests that – in an ideal system - ZnO pathways will form at 20 wt%, with shunt resistance values (figure 5-12) showing evidence of them by 30 wt% ZnO concentration. Despite these ZnO pathways, series resistance increases greatly past 30 wt% ZnO, which suggests that charge transport is limited by the PbS phase and that charge transport through the device is the limiting factor on short circuit current, which concurrently decreases. An imaging study of the two phases around 20 wt% and 30 wt% ZnO would be useful to firmly identify problems with morphology. In particular, it should check whether PbS and ZnO pathways are clearly forming across the device and whether domain sizes are less than the exciton diffusion length (or less than the diffusion length plus depletion width if a depletion region forms). AFM was attempted by Cheng Cheng for a few concentrations and two phases were seen but the images were not clear enough to

confirm lateral percolation. Cross-section TEM was also in considered but difficulties in making the microscope samples prevented this from being fruitful.

5.5 Open circuit voltage

The higher V_{OC} for the BHJ devices shows promise for higher efficiency. Identifying its origin would be a step forward in refining CQD BHJ solar cell design. The value of the open circuit voltage is attributed to two general factors: energy level changes and changes in recombination.

The open circuit voltage across an illuminated p-n junction, is equal to the difference in electron and hole quasi-Fermi levels (E_F)[22,38], as shown in figure 5-16A. For an excitonic junction V_{OC} could be any value up to the difference in PbS VB- ZnO CB difference[269,270] (figure 5-16B).

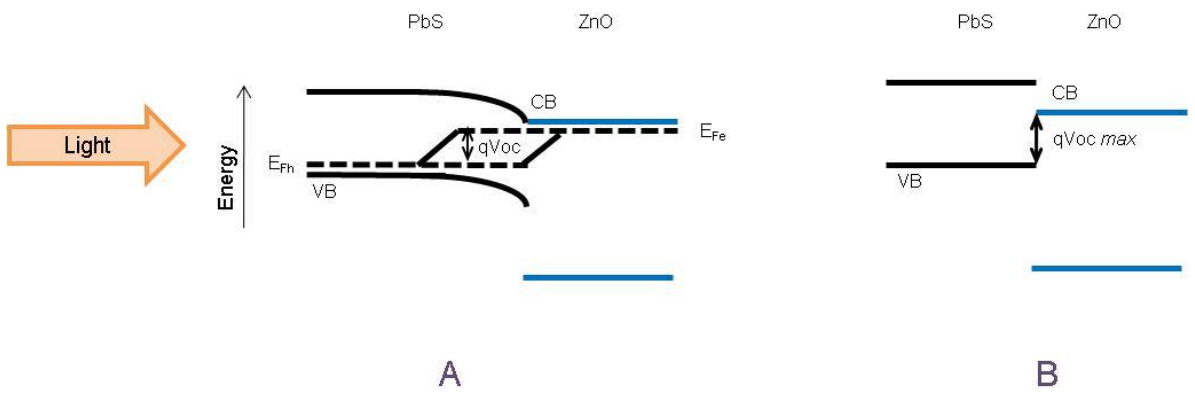

Figure 5-16: Open circuit voltage, V_{OC}, for A: a p-n PbS-ZnO junction and B: an excitonic PbS-ZnO junction. Conduction bands (CB), valence bands (VB) and quasi electron and hole Fermi levels (E_{Fe} and E_{Fh}) are marked as appropriate.

Whatever the dominant charge transport mechanism, if the conduction band edge of ZnO rises or the valence band edge of PbS lowers then V_{OC} will increase. Additionally for the p-n case, V_{OC} will increase if ZnO becomes more n-type or PbS more p-type. Section 5.5.1 will state causes of energy level changes that could come about by the blending of PbS with ZnO, with the aim of determining whether any of these changes could result in the V_{OC} trend observed.

The voltage at open circuit is also, by definition, that which is formed when no current flows through the device. This is true when photocurrent (J_{ph}) and dark current (J_{dark}) are equal in magnitude, thus cancelling each other out. For devices with charge diffusion lengths much larger than the active layer thickness[228] photocurrent is assumed to be independent of bias and equal to the short circuit current. This is because charge extraction is expected to occur easily with no heavy reliance on the electric field to ensure charges can drift to the electrodes before recombination. In BHJs this is often not the case, with the random networks causing disorder that reduces charge mobility[228]. If this is the case for the devices in this chapter, and there is a decrease in photocurrent extraction with forward bias, as observed for various types of solar cells in the past[226–228], then V_{OC} will diminish.

An increase in dark current will also act to diminish V_{OC}. Dark current is a recombination current and thus an increase in dark current implies higher recombination. This can be quantified by measuring reverse saturation current (J_0), which measures the extent of recombination and ideality factor (n), which defines the recombination process[219]. As shown in equation 5-3, which is the diode equation rearranged for V = V_{OC}, and as illustrated in figure 4-15 (in chapter 4), increasing n will increase V_{OC} whereas increasing J_0 will decrease V_{OC}.

$$V_{OC} = \frac{nk_BT}{q}\left(\ln\left(\frac{J_{ph}}{J_0}\right) + 1\right)$$

Equation 5-3

Dark current and photocurrent changes will be explored in section 5.5.2. Firstly, possible energy level changes are outlined.

5.5.1 Possible causes of energy level changes

5.5.1.1 Interaction of EDT with ZnO

It has been reported that EDT treatment can change the energy levels of lead chalcogenide: ZnO blends[12,268]. During device fabrication, the ZnO in the PbS:ZnO blend is exposed to the EDT used for

PbS oleic acid-to-EDT ligand exchange. The ZnO surface is very reactive and, according to Timp and Zhu[268], it can react with EDT to cause a rise in oxygen vacancies, which act as surface trap states on the ZnO. Thus, the ZnO in the blend might have different energy levels from the ZnO blocking layer.

Fourier-Transform Infrared spectrometry (FTIR) measurements of ZnO films with and without EDT treatment were performed by Cheng Cheng, (figure 5-17). The absorption between 2800 cm^{-1} and 3000 cm^{-1} that is only present in the post-EDT treated ZnO film is attributed to the C-H bonds in EDT[241] and confirms that EDT is present on the film, despite having attempted to wash unreacted EDT from the film with methanol. Kelvin Probe (KP) analysis also performed by Cheng Cheng shows that this change makes ZnO less n-type, with a Fermi level 0.15 eV lower in EDT-treated ZnO than ZnO without EDT. This would be expected if EDT has induced surface traps in the ZnO band gap, which could capture electrons that would otherwise be in the conduction band, thus reducing the Fermi level. This opens up the possibility that the EDT that remains on the ZnO film could have reacted with it.

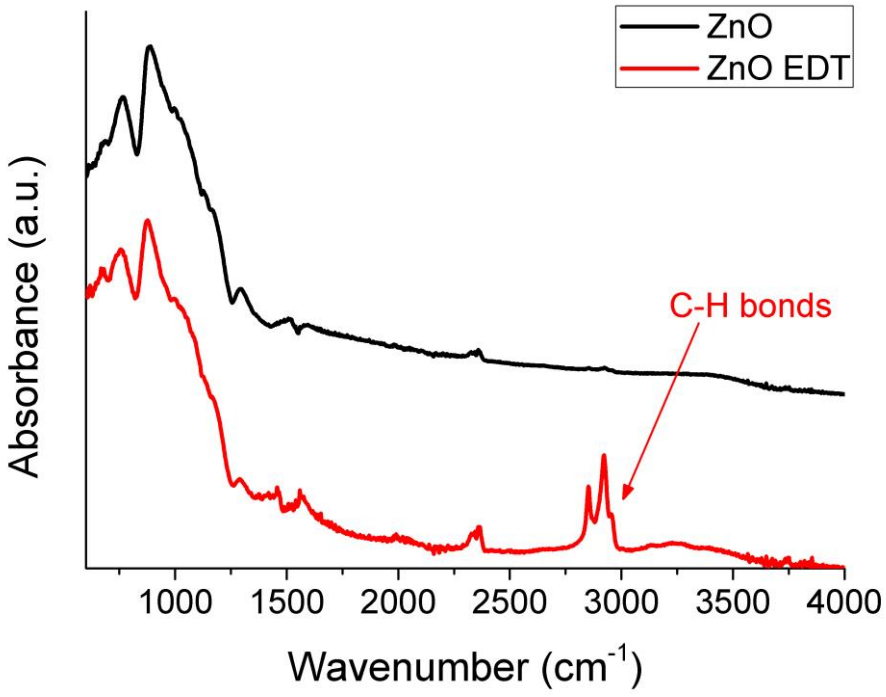

Figure 5-17: Fourier Transform Infrared Spectrum of ZnO film (black) and ZnO film after exposure to EDT (red).

The effect of the ZnO Fermi level change on the PbS Fermi level in the blend was not tested as it would be impossible to determine which phase in a composite film was being tested given the resolution of the Kelvin probe. However, Timp and Zhu further propose that the VB of lead chalcogenide QDs can pin to the ZnO oxygen vacancy surface states[268]. To prove this they examined the interaction of PbSe QDs of different sizes with EDT-treated ZnO. If there was no interaction between the PbSe QDs and the ZnO then as QD size changes the CB and VB would shift equally away from the Fermi level (as it does when with TiO_2[268]). However, the VB of both sizes of QD was found to be in the same energy position, thus the pinning in effect appears to raise the PbS VB maximum (figure 5-18).

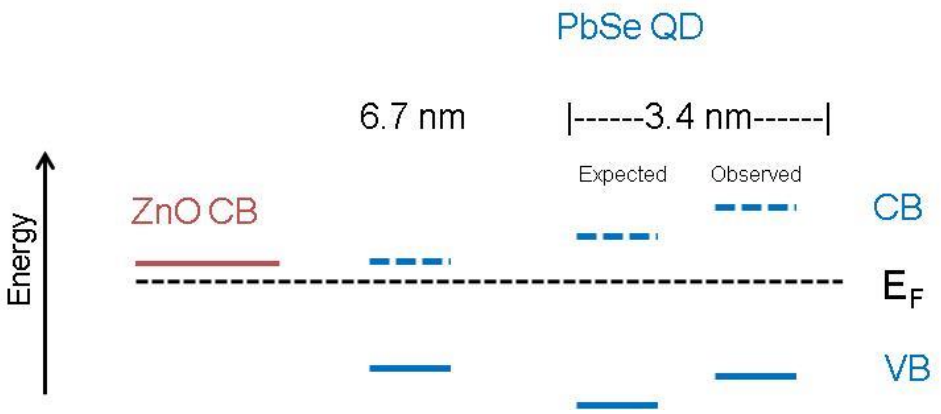

Figure 5-18: Adapted from Fig 5. Timp and Zhu[268]. Energy level diagrams summarising the measured energy alignment of 6.7 nm EDT-treated PbSe QDs with ZnO and, from this, the expected energy alignment of 3.4 nm EDT-treated PbSe QDs with ZnO. The measured alignment for the 3.4 nm QDs is shown on the right. CB: dashed line, VB: solid line.

The effect of EDT treatment can be summarised as making ZnO less n-type and raising the CB and VB of PbS. Both of these changes would act to decrease the V_{OC}. In this study, the cells with EDT-treated ZnO (the PbS:ZnO bulk heterojunction cells) show a higher V_{OC}, contrary to what would be expected from the energy level changes discussed above. Thus EDT treatment is not the cause of the V_{OC} changes measured. In a quantum dot, energy levels can also change as a result of changes in confinement. This will be discussed in the next section.

5.5.1.2 Quantum confinement

Having ZnO dispersed within a PbS film results in PbS QDs being on average further away from each other. This might be expected to decrease wavefunction overlap between QDs and thus increase their quantum confinement. This would result in a larger PbS band gap and thus a blueshift of the excitonic peak, as occurs when long ligands separate the dots[256]. A larger PbS band gap would increase the open circuit voltage. However, photoluminescence from the first excitonic PbS transition shows no such shift with increasing ZnO (figure 5-8), indicating no increased confinement or reduced coupling of PbS CQDs.

To conclude, there are two mechanisms that could change energy levels: EDT treatment, and ZnO changing the quantum confinement of PbS CQDs. EDT treatment should act to decrease the PbS VB – ZnO CB energy gap, which would act to decrease V_{OC}, and photoluminescence measurements (figure 5-8) showed that ZnO did not increase quantum confinement. As V_{OC} initially increases as ZnO is added to the composite (up to 30 wt% ZnO) then a simple explanation of a change in V_{OC} arising from a change in the energy levels would not seem to apply.

5.5.2 Current density – voltage (JV) analysis

5.5.2.1 Dark current and photocurrent

Section 5.5.1 indicated that the energy levels of the bulk PbS:ZnO devices are not changed from the bilayer case in any way that would result in a higher open circuit voltage. The alternative reason for the V_{OC} increase up to 30 wt% ZnO is a decrease in dark current, synonymous with a decrease in recombination. This assumes a constant photocurrent, an assumption that will be checked in this section.

Dark current density-voltage measurements for ZnO concentration-varying devices are shown in figure 5-19.

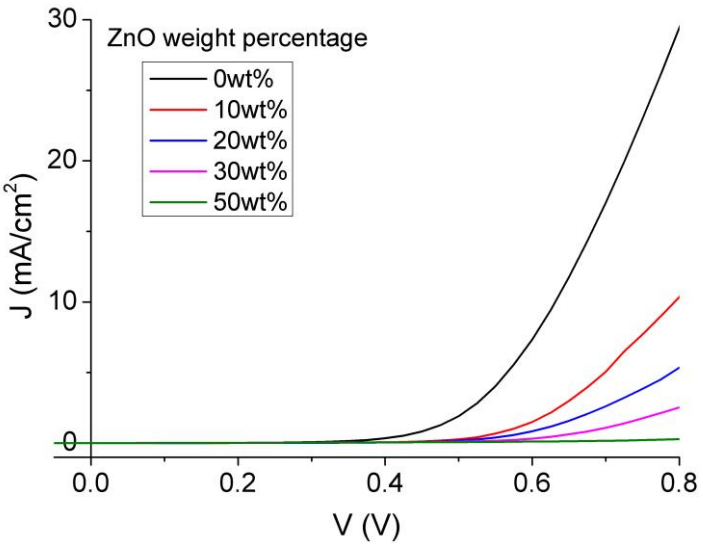

Figure 5-19: Dark JV curves for PbS-ZnO devices in a batch of devices of different PbS: ZnO compositions, with ZnO weight percentage shown in the key.

The dark current is seen to decrease from the bilayer case (black curve) to the 50 wt% ZnO BHJ case (green curve). This supports the notion that the reduction in dark current and recombination is responsible for higher V_{OC} for the BHJ devices, although the behaviour at high ZnO weight percentages shows that dark current alone cannot explain the V_{OC} trend. V_{OC} falls when ZnO weight percentage exceeds 30 wt% (figure 5-6) and yet all the higher ZnO weight percentage devices measured had the lowest dark current. As V_{OC} is the balance between dark current and photocurrent, in order to understand this discrepancy, photocurrent density-voltage curves of the above devices are examined.

The photocurrent density – voltage curve (J_{ph}-V curves) is simply the illuminated JV curve minus the dark JV curve, as shown in the example for the bilayer (0 wt% ZnO) device (figure 5-20). J_{ph}-V curves for all concentrations are shown in figure 5-21 along with the dark JV equivalents of figure 5-19 reproduced for easy comparison.

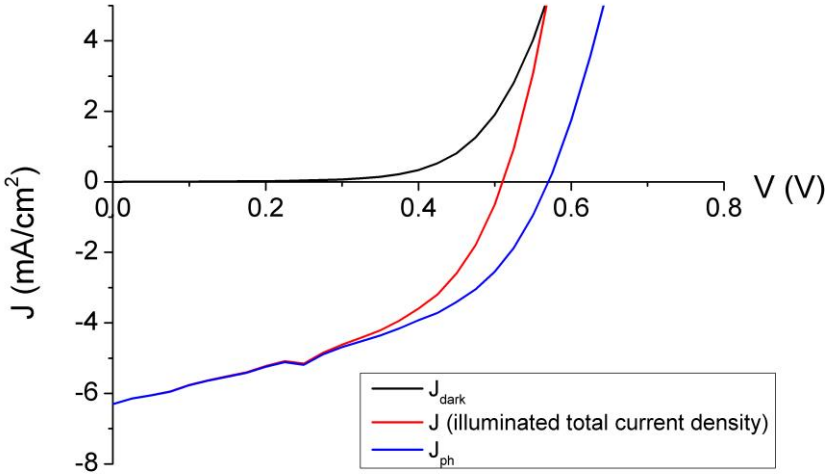

Figure 5-20: Bilayer (0wt% ZnO) solar cell showing dark (black), light (red) and photocurrent (blue) JV curves.

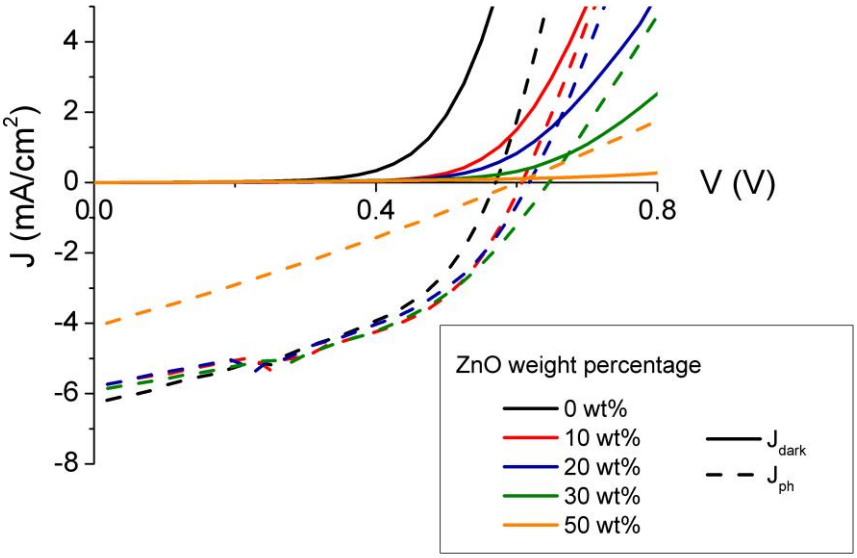

Figure 5-21: Photocurrent density (dashed lines) and dark current density (solid lines) as a function of voltage for PbS:ZnO solar cells with a range of ZnO weight percentages.

Photocurrent is clearly bias dependent, reducing as forward bias increases. From 0 wt % to 30 wt% ZnO, photocurrent becomes less bias dependent. A lower photocurrent, with the same dark current, would result in a lower V_{OC}. Therefore, increasing ZnO to 30 wt% causes the photocurrent trend to be less detrimental to V_{OC}. However, for the 50 wt% device, photocurrent is always very low, which acts to decrease V_{OC}.

The decrease in photocurrent with bias indicates a reduction in carrier collection efficiency with bias. This has been correlated with drift length[227,228,271]. Carrier drift length will decrease as the electric field decreases (equation 5-2)[272]. Therefore it is important for the ratio between drift length and active layer thickness to be as high as possible[226]. Drift length is proportional to mobility and lifetime (equation 5-2)[272] so photocurrent from samples with poor mobility-lifetime products will reduce at a lower bias. Section 5.4.3.2 concluded that as ZnO increases in these devices the mobility-lifetime product decreases, which would present the opposite photocurrent - bias trend with blend composition to what is seen.

Another possibility is that bias dependence can be attributed to material photoconductivity[273], in which photogeneration of carriers causes an increase in free carrier density. These extra carriers render recombination more likely and can also can decrease the parasitic resistances from their dark values[238,274–276]. From the gradients of the curves at V = 0 in figure 5-20, it indeed appears that shunt resistance is lower when the cell is illuminated. The differences in the photocurrent curves can be explained by this theory: if light reduces the shunt resistance of a device with an already large shunt resistance, it will result in less of a photocurrent change than if the shunt resistance of a lower shunt resistance solar cell would reduce by the same factor. Thus the photocurrent of the 30 wt% ZnO solar cell, which has the highest R_{sh} (figure 5-6), would be less bias dependent than the ones of lower and higher ZnO concentration.

From 0 – 30 wt% the dark current of each composition is very different, much more so than the difference in photocurrent across the different compositions (figure 5-21), so it affects V_{OC} more than the photocurrent change. For the 50 wt% device the photocurrent is quite distinct from the other composition and the device has a fairly flat dark JV curve. This could be because the 50 wt% cell has a much higher series resistance than the other devices (figure 5-6). If the series resistance is much greater in the dark than in the light, the dark JV curve will be much flatter than the illuminated JV curve so will have little impact when subtracted from the illuminated JV curve to obtain the

photocurrent values. This means the J_{ph} – V curve almost replicates the illuminated JV curve. The almost linear nature of the photocurrent curve is due to the poor fill factor of the illuminated JV curve, caused mainly by the very high series resistance. Also as the photocurrent of the 50 wt% ZnO device is inherently lower than for the other devices (its J_{sc} is lower) then this would also act to lower the V_{OC}. In order to determine the cause of the rise in V_{OC} from 0 - 30 wt% ZnO, the next section will primarily discuss why the dark current decreases with ZnO concentration up to 30 wt% ZnO, except for where analysis will benefit understanding of devices of higher ZnO composition.

5.5.2.2 Dark JV analysis 0 – 30 wt%

To understand the cause of the differences in dark current it is necessary to identify its components.

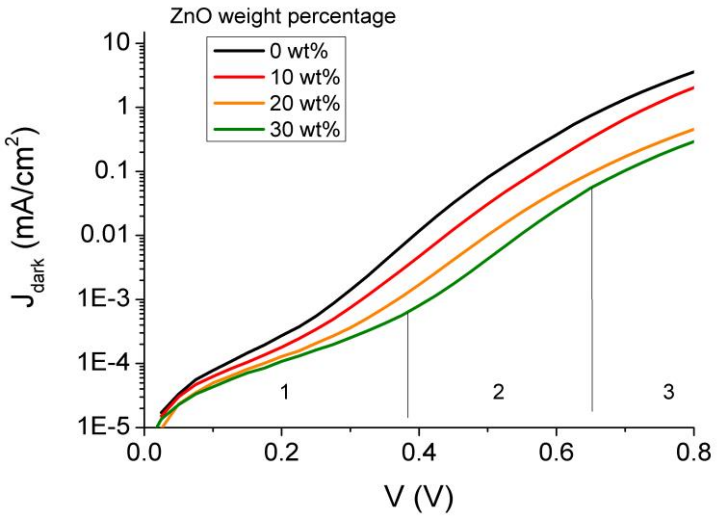

Figure 5-22: Dark JV curves for devices containing 0 wt% - 30 wt% ZnO in the blend. Current density is plotted on a logarithmic scale.

For devices with up to 30wt% ZnO concentration there are three distinguishable sections of the dark JV curve, as delineated in figure 5-22. In the mid-bias region (region 2), diffusion current dominates. At these biases, majority carriers diffuse with little impedance across the junction to the oppositely-doped side, where they become minority carriers and recombine with majority carriers. Anything to

increase the magnitude of this recombination will increase the diffusion current. The flattening at very high bias (region 3) is a result of series resistance impeding current flow. The additional current that dominates at low bias (region 1) can be explained by shunt current, a second diode current or a combination of both. The main reasons given for a second diode are depletion region recombination[277] and the formation of a Schottky junction at the electrode-active layer interface[12,278]. In this case, the possibility of a p-n junction lends itself to the depletion region explanation. To determine whether the 'second diode' depletion region recombination current or shunt current prevail at low bias, the current density – voltage relationship in this region is examined.

Depletion region recombination and shunt current have different relationships with bias. Equation 5-4 shows the complete dark diode equation including parasitic resistances (R_s and R_{sh} given in units of Ωcm^2) and a depletion region recombination term (middle term). The one-diode dark JV equation assuming no influence from parasitic resistances is shown in equation 5-5 for comparison. Dark diffusion current parameters are indicated by the subscript 'diff', whereas dark depletion region recombination current parameters are indicated by the subscript 'dep'. This shows that depletion region recombination has an exponential relationship with bias whereas shunt resistance is linear with bias.

$$J_{dark} = J_{0_{diff}}\left(e^{\frac{q(V-JR_{s)}}{n_{diff}k_BT}} - 1\right) + J_{0_{dep}}\left(e^{\frac{q(V-JR_{s)}}{n_{dep}k_BT}} - 1\right) + \frac{V - JR_s}{R_{sh}}$$

Equation 5-4

$$J_{dark} = J_{0_{diff}}\left(e^{\frac{qV}{n_{diff}k_BT}} - 1\right)$$

Equation 5-5

A fit of the curves to either the depletion region recombination term or the shunt resistance term is shown for the bilayer cell and 30 wt% ZnO BHJ cell (figure 5-23). The grey dashed line represents a

single diode with no parasitic resistances (with reverse saturation current (J_{0diff}) and ideality factor (n_{diff}) extracted from measured data). The pink and blue dotted lines represent the inclusion of shunt current and second diode current, respectively. The shunt resistance, R_{sh}, and second-diode parameters, J_{0dep} and n_{dep}, are taken from values fitted to the measured dark data as if only one or the other were present. The graphs show that shunt resistance offers a better match to the real curves, thus this is the parameter that dominates at low bias and depletion region recombination can be neglected.

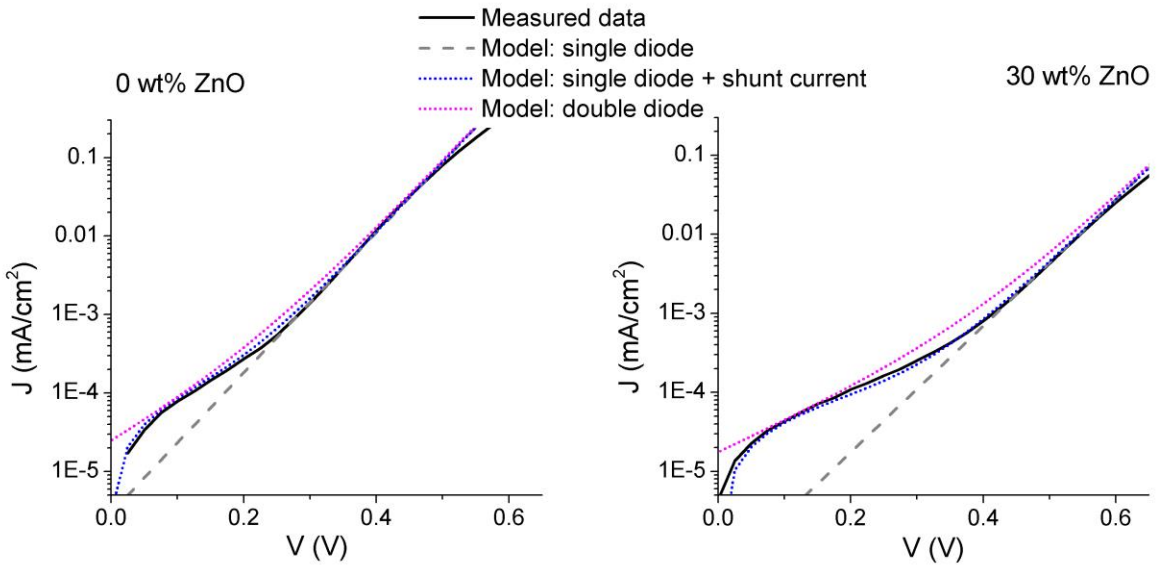

Figure 5-23: The components of the dark JV curves of PbS:ZnO solar cells with 0 wt% ZnO and 30wt% ZnO. The black solid curve is the measured data, the grey dashed line is the single diode model with no parasitic resistances and the blue and pink dotted lines are the models including shunt current and a second diode respectively.

Although R_{sh} and R_s dominate and low and high bias respectively, the position and slope of the dark JV curve is mainly influenced by the diffusion current. To identify the root of changes in diffusion current, the dark current parameters, namely reverse saturation current and ideality factor, will be examined.

Dark current parameters

Dark current parameters were extracted from the mid-bias region of the curves by fitting to the one-diode dark JV equation (equation 5-5) after shunt resistance was taken into account. J_0 was calibrated across the batches of devices and values were scaled to a maximum of 1, as performed for the light JV parameters in section 5.3. The ideality factor did not vary much between batches and so the average value of n is given.

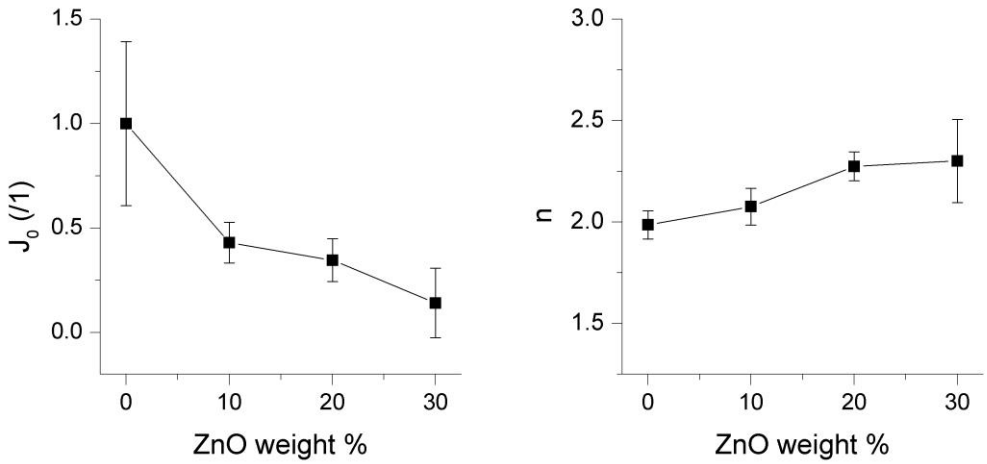

Figure 5-24: Dark JV parameters. Reverse saturation current (J_0) were calibrated across the batches and values shown are scaled to a maximum of 1. Ideality factor (n) were calibrated across batches and scaled to the mean average of the ideality factor of the bilayer device, in order to give an indication of the values. Errors shown are fitting errors but ideality factors never deviated outside of 1.75 (bilayer) and 2.5 (30 wt% ZnO).

Figure 5-24 shows that J_0 of the bulk devices is lower than that of the bilayer and n of the bulk devices is generally higher than that of the bilayer. Both of these trends act to diminish the dark current in the bulk devices (equation 5-3).

Reverse saturation current

The lower J_0 of the BHJ cells implies that fewer injected charges diffuse across the heterojunction to become minority carriers and recombine with the majority carriers in the opposite phase. Possible reasons are that there are electronic energy level barriers to diffusion[279,280], there is a reduction of

traps which reduces recombination[220] or that more selective charge movement occurs, reducing the possibility of direct injection of minority carriers into materials[281].

All devices have the same energy levels at the electrode/ blocking layer interface, so a change in the electronic barriers to injection from electrodes is unlikely.

A reduction in the density of any traps that act as recombination centres would reduce recombination and thus reduce the diffusion current[220]. However, as discussed in the next section, the increase in ideality factor suggests the opposite is true, i.e. that trap density might increase.

Direct injection of minority carriers - holes into ZnO and electrons into PbS – is caused by pinholes forming through the blocking layers in solar cells. Such pinholes are characterised by shunt resistance, as portrayed in figure 5-14. As figure 5-6 shows, shunt resistance increases as ZnO concentration increases, implying a reduction in minority carrier injection. This would explain the decrease in J_0. Such correlations between shunt resistance and reverse saturation current have been observed in other systems[281,282] and also attributed to a decrease in recombination via shunts.

A plot of R_{sh} vs. V_{OC}, for all compositions tested, shows a great similarity (figure 5-25). A small R_{sh} should theoretically decrease V_{OC}[283] and the link has been seen experimentally[284]. Thus the V_{OC} increases because minority carriers are no longer injected into PbS at forward bias, which is reflected in the shunt resistance.

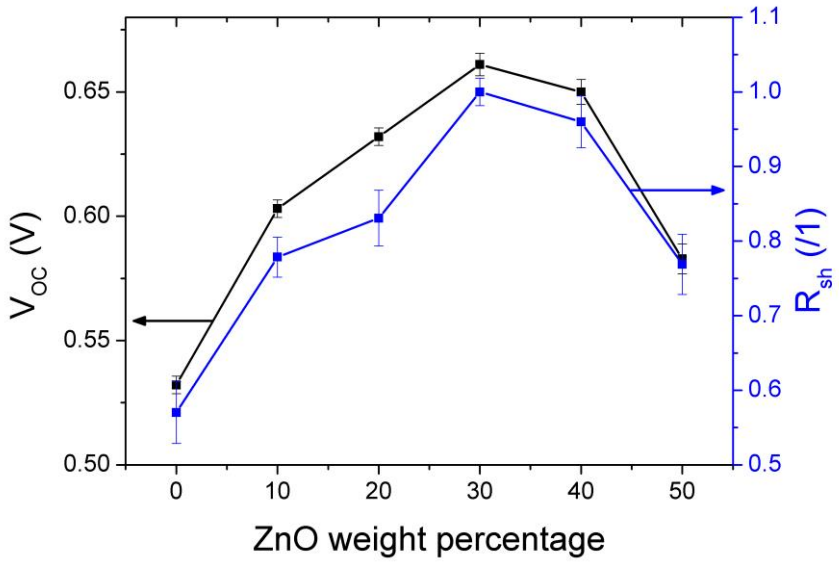

Figure 5-25: V_{OC} and R_{sh} of devices as a function of ZnO weight percentage. Calibrated average values are shown with errors corresponding to errors across one batch.

Ideality factor

Figure 5-24 shows that all cells are far from ideal with ideality factors around 2.0 suggesting that trap-assisted recombination is prevalent. This is not unexpected in PbS QDs[285] due to the high density of traps caused by dangling bonds at the surface of the quantum dots[257,286]. The ideality factor increases as the ZnO content increases, indicating a higher density of recombination-inducing traps. As stated in section 5.5.1.1, ZnO might reactwith EDT thus limiting PbS trap passivation. Ehrler et al.[119] showed that electrons within ZnO that are at a PbS/ ZnO interface can be accepted by lower energy PbS mid-gap states. Furthermore, studies have shown that charges on the ZnO often recombine via trap states in the ZnO species[287,288], a process which would increase the ideality factor.

5.5.3 Summary

Energy level changes are not responsible for the changes in V_{OC} with blend composition. EDT could change energy levels of ZnO and PbS but only in such a way as to decrease the open circuit voltage. No confinement change in PbS is seen upon adding ZnO, so no energy level change is obtained via this route.

Dark current and bias-dependence of photocurrent do change with blend composition. The dominating factor up to 30 wt% dark current is the decrease in dark current, which originates from a decrease in reverse saturation current and an increase in ideality factor. The reverse saturation current is likely to decrease because fewer minority carriers are injected into the materials via shunting, as evidenced by the shunt resistance measurements. The increase in ideality factor as the ZnO fraction increases implies that a higher proportion of trap state recombination can take place. With a greater proportion of ZnO and a greater PbS/ ZnO interface area, this can originate from either charges on ZnO recombining via ZnO traps or by capture onto PbS traps. At the highest ZnO concentrations the high series resistance causes a low J_{sc} and limits photocurrent collection, resulting in the rapid decrease of photocurrent with forward bias. This photocurrent changes more rapidly than the dark current at this concentration so has more influence on the V_{OC}.

Thus to keep the high $V_{OC,}$ experienced by 30 wt% ZnO BHJ cells, reducing recombination is key. One way to do this is to reduce shunt paths which can increase dark current. This could be achieved by making blocking layers thicker[238], to reduce the probability of electrodes protruding into the active layer. Furthermore, the bias-dependency of the photocurrent should be reduced. The bias-dependency is a result of the parasitic resistances through the device. Whilst the extra blocking layers would improve shunt resistance, series resistance can only be improved with more ideal blend morphology and better energy level alignment to allow for easier exciton dissociation[92].

5.6 Conclusions

Different compositions of PbS:ZnO bulk heterojunction solar cells were manufactured. Some efficiency improvement was observed when a 30 wt% ZnO composition was used, attributed to an increased in open circuit voltage, largely due to a reduction in dark current as a result of fewer shunt pathways. However, the expected increase in exciton dissociation efficiency and short circuit current did not materialise. External quantum efficiency spectra suggested that exciton dissociation in the bulk heterojunction can occur, but this process was not obvious from the photoluminescence measurements. Furthermore, charge transport through the BHJ, particularly in the PbS phase, seemed to be hampered by the presence of ZnO.

To improve the possibility of exciton dissociation in the BHJ, a greater conduction band offset between PbS and ZnO might be key[92]. This could be achieved by fabricating smaller PbS quantum dots with larger band gaps – currently PbS quantum dots as small as 1.5 nm in diameter have been fabricated[289], which have a band gap of 2.6 eV. To fully understand the driving forces on photogenerated electron-hole pairs, it should be determined exactly whether a p-n, p-i-n or excitonic junction forms in the BHJ device. A way to start this study could be do perform impedance spectroscopy to measure the depletion width[112] (if there is one). To increase current further, charge transport needs to be improved, i.e. series resistances through the devices should be minimised, keeping in mind that shunt resistance should stay high. A morphological study would be useful to identify how percolation pathways can be improved to reduce series resistance, and whether PbS/ZnO interfaces form within the exciton diffusion length (or depletion width for the p-n case). Furthermore, thicker blocking layers could be used to increase shunt resistance[238].

6. Graphene as the transparent electrode for squaraine/ C_{70} solar cells

6.1 Introduction

In the previous chapter the implementation of quantum dots as absorber layers in solar cells was discussed. This chapter will examine graphene as a transparent conductor. Like the zero-dimensional quantum dots, graphene's electronic properties are defined by its two dimensional quantum confined structure [150,160,290,291].

Graphene sheets are one-atom-thick hexagonal structures of carbon. This configuration results in a unique electronic structure. Other crystal arrangements (including 3D graphite) have parabolic energy (E) – momentum (p) relationships[292], implying non-zero effective electron and hole masses[27]. Graphene, on the other hand, is a zero band gap material[293] with energy bands exhibiting a linear $E-p$ relationship, $E = v_F p$, as if the electrons were massless[147]. v_F is the Fermi velocity of the electrons, which is equal to ~ 1 x 10^6 m/s in graphene[148]. The high carrier velocity renders single crystals of graphene theoretically highly electrically conductive. Current manufacturing methods produce polycrystalline graphene sheets[150,151], with grain boundaries presenting a resistance to charges in the film. Still, decent sheet resistances have been reported over large areas for few layer graphene; the best so far is a four-layer doped graphene sheet with a sheet resistance of 30 Ω/sq over a few inches[149].

Single layer graphene sheets can also transmit over 97% of light[143,149] and the bonding between the atoms give graphene excellent mechanical properties including strength[144] and flexibility[144,146]. These properties are ideal to create the flexible transparent electrodes sought after by organic

photovoltaics and indeed graphene also has shown good enough energy level alignment with organic materials to facilitate charge extraction and maintain a high open circuit voltage[156,294]. The transparency and flexibility are superior to the current industry-standard metal oxide transparent conductors[146,295]; the only thing preventing implementation is the production of large areas[296]. In addition to technical benefits, the abundance of carbon means that graphene would not face the issues with material supply and price fluctuations experienced by the widely-used transparent electrode indium tin oxide (ITO)[121].

In this chapter graphene is used as an anode instead of ITO in vacuum-deposited squaraine:C_{70} (SQ:C_{70}) heterojunction photovoltaic devices. Vacuum deposition is a potentially low-cost, high volume solar cell fabrication technique and already has use in industry[297,298]. Squaraines are small molecule electron donors that strongly absorb in the red to infrared part of the spectrum, allowing even a thin layer to be an effective solar cell component, with cell efficiencies of 4.1%[299]³⁰⁰³⁰⁰ in bilayers with acceptor materials. Fullerenes are common electron acceptors, the most widely used being C_{60} in organic solar cells. However, C_{70} has been shown to absorb more widely across the solar spectrum and has resulted in devices of higher J_{sc} than C_{60} equivalents[301,302].

Squaraine-C_{60} has been a popular bilayer combination [161,299,300]. Recently this combination has been adapted to make use of the favourable properties of C_{70}, with squaraine-C_{70} having been made into co-deposited bulk heterojunction[159] and vacuum-deposited planar forms[299]. To further optimise devices, the use of an electron blocking layer of MoO_3 is examined in this chapter. This has been shown to vacuum-deposit onto graphene with good wettability[150] and suitably aligned in energy to act as an electron blocking and hole transporting layer in this system.

I firstly compare the efficiency parameters of identical SQ-C_{70} bilayer devices with different anodes: ITO or graphene. Then the focus is shifted to the optoelectronic mechanisms of devices with the graphene-MoO_3 electrode system.

6.2 Devices

The physical and electronic structures of the solar cells are shown in figure 6-1. Squaraine (SQ) and C_{70} form the active heterojunction. The chemical structure of these molecules is shown in figure 6-1A. Molybdenum tri-oxide (MoO_3) and bathocuproine (BCP) act as electron-blocking and hole-blocking layers respectively (figure 6-1B). The ITO is bought pre-deposited on a glass substrate etched so a thin strip of width 2.0 mm remains. The graphene electrodes were prepared by Mr Zhengyu He using a method similar to that explained by Suk et al.[303]. Specifically, chemical vapour deposition (CVD) was used to deposit graphene on a copper substrate. This was coated with a layer of PMMA before the copper substrate was etched away by ferric chloride solution. The PMMA + graphene was then transferred onto a transparent quartz plate before acetone was used to remove the PMMA. The resultant graphene area was 3.2 mm x 2.2 mm. The layers of the solar cell were sequentially vacuum-deposited onto the ITO or graphene by Dr Peter Kovacik. The aluminium electrodes were deposited in three strips, resulting in solar cell 'pixels' (figure 6-1C) with device areas of 2.1 mm^2 and 4.5 mm^2 respectively.

Devices were tested in a nitrogen atmosphere as soon as possible after manufacture and stored in a nitrogen atmosphere dry-box when not being tested.

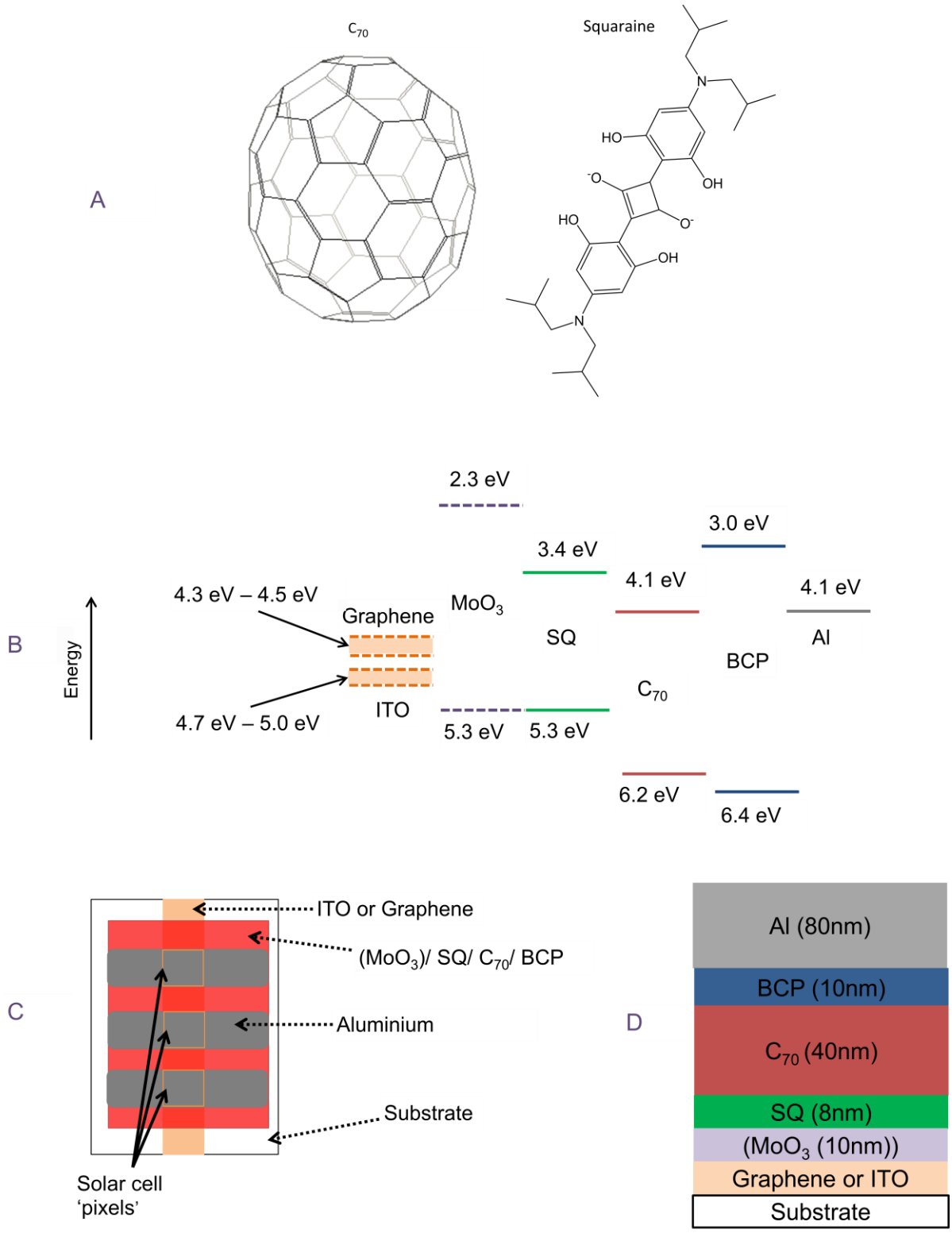

Figure 6-1: A: Molecular structure of C_{70} and squaraine. B Energy level structure of solar cell components in isolation. Energy values are taken from the literature[146,160,162,304,305] and are referenced to the vacuum energy level. Dashed lines indicate energy levels of materials which change between devices. C: Schematic plan view of device structure D: Schematic side view of device structure

6.3 Optical and electronic properties of the electrodes

Sheet resistances and thicknesses of the electrodes used in this chapter are presented in table 6-1. Transmittance is shown in figure 6-2. The data for the graphene were measured by Mr Zhengyu He: the number of graphene layers was identified by Raman spectroscopy and the sheet resistance by the Van de Pauw method.. The thickness of the ITO was measured by a DEKTAK profilometer and the sheet resistance for the ITO was obtained from the supplier.

Anode	Thickness	Sheet resistance (Ω/square)
Graphene	Monolayer/ bilayer (order of 1 nm)[306]	500
ITO	60 nm	15

Table 6-1: Thicknesses and sheet resistances of the electrodes.

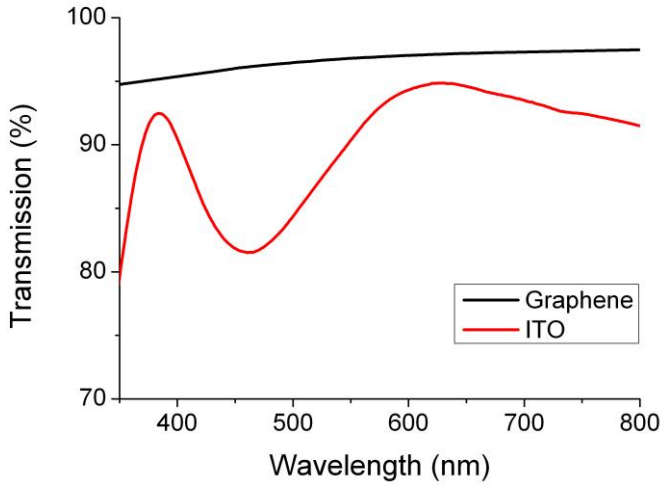

Figure 6-2: Tranmission spectra of the graphene (black) and ITO (red) electrodes. These were calculated from absorbance spectra of the electrodes. To obtain absorbance through just the electrodes, absorbance of the substrates were subtracted from the total electrode+susbtrate absorbance.

The sheet resistance of graphene is much worse than that of ITO indicating the presence of grain boundaries in the graphene film. The very lowest reported graphene sheet resistances

(~30 Ω/square) are obtained by creating multilayer graphene[149], so it is unsurprising to have a relatively high value for the mono- and bilayer graphene here. However, the optical transmission through the graphene is, as expected[149,307], much higher than the ITO. Also the comparatively thick ITO film induces interference, visible as the waves in its transmission spectrum[308,309]. It should also be noted that the quartz substrate on which the graphene is deposited is substantially more transmissive than the glass substrate on which the ITO rests, with 96 % transmission through quartz compared to 79 % through glass in the visible region. This will further enhance the transmission difference set up by the electrodes, as discussed in section 6.4.1.2.

6.4 Device Results

6.4.1 Graphene vs. ITO

Current density-voltage (JV) curves for the two devices without the MoO_3 blocking layer are presented in figure 6-3. The device with the graphene electrode experiences a greater efficiency than the device with the ITO electrode, with the higher J_{sc} and V_{OC} contributing to this. The one disadvantage of graphene is the drop in fill factor. As ITO and graphene devices are produced simultaneously under the same conditions, it is assumed that the differences observed stem from the different transparent contacts rather than differences in device processing.

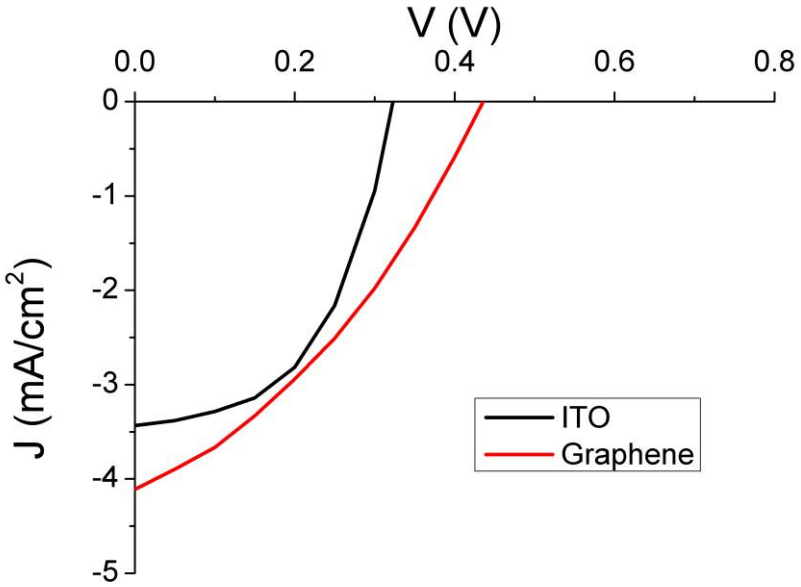

Anode	J_{sc} (mA/cm^2)	V_{OC} (V)	FF (%)	PCE (%)	R_s (kΩ.cm^2)	R_{sh} (kΩ.cm^2)
ITO	3.42 ± 0.04	0.32 ± 0.01	51 ± 2	0.56 ± 0.02	0.024 ± 0.003	1.16 ± 0.20
Graphene	4.11 ± 0.02	0.44 ± 0.01	35 ± 2	0.63 ± 0.02	0.060 ± 0.002	0.25 ± 0.02

Figure 6-3: Current density – voltage (JV) curves for devices with ITO and graphene electrodes. JV parameters extracted from the curves are given in the table: short circuit current (J_{sc}), open circuit voltage (V_{OC}), fill factor (FF) and power conversion efficiency (PCE). Series resistance (R_s) and shunt resistance (R_{sh}) values extracted from the curve are also shown. Errors represent the standard deviation of values across the three pixels on each substrate.

6.4.1.1 Fill factor decrease

The fill factor of the graphene-based device is lower than that of the ITO due to parasitic resistances. The high series resistance is expected from the much higher sheet resistance of the graphene[295], i.e. once charges reach the graphene the journey across the graphene sheet to the external circuit could act as a source of series resistance. The low shunt resistance of the device with the graphene electrode implies there is more leakage current in the graphene cells. Other studies have reported that graphene electrode cells result in lower shunt resistance than those with ITO[152,294] and attribute this to the graphene surface being slightly rougher than ITO[146], perhaps induced during transferral of

graphene from PMMA to substrate[152]. A rougher surface increases the possibility of less than total coverage of the graphene by the squaraine, which would result in direct contact of the C_{70} to both electrodes, causing leakage current. Although transmission electron microscopy was performed by the manufacturer of the graphene in these devices to view the graphene surface, this does not provide quantitative information on its roughness. Atomic force microscopy could show this, but this technique could not be carried out during the course of this project.

6.4.1.2 Short circuit current improvement

Short circuit current output is reliant on the absorption of photons to generate charges and on charge carrier collection at the electrodes. With higher transmission through the graphene and its substrate, the semiconductor layers of this device will receive more photons than that of the ITO device. Electrode and substrate transmission of both devices, along with absorption of the squaraine and C_{70} layers are shown in figure 6-4.

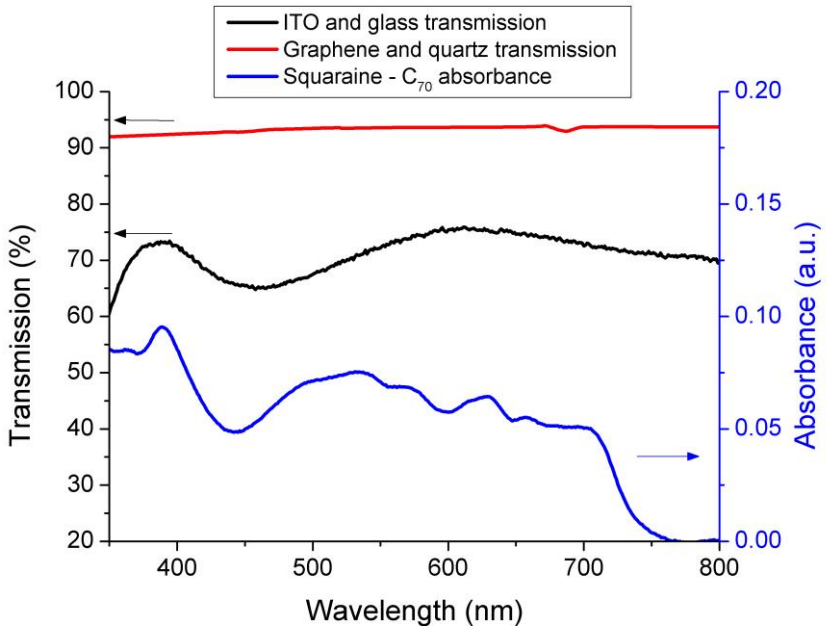

Figure 6-4: Transmission spectra of ITO on glass (black) and graphene on quartz (red) and the absorbance spectrum of the squaraine (8nm) – C_{70} (40 nm) heterojunction.

In the regions of high semiconductor absorption, the ITO device transmits 70 – 75 % of light, whereas this figure is about 92 % for the graphene device. The ITO device produces 83 % of the short circuit current of the graphene device. This is a not as low as would be expected given the electrode transmission. What is probably aiding ITO current extraction is the much lower series resistance compared to the graphene device. If the sheet resistance of the graphene can be improved (for example by doping the film[149]) without losing this high transmittance, then graphene devices could reach even higher short circuit currents.

6.4.1.3 Open circuit voltage improvement

Work functions

The maximum V_{OC} in an organic solar cell is the offset between the HOMO level of the donor and LUMO level of the acceptor[310]. This maximum can only be achieved if the electrodes make Ohmic contact with the active layers, in which case the work functions of the electrodes pin to the Fermi level of the semiconductor layer[311–314]. However, non-Ohmic contacts should form in the case of ITO and graphene as their work functions are much lower than the HOMO of the donor[161] (figure 6-1), in which case the electrode work function will limit V_{oc}[311,314]. Graphene has a lower work function than ITO so should form a poorer Ohmic contact to squaraine than the ITO, thus actually lowering the theoretical maximum V_{OC} of the device. Since the V_{OC} is actually higher in the case of the graphene electrode, the dark current is now examined to understand the origin of the difference in V_{OC}.

Dark current

The open circuit voltage is the point at which dark current balances photocurrent, so a lower dark current will result in this balance point being shifted to a higher voltage, i.e. V_{OC} will increase. Dark current density - voltage (JV) curves are shown in figure 6-5 for devices with the graphene and ITO electrodes. At forward bias, the device with the graphene electrode clearly has a lower dark current, which explains why the V_{OC} for this device is higher than that of the ITO, despite the lower work function. To understand the cause of this, the dark JV curves will be examined in relation to the three distinct sections of dark JV curves[275]:

- Negative bias and low forward bias: shunt current dominates, which has a linear J-V relationship
- Medium forward bias: diffusion current dominates, which has an exponential J-V relationship
- High forward bias: series resistance suppresses current flow

The first thing to note is that the device with the graphene electrode has an almost symmetrical JV curve about V = 0. As shunt current dominates at negative bias, such symmetry indicates a very dominant shunt current, even at forward bias[24]. A slight change in curve shape suggests that there is a small region where diffusion current prevails (labelled J_{diff} on the graph) but this is soon suppressed by series resistance (R_s) effects. It is thus meaningless to extract dark current parameters (namely reverse saturation current and ideality factor) to aid analysis as it is difficult to disentangle the J_{diff} section from those sections of the curve limited by parasitic resistance.

In comparison, the forward bias current of the ITO device quickly rises above reverse bias current values, showing a clear diffusion current dominating region (J_{diff} section) before series resistance again suppresses it (R_s section).

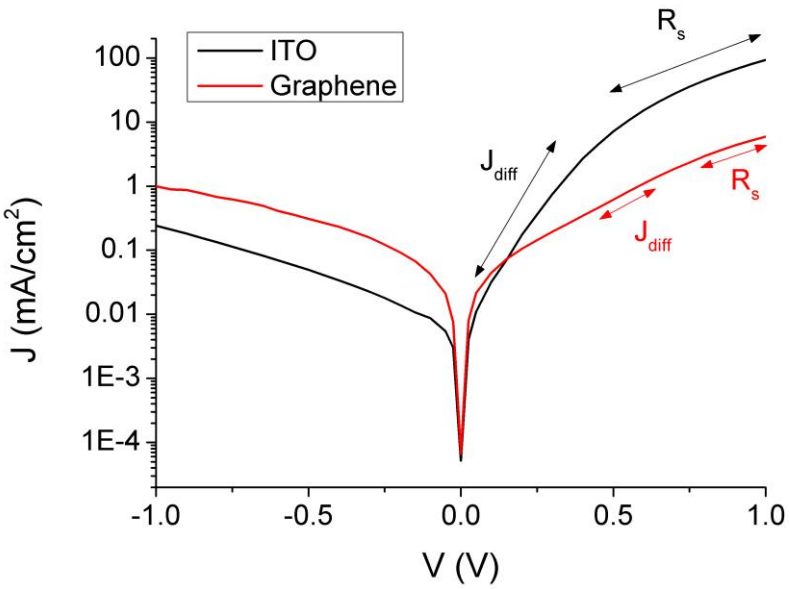

Figure 6-5: Semi-logarithmic plot of dark current density-voltage curves for devices with ITO (black) or graphene (red) anodes.

The comparatively weak diffusion current through the graphene device could be linked to its much higher series resistance (figure 6-3), which will severely limit dark current flow[315]. Wu et al.[294] also observed that after a small forward bias the dark current of an organic solar cell with a graphene electrode was lower than that of an ITO equivalent. Wu et al. calculated that the lower dark current was almost entirely due to the higher series resistance, stemming from the high sheet resistance of graphene. Thus the reasoning seems to be the same in the case of the squaraine-C_{70} devices here. Despite the high series resistance hindering photocurrent, its role in lowering dark current is beneficial to the $V_{OC.}$

Having explained the efficiency difference between devices with graphene and ITO electrodes, a study of the graphene device with a 10 nm MoO_3 layer under the squaraine will now be considered. MoO_3 has proven to be an effective electron hole blocking layer and hole transport layer[112,150,162] and has energy levels[162] suited to between the graphene – squaraine interface, with a lower work function than graphene (figure 6-1B). Such changes may be expected to improve device efficiency.

6.4.2 The effect of MoO_3

JV curves and associated parameters for devices with and without the MoO_3 blocking layer are presented in figure 6-6. The PCE is much higher with the MoO_3 layer as a result of the substantial increase in V_{OC}, yet detrimentally, J_{sc} diminishes.

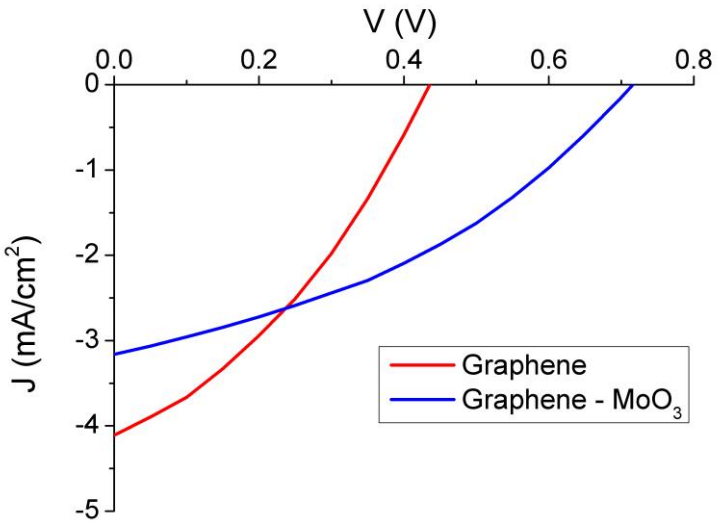

Anode	J_{sc} (mA/cm^2)	V_{OC} (V)	FF (%)	PCE (%)	R_s (kΩ.cm^2)	R_{sh} (kΩ.cm^2)
Graphene	4.11 ± 0.04	0.44 ± 0.01	35 ± 2	0.63 ± 0.03	0.060 ± 0.002	0.25 ± 0.02
Graphene–MoO_3	3.16 ± 0.05	0.72 ± 0.01	37 ± 2	0.84 ± 0.01	0.108 ± 0.003	0.53 ± 0.01

Figure 6-6: JV curves for squaraine-C_{70} devices with a graphene anode (red) or a graphene + 10 nm MoO_3 anode (blue). JV parameters extracted from the curves are given in the table: short circuit current (J_{sc}), open circuit voltage (V_{OC}), fill factor (FF) and power conversion efficiency (PCE). Series resistance (R_s) and shunt resistance (R_{sh}) values extracted from the curve are also shown. Errors are the standard deviation of values across the three pixels on each substrate.

Short circuit current reduction

The reduction in J_{sc} could be caused by the higher series resistance in the device with the MoO_3 layer. MoO_3 is insulating[316] and too thick a layer has been known to reduce device performance because of the increased series resistance[150,317]. Cattin et al.[317] reported an optimum thickness of 3.5 nm of MoO_3 on ITO. In this case a thickness of 10nm of MoO_3 was used, so a thinner layer could be possibly be used improve the short circuit current. This thickness would have to be optimised for the graphene surface as it is important to have a thickness that sufficiently covers the entire electrode area.

In addition, a 10 nm MoO_3 layer has been shown to reduce the overall transmission of photons into the active layer by about 4 %[318]. This is not such a big reduction as the one between graphene and ITO, yet it will reduce the number of charges generated in the active layer.

Open circuit voltage increase

MoO_3 has a higher work function than graphene so is thought more likely to form an Ohmic contact with the squaraine donor[162,299], resulting in Fermi level pinning and thus independence of the V_{OC} from the anode work function. An alternative depiction of band alignment with MoO_3 is that it creates a metal-insulator-semiconductor junction between the anode and the electron donor[316,317], in which the band-tilting of the insulator effectively decreases in the barrier height between the anode and the donor[316,317,319]. With either of these mechanisms, the MoO_3 should increase the maximum possible V_{OC} of the device.

As an electron-blocker, MoO_3 is expected to reduce recombination at the anode/ squaraine interface, so should lower dark current, which is observed (figure 6-7). A lower dark current results in a higher V_{OC}. In addition, the MoO_3 decreases the chance of shunt paths forming between the

electrodes[150], resulting in better shunt resistance (figure 6-6). Complete coverage of the MoO_3 is vital for high shunt resistance and Park et al.[150] have shown that MoO_3 has good wetting with graphene, so it seems like an appropriate choice of blocking material. The high shunt resistance will also lead to a lower dark current at low forward bias[275].

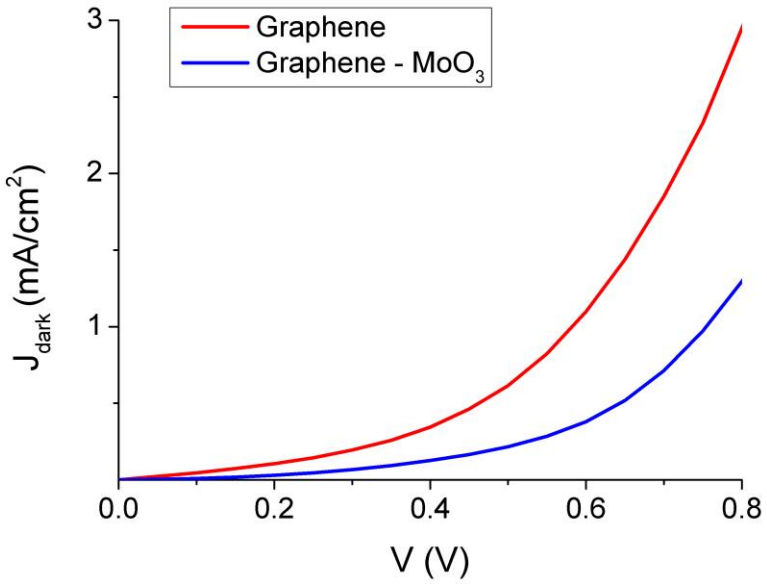

Figure 6-7: Dark current density – voltage curves of devices with graphene electrodes both without (red) and with (blue) and 10 nm MoO_3 electron blocking layer.

6.4.3 Further study of graphene – MoO_3 device

Looking to the specifics of the current generation dynamics in the device, the external quantum efficiency is examined in relation to the absorbance of the two photon-absorbing materials and energy level alignment of the layers.

Absorption and external quantum efficiency

The absorbance spectrum of the squaraine-C_{70} bilayer is plotted in figure 6-8 along with the external quantum efficiency measurements through the device with the graphene-MoO_3 electrode. C_{70}

absorbs photons of wavelength between 300 nm and 700 nm and squaraine absorption lies between 500nm and 800 nm with a peak just below 700 nm[299]. After photon absorption, generated excitons dissociate and are either extracted as current or recombine. Those that are extracted reveal themselves in the external quantum efficiency (EQE) spectrum.

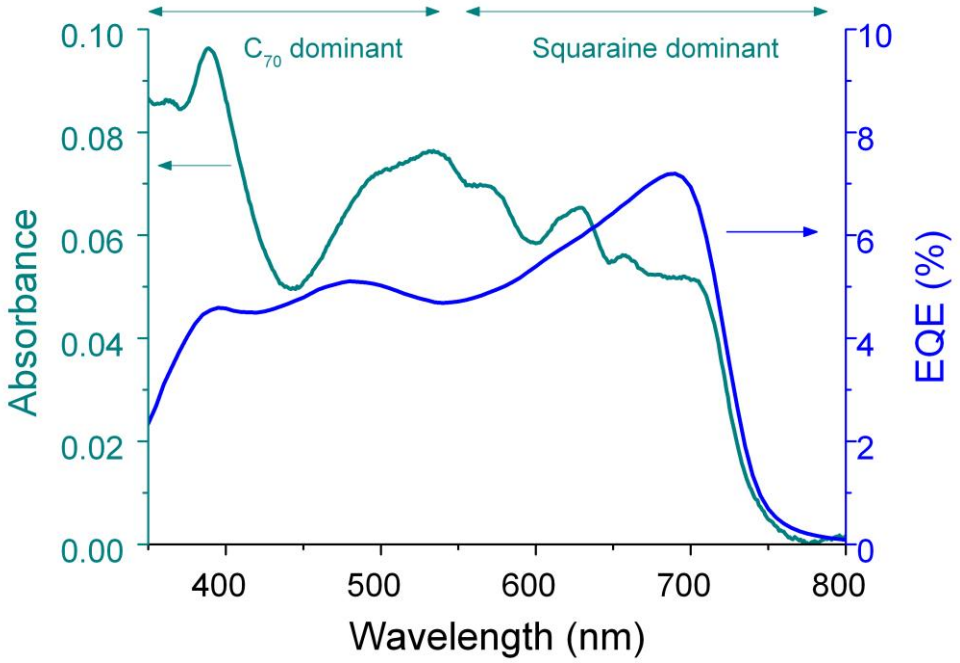

Figure 6-8: Absorbance (left axis) through SQ (8 nm)/ C_{70} (40 nm) film and External quantum efficiency (right axis) of the graphene/ MoO_3/ SQ (8nm)/ C_{70} (40 nm)/ BCP/ Al device.

The extinction coefficient for squaraine has been reported to be more than double that of C_{70}[299,320,321], so for both materials to achieve similar absorbance a thicker C_{70} layer was used. It can be seen that with the thicknesses used here, the C_{70} absorbs slightly more light at its peak than the squaraine (figure 6-8).

Looking at the EQE, the current mainly comes from the excitons generated by the squaraine (those generated from the longer wavelength photons). The 700 nm EQE peak is around where the squaraine absorption peak is expected to be. The absorption spectrum for the two semiconductors does not actually peak at 700 nm because at shorter wavelengths there are also absorption contributions from C_{70}. As excitons are not being extracted from the C_{70} layer as well as they are

from the squaraine layer, many excitons in the C_{70} must be generated more than a diffusion length away from the heterojunction interface and thus cannot reach the interface to dissociate. Diffusion lengths of non-functionalised squaraine have been reported to be no more than 4.5 nm[299,322] with values for C_{70} not being more than 15 nm[320,323]. These diffusion lengths are much shorter than the thicknesses of the layers in the devices presented here, so both layers have considerable 'dead zones' where excitons are generated without being able to contribute to current output. The dead zone in the squaraine is a little less than half of its layer thickness, whereas the dead zone in the C_{70} layer is more than half of its thickness. So it would be expected that proportionally more excitons in the C_{70} recombine before reaching the heterojunction.

The spectral shape of the C_{70} absorption compared to its EQE spectrum is curious. C_{70} has good absorption of short wavelength photons (450 nm and less) but excitons generated by these short wavelength photons are poorly extracted. Short wavelengths have a short penetration depth[258] so once passing through the front, relatively transparent layers, these short wavelength photons should be absorbed close to the front of the C_{70} layer, i.e. close to the squaraine/C_{70} interface. Thus excitons here would be expected to be more easily dissociated and extracted than those from longer wavelength photons generated at the back of the C_{70} layer, yet the reverse is observed. This paradox was seen in other studies[159,299,324] but was never explained. A likely explanation was that given by Peumans et al.[325] for a copper phthalocyanine (CuPc) (20 nm)/ C_{70} (40 nm) bilayer device, in which reflection from the back aluminium cathode was calculated to significantly increase absorption of long wavelength photons. Those photons with a longer penetration depth that reach the aluminium have more chance of being reflected than the shorter wavelength photons[258] and thus absorption in the long wavelength region might be underestimated by the absorption spectrum of figure 6-8, which was taken without the aluminium cathode.

In order to improve the current extraction, a change in device structure seems necessary. At present, there are some excitons that are generated too far away from the heterojunction interface to dissociate. However the layers must be this thickness to absorb a good proportion of photons. Extending the interfaces throughout the absorber layers with a bulk heterojunction structure (the structure used in chapter 5) is one way to create extra exciton dissociation sites. EQE has been shown to increase when a bulk heterojunction SQ:C_{70} structure is used rather than a planar heterojunction[159]. However, bulk heterojunctions can be disordered and it takes fine tuning in the manufacturing process to ensure that both materials form interpenetrated networks between the electrodes. If these networks are not continuous then separated electrons and holes will have difficulty in reaching the electrodes and charge extraction will be hampered. A more ordered design than this would be to have one phase form vertical nanopillars through the device. A few years ago squaraine nanowires were grown[326]. These were solution-processed so could not be incorporated simply into the cell design here, however the fact that such ordered structures can be made is promising for the future efficiency gains in these types of devices.

Additional further work could be done to study the effect of the aluminium cathode on reflection of incident photons in this particular cell structure. If the cell thickness can be tailored to encourage constructive interference of incoming and reflected light then absorption could be significantly enhanced[325].

Comparing the absorption spectrum with EQE has helped in the understanding of how structure of the absorber layers can be more closely tuned to the exciton diffusion lengths. This will enable excitons to always be created where they can reach the heterojunction to dissociate. After dissociation, electrons and holes drift to the electrodes via the blocking layers. Bias-dependent external quantum efficiency reveals how the energy alignment of these layers aids this process.

Bias-dependent external quantum efficiency

Bias-dependent external quantum efficiency is presented in figure 6-9. As forward bias increases, a forward current starts to flow in the opposite direction to the photocurrent (as JV curves show). Thus the current recorded by the ammeter is a combination of photocurrent output plus forward current. This forward current is identified by the constant current that appears at wavelengths longer than the squaraine band gap, i.e. at 800 nm and longer. For presentation of the EQE spectra here the forward current is subtracted as a baseline from the total current before the EQE is calculated. As the spectra have been shifted, the spectra are more correctly termed 'apparent quantum efficiency' (AQE) curves. On this graph, positive current indicates photocurrent and negative current indicates forward diode current.

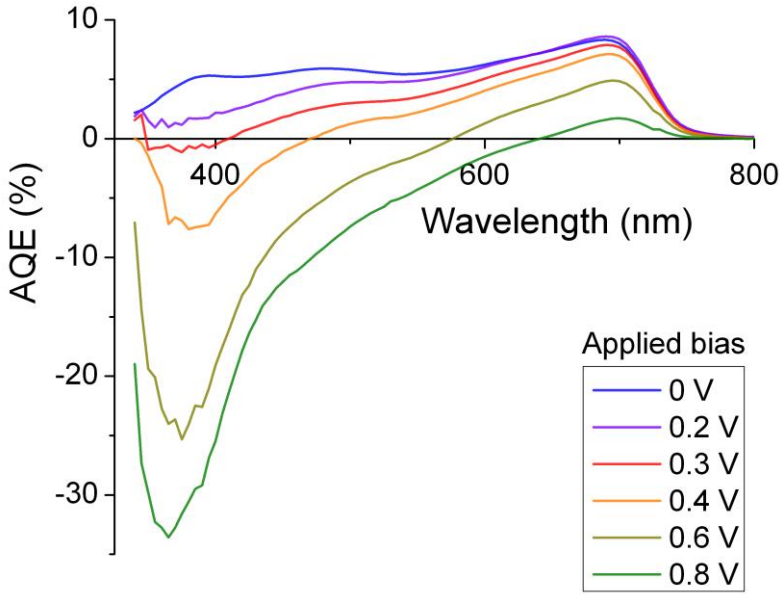

Figure 6-9: Bias dependent external quantum efficiency, presented as apparent quantum efficiency (AQE), of the graphene/MoO_3/SQ/C_{70}/BCP/Al device.

As forward bias increases, AQE decreases across the spectrum. This is a common observation[327,328] and akin to voltage-dependent photocurrent collection as seen in section 5.5.2.1 (chapter 5). It

results from the reduction in the electric field making it harder for charges of low mobility to reach the electrodes[227,228,327].

Interestingly, current generated from the shortest wavelength photons seem to invert under forward bias, so charges are extracted as forward current rather than reverse (photo) current. Up to 500 nm, nearly all current can be assumed to originate from the C_{70} layer[299]. Studying previous work on the AQE of C_{60}/ donor material heterojunctions, it is revealed that the AQE of C_{60} regularly reduces more rapidly with bias than the donor material in the same solar cell[273,327,329]. One explanation of the negative AQE[273,329] is based on experiments and theoretical work by Kazaoui et al.[330], which showed that high-energy C_{60} and C_{70} excitons are probably weakly-bound excitons. These, almost free charges, increase the conductivity of the fullerene under illumination[273]. Such an increase in conductivity will enable more forward 'dark' current to flow.

Another factor to consider is that negative EQE has also been associated with charges overcoming a barrier[331]. Indeed this would make sense considering the energy level diagram in figure 6-1B. The energy level gap between BCP and the C_{70} HOMO level is only 0.2 eV. Thus it is feasible that under small forward bias, the BCP is no longer an effective hole blocking layer and so holes generated in the C_{70} can move the 'wrong way' and generate a forward current. The MoO_3 – squaraine energy gap is much higher and the AQE curves show that the MoO_3 layer is an effective electron blocker even under forward bias.

What is unusual about the AQE results presented here is that the negative AQE from C_{70} is much more intense at shorter wavelengths. It is expected that these shorter wavelength photons are absorbed closer to the squaraine interface than the 500 nm photons, so should be more likely to dissociate into free charge carriers. If this reason were sound, then C_{70} conductivity would be larger when shorter wavelength photons were absorbed. However, going against this argument is the EQE spectrum at 0V, which shows that charge extraction is occurring almost equally for all wavelengths absorbed in the C_{70}. Also, the increase in conductivity would arise when an exciton generated on the

squaraine dissociated at the junction and C_{70} accepted the electron, yet the negative AQE is not observed when squaraine is optically excited. An alternative reason for the very negative AQE from excitons generated at short wavelengths could be that their binding energy is lower than those at other wavelengths. This would need to be examined theoretically, but according to Kazaoui et al.[330] not all transitions produce excitons with the same binding energy. An exciton of lower binding energy would increase conductivity, and thus dark current, more than those that are more tightly bound. A higher conductivity would also augment the effects of any decreased C_{70} - BCP barrier on forward current.

6.5 Conclusions

Graphene electrodes have been employed with squaraine – C_{70} solar cells, showing significant PCE improvement upon ITO equivalents. This is largely a result of its greater transparency, which dominates in the face of the greater series resistance of graphene devices. Despite theoretically high conductivity, graphene suffers from poor sheet resistance, likely to be due to grain boundaries within graphene sheets[151]. The greater series resistance along with a low shunt resistance results in a much poorer fill factor, which would decrease efficiency if the higher J_{sc} and V_{OC} did not counteract it. A possible reason for the low shunt resistance could be a rough graphene surface[152], but this needs further investigation. The high series resistance, however, decreases the dark current of the devices to such an extent that V_{OC} is higher in the graphene devices.

A more conventional way to increase V_{OC} is to modify the band-alignment between electrodes and semiconductors. This was attempted by adding MoO_3 to the graphene device and indeed a V_{OC} improvement was observed with 0.72 V achieved. Furthermore, the MoO_3 increased the shunt resistance, which contributes to lower dark current and higher V_{OC}.

MoO_3 is also an electron blocking layer but despite this, MoO_3 caused a reduction in J_{sc}, which was a product of higher series resistance through the cell and lower optical transmission through the graphene – MoO_3 layer.

External quantum efficiency was then studied to investigate current output in more detail. It was revealed that excitons generated in the squaraine result in proportionally more current than those generated in the C_{70}. This indicates that many excitons generated in the C_{70} are unable to diffuse to the heterojunction to dissociate. Furthermore, bias dependent external quantum efficiency showed that at low forward bias, excitons generated in C_{70} are extracted as forward current. One hypothesis for why this occurs is that C_{70} could be photoconductive[273,329], i.e. the photogenerated charges will increase the C_{70} photoconductivity. Therefore, as a forward bias is applied, which injects charges in to the C_{70}, a greater forward current can manifest itself than would flow if the C_{70} were not illuminated. A negative quantum efficiency peak will occur if the increase in forward current exceeds any photocurrent generated. Another possible reason for the negative quantum efficiency is that the BCP layer might be less hole-blocking at forward biases. The small energy level offset with C_{70} suggests this is likely to happen. In this case, photogenerated holes in the C_{70} could drift to the aluminium electrode, creating a forward current rather than a reverse (photo) current.

With these points in mind, the following future investigations and improvements are suggested:

- Identify the roughness of graphene, for example by using atomic force microscopy. From there, establish whether any steps in processing can be improved to ensure as flat a graphene sheet as possible.
- Investigate the morphology of vacuum-deposited MoO_3 on graphene to ensure good coverage of MoO_3. Good coverage ensures a high shunt resistance.
- Investigate the morphology of squaraine onto the MoO_3 to identify the optimum thickness of squaraine that covers electrode and is close to its exciton diffusion length.

- Change the morphology of the absorber layer. As it stands, many charges are generated too far from the heterojunction and not utilised. The extra thickness just means it is further for dissociated electrons to travel, which increases the chances of recombination. Increasing the interfacial area between the squaraine and the C_{70}, for example by means of a bulk heterojunction, could improve charge extraction.
- Change BCP to another blocking layer with deeper HOMO (or lower the HOMO of BCP) to more effectively block forward current.

7. Final conclusions and outlook

7.1 Thesis conclusions

This thesis studied three new solar cell designs which aimed to improve device efficiency. All utilised the benefits of low-dimensional systems. Quantum dots were utilised as photon absorbers in chapters 4 and 5, and graphene was used as a transparent electrode in chapter 6.

Chapter 4 presented a study of intermediate band solar cells (IBSCs) made from a gallium arsenide (GaAs) p-i-n structure, with indium arsenide (InAs) quantum dots providing the 'intermediate band' energy states. Thin layers of wide-band gap aluminium arsenide (AlAs) were deposited on top of each layer of the quantum dots, in an attempt to raise the open circuit voltage (V_{OC}) by preventing Fermi level pinning of the intermediate band (IB) to the quasi-electron Fermi level of the GaAs conduction band (CB). The addition of the AlAs layer was indeed seen to increase the V_{OC} from 0.66 V to 0.80 V, but J_{sc} concurrently diminished. Electroreflectance and external quantum efficiency determined that the cause of the J_{sc} reduction was a reduction in the number of InGaAs states, suggesting that the AlAs had suppressed the intermixing of gallium and indium at the edges of the quantum dots [81,83]. The higher V_{OC} arose from reduced recombination in the AlAs cell and not, as postulated, isolation of the intermediate band. Instead, it was found that charges from the QD can tunnel into the conduction band, indicating that wide-band gap AlAs and the lack of InGaAs states are not significant barriers to charge movement. The lower recombination in the AlAs cell was studied using JV parameters, which pointed to a lower defect density than for the control cell, although a morphological study is required to investigate this further.

Chapter 5 detailed studies of inorganic bulk heterojunctions (BHJ) made from lead sulphide colloidal quantum dots (PbS CQDs) blended with zinc oxide (ZnO) nanoparticles. The aim of the structure was to create a solar cell with greater interface area than that possible with a planar heterojunction, and

thus open up more possibilities for charge separation and extraction. However, a corresponding increase in short circuit current did not materialise and in fact decreases when the ZnO fraction exceeded 30 wt%. It was evaluated that there is likely to be a fine balance in the BHJ between electron-hole pairs separating and electron-hole pairs recombining before separation: photoluminescence results indicated reduced electron-hole pair separation in bulk heterojunction solar cells; however, external quantum efficiency spectra suggested that exciton dissociation *can* occur at bulk heterojunction interfaces. Still, the main limitation to this technology was poor charge transport in the bulk heterojunction, arising from the reduction in pathways to the electrodes. This was particularly the case for the PbS phase, with an increasing fraction of ZnO increasing the series resistance. In terms of overall efficiency, a small improvement was observed for a blend composition of 70 wt% PbS: 30 wt% ZnO. This was attributed to an increased open circuit voltage, largely due to a reduction in dark current as a result of fewer shunt pathways.

Chapter 6 examined the use of graphene as the transparent conducting electrode for squaraine/ C_{70} vacuum-deposited bilayer solar cells. Cells with graphene electrodes showed significant PCE improvement upon ITO equivalents. This was primarily because the graphene was more transparent than ITO. This counteracted the reduction in current output caused by increased series resistance in the graphene devices, linked to the much higher sheet resistance of the graphene. A high sheet resistance is attributed to grain boundaries between different crystals within the graphene sheets[151]. Graphene devices also had a lower shunt resistance than those made with ITO, giving these devices a lower fill factor. However, the high series resistance decreases the dark current of the devices to such an extent that V_{OC} is higher in the graphene devices. A better way to increase V_{OC} was found to be by adding a layer of MoO_3 between the graphene electrode and the squaraine, which modified the band-alignment between them sufficiently to cause a V_{OC} improvement from 0.44 V to 0.72 V. Furthermore, the MoO_3 increased the shunt resistance, which contributed to lower dark current and higher V_{OC}. One disadvantage to the MoO_3 was that the higher series resistance and lower optical transmission caused by its presence reduced J_{sc}. Further studies of the graphene-MoO_3 device

revealed that many excitons generated in the C_{70} are generated too far away from the squaraine/C_{70} heterojunction to dissociate. Furthermore, bias dependent external quantum efficiency showed that at low forward bias, excitons generated in C_{70} are extracted as forward current. This is either due to photogenerated charges causing C_{70} to increase in conductivity[273,329], thus allowing more forward current to flow than in the dark, or it is because the small energy offset between the BCP hole-blocking layer and the C_{70} highest-occupied molecular orbital allows photogenerated holes in the C_{70} to drift to the aluminium electrode, creating a forward current.

7.2 Suggestions for future investigations

From this work, future design considerations and study points are put forward.

Chapter 4

- To help offset the J_{sc} reduction due to the lack of InGaAs states, the QD absorption should be increased. This absorption can be enhanced by increasing dot density or by delta-doping the QDs so there is already an electron population within them[51,229].
- To prevent tunnelling to the conduction band in the InAs/GaAs system, spacer materials could be used either side of the quantum dot region as, if they are thick enough or wide enough, tunnelling will be reduced[79,230].

Chapter 5

- Choosing a heterojunction with a larger conduction band offset could increase exciton dissociation at bulk heterojunction interfaces[92]. This could be achieved by fabricating smaller PbS quantum dots with larger band gaps.
- To fully understand the driving forces on photogenerated electron-hole pairs, it should be determined exactly whether a p-n, p-i-n or excitonic junction forms in the BHJ device. A way

to start this study could be do perform impedance spectroscopy to measure the depletion width[112] (if there is one).

- A step towards improving charge transport would be to perform a morphological study on the bulk heterojunction, to identify how percolation pathways can be improved to reduce series resistance, and whether PbS/ZnO interfaces form within the exciton diffusion length (or depletion width for the p-n case).
- Thicker PbS and ZnO blocking layers could be used to increase shunt resistance[238].
- To increase photon absorption, an acceptor material could be chosen that absorbs light in the visible part of the electromagnetic spectrum[93].

Chapter 6

- An investigation of the morphology of different thicknesses of vacuum-deposited MoO_3 on graphene to determine the minimum thickness at which good coverage of MoO_3 on the graphene is achieved will allow the minimisation of the series resistance due to the MoO_3 Good coverage will prevent leakage currents. Similarly, the optimum thickness of squaraine on the MoO_3 should be investigated, such that it both covers the electrode and is close to the exciton diffusion length of squaraine.
- If the morphology of the absorber layer is optimised, more excitons could be generated close to a heterojunction interface, to improve the probability of charge separation. This could be realised by means of a bulk heterojunction.
- Changing BCP to another blocking layer with deeper HOMO (or lower the HOMO of BCP) would more effectively block forward current.

8. References

1. Boyle, G., Everett, B. & Ramage, J. *Energy Systems and Sustainability*. 24 (Oxford University Press, 2003).

2. *International Energy Statistics*. *U.S. Energy Inf. Adm.* (2010). at <http://www.eia.gov/cfapps/ipdbproject/IEDIndex3.cfm?tid=2&pid=2&aid=2>

3. *International Energy Outlook 2013*. Electricity generation by source (2013). at <http://www.eia.gov/forecasts/ieo/electricity.cfm>

4. B.P. *Statistical Review of World Energy 2013*. (2013). at <bp.com/statisticalreview>

5. I.P.C.C. *Climate Change 2007 : An Assessment of the Intergovernmental Panel on Climate Change*. 14–16 (2007). at <http://www.ipcc.ch/pdf/assessment-report/ar4/syr/ar4_syr.pdf>

6. Lewis, N. S. Powering the Planet. *MRS Bull.* **32,** (2007).

7. Green, M. A., Emery, K., Hishikawa, Y., Warta, W. & Dunlop, E. D. Solar cell efficiency tables (version 42). *Prog. Photovoltaics Res. Appl.* **21,** 827–837 (2013).

8. Wadia, C., Alivisatos, a P. & Kammen, D. M. Materials availability expands the opportunity for large-scale photovoltaics deployment. *Environ. Sci. Technol.* **43,** 2072–7 (2009).

9. Sargent, E. H. Colloidal quantum dot solar cells. *Nat. Photonics* **6,** 133–135 (2012).

10. Wohrle, D. & Meissner, D. Organic Solar Cells. *Adv. Mater.* **3,** 129–138 (1991).

11. Hook, J. R. & Hall, H. E. in *Solid State Phys.* 399–414 (John Wiley & Sons, Inc., 2003).

12. Gao, J. *et al.* Quantum Dot Size Dependent J-V Characteristics in Heterojunction. *Nano Lett.* **11,** 1002–1008 (2011).

13. Schep, K. M., Kelly, P. J. & Bauer, G. E. W. Ballistic transport and electronic structure. *Phys. Rev. B* **57,** 8907–8926 (1998).

14. Nelson, J. in *Phys. Sol. Cells* 87–98 (Imperial College Press, 2003).

15. Nelson, J. in *Phys. Sol. Cells* 119–144 (Imperial College Press, 2003).

16. Sah, C.-T., Noyce, R. N. & Shockley, W. Carrier Generation and Recombination in P-N Junctions and P-N Junction Characteristics. *Proc. IRE* 1228–1243 (1957).

17. Bergmann, R. B. Crystalline Si thin-film solar cells: a review. *Appl. Phys. A Mater. Sci. Process.* **69,** 187–194 (1999).

18. Bulović, V., Baldo, M. A. & Forrest, S. R. in *Org. Electron. Mater.* 398–399 (Springer-Verlag, 2001).

19. Nelson, J. in *Phys. Sol. Cells* 46–55 (Imperial College Press, 2003).

20. Anderson, W. A. An 8% efficient layered Schottky-barrier solar cell. *J. Appl. Phys.* **45,** 3913 (1974).

21. Yeh, Y. C. M. & Stirn, R. J. A Schottky-barrier solar cell on sliced polycrystalline GaAs. *Appl. Phys. Lett.* **33,** 401 (1978).

22. Ruppel, W. & Wurfel, P. Upper limit for the conversion of solar energy. *IEEE Trans. Electron Devices* **27,** 877–882 (1980).

23. Nelson, J. in *Phys. Sol. Cells* 7–15 (Imperial College Press, 2003).

24. Dongaonkar, S. *et al.* Universality of non-Ohmic shunt leakage in thin-film solar cells. *J. Appl. Phys.* **108,** 124509 (2010).

25. Buhro, W. E. & Colvin, V. L. Semiconductor Nanocrystals Shape matters. *Nat. Mater.* **2,** 138–139 (2003).

26. Bransden, B. H. & Joachain, C. J. *Introduction to quantum mechanics*. 27–28 (Longman, 1997).

27. Hook, J. R. & Hall, H. E. in *Solid State Phys.* 124–129 (John Wiley & Sons, Inc., 2003).

28. Mandl, F. in *Quantum Mech.* 21–31 (John Wiley & Sons, Inc., 2006).

29. Grätzel, M. Conversion of sunlight to electric power by nanocrystalline dye-sensitized solar cells. *J. Photochem. Photobiol. A Chem.* **164,** 3–14 (2004).

30. Brabec, C. J. Organic photovoltaics: technology and market. *Sol. Energy Mater. Sol. Cells* **83,** 273–292 (2004).

31. NREL. *Best Research-Cell Efficiencies*. (2013). at <http://www.nrel.gov/ncpv/images/efficiency_chart.jpg>

32. Miles, R. W. Photovoltaic solar cells: Choice of materials and production methods. *Vacuum* **80,** 1090–1097 (2006).

33. Green, M. A. Thin-film solar cells: review of materials, technologies and commercial status. *J. Mater. Sci. Mater. Electron.* **18,** 15–19 (2007).

34. Aberle, A. G. Thin-film solar cells. *Thin Solid Films* **517,** 4706–4710 (2009).

35. Wesoff, E. First Solar Surprises With Big 2013 Guidance, 40 Cents per Watt Cost by 2017. *Green Tech Media* (2013). at <http://www.greentechmedia.com/articles/read/First-Solar-Surprises-With-Big-2013-Guidance-40-Cents-Per-Watt-Cost-by-201>

36. Nelson, J. in *Phys. Sol. Cells* 17–39 (Imperial College Press, 2003).

37. Shockley, W. & Queisser, H. J. Detailed Balance Limit of Efficiency of p-n Junction Solar Cells. *J. Appl. Phys.* **32,** 510 (1961).

38. Nelson, J. in *Phys. Sol. Cells* 310 (Imperial College Press, 2003).

39. Beard, M. C. *et al.* Multiple exciton generation in colloidal silicon nanocrystals. *Nano Lett.* **7,** 2506–12 (2007).

40. Ellingson, R. J. *et al.* Highly efficient multiple exciton generation in colloidal PbSe and PbS quantum dots. *Nano Lett.* **5,** 865–71 (2005).

41. Midgett, A. G. *et al.* Size and Composition Dependent Multiple Exciton Generation Efficiency in PbS, PbSe, and PbS(x)Se(1-x) Alloyed Quantum Dots. *Nano Lett.* **13,** 3078–33085 (2013).

42. Sambur, J. B., Novet, T. & Parkinson, B. A. Multiple exciton collection in a sensitized photovoltaic system. *Science (80-.).* **330,** 63–6 (2010).

43. Semonin, O. E. *et al.* Peak external photocurrent quantum efficiency exceeding 100% via MEG in a quantum dot solar cell. *Science* **334,** 1530–3 (2011).

44. Binks, D. J. Multiple exciton generation in nanocrystal quantum dots - controversy, current status and future prospects. *Phys. Chem. Chem. Phys.* **13,** 12693–704 (2011).

45. De Vos, A. Detailed balance limit of the efficiency of tandem solar cells. *J. Phys. D Appl. PhysicsPhysics* **13,** 839–46 (1980).

46. King, R. R. *et al.* 40% efficient metamorphic GaInP⁄GaInAs⁄Ge multijunction solar cells. *Appl. Phys. Lett.* **90,** 183516 (2007).

47. Geisz, J. F., Olson, J. M. & Friedman, D. J. Toward a Monolithic Lattice-Matched III-V on Silicon Tandem Solar Cell. *19th Eur. PV Sol. Energy Conf.* (2004).

48. Leite, M. S. *et al.* Towards an optimized all lattice-matched InAlAs/InGaAsP/InGaAs multijunction solar cell with efficiency >50%. *Appl. Phys. Lett.* **102,** 033901 (2013).

49. Sista, S., Hong, Z., Chen, L.-M. & Yang, Y. Tandem polymer photovoltaic cells—current status, challenges and future outlook. *Energy Environ. Sci.* **4,** 1606 (2011).

50. Luque, A. & Martí, A. Increasing the Efficiency of Ideal Solar Cells by Photon Induced Transitions at Intermediate Levels. *Phys. Rev. Lett.* **78,** 5014–5017 (1997).

51. Martí, A. *et al.* Production of Photocurrent due to Intermediate-to-Conduction-Band Transitions: A Demonstration of a Key Operating Principle of the Intermediate-Band Solar Cell. *Phys. Rev. Lett.* **97,** 1–4 (2006).

52. Marti, A., Cuadra, L. & Luque, A. Design constraints of the quantum-dot intermediate band solar cell. *Phys. E Low-dimensional Syst. Nanostructures* **14,** 150–157 (2002).

53. Marti, A., Cuadra, L. & Luque, A. Quantum dot intermediate band solar cell. *Conf. Rec. Twenty-Eighth IEEE Photovolt. Spec. Conf. - 2000 (Cat. No.00CH37036)* 940–943 (2000). doi:10.1109/PVSC.2000.916039

54. Antolín, E. *et al.* Advances in Quantum Dot Intermediate Band Solar Cells. *IEEE* 65–70 (2010).

55. Wolf, M. Limitations and Possibilities for Improvement of Photovoltaic Solar Energy Converters: Part I: Considerations for Earth's Surface Operation. *Proc. IRE* **48,** 1246–1263 (1960).

56. Beaucarne, G., Brown, A. S., Keevers, M. J., Corkish, R. & Green, M. A. The impurity photovoltaic (IPV) effect in wide-bandgap semiconductors: an opportunity for very-high-efficiency solar cells? *Prog. Photovoltaics Res. Appl.* **10,** 345–353 (2002).

57. Luque, A., Martí, A. & Stanley, C. Understanding intermediate-band solar cells. *Nat. Photonics* **6,** 146–152 (2012).

58. Palacios, P., Wahnón, P., Pizzinato, S. & Conesa, J. C. Energetics of formation of TiGa3As4 and TiGa3P4 intermediate band materials. *J. Chem. Phys.* **124,** 14711 (2006).

59. Silvestre, S. *et al.* STUDY OF GaAs(Ti) THIN FILMS AS CANDIDATES FOR IB SOLAR CELLS MANUFACTURING. in *35th IEEE Photovolt. Spec. Conf.* 1210–1212 (2010).

60. Olea, J., del Prado, a., Pastor, D., Mártil, I. & González-Díaz, G. Sub-bandgap absorption in Ti implanted Si over the Mott limit. *J. Appl. Phys.* **109,** 113541 (2011).

61. Linares, P. G. *et al.* Extreme voltage recovery in GaAs:Ti intermediate band solar cells. *Sol. Energy Mater. Sol. Cells* **108,** 175–179 (2013).

62. Adams, J. G. J. *et al.* Recent results for single-junction and tandem quantum well solar cells. *Prog. Photovoltaics Res. Appl.* **19,** 865–877 (2011).

63. Barnham, K. W. J., Braun, B., Nelson, J. & Paxman, M. Short-circuit current in a low-dimensional and energy efficiency structure photovoltaic enhancement device. **59,** 135–137 (1991).

64. Anderson, N. G. & Wojtczuk, S. J. Open-circuit voltage characteristics of InP-based quantum well solar cells. *J. Appl. Phys.* **79,** 1973 (1996).

65. Luque, A. *et al.* Progress towards the practical implementation of the intermediate band solar cell. *Conf. Rec. Twenty-Ninth IEEE Photovolt. Spec. Conf.* 1190–1193 (2002). doi:10.1109/PVSC.2002.1190820

66. Nakata, Y., Sugiyama, Y. & Sugawara, M. in *Self-Assembled InGaAs/ GaAs Quantum Dots* (Sugawara, M.) 119–133 (Academic Press, Inc., 1999).

67. Bremner, S. P., Corkish, R. & Honsberg, C. B. Detailed Balance Efficiency Limits with Quasi-Fermi Level Variations. *IEEE Trans. Electron Devices* **46,** 1932–1939 (1999).

68. Yang, X.-G. *et al.* Intermediate-Band Solar Cells Based on InAs/GaAs Quantum Dots. *Chinese Phys. Lett.* **28,** 038401 (2011).

69. Guimard, D., Morihara, R., Bordel, D., Tanabe, K. & Wakayama, Y. Fabrication of InAs / GaAs quantum dot solar cells with enhanced photocurrent and without degradation of open circuit voltage Fabrication of InAs / GaAs quantum dot solar cells with enhanced photocurrent and without degradation of open circuit voltage. *Appl. Phys. Lett.* **203507,** 2010–2013 (2012).

70. Sugaya, T. *et al.* Highly stacked and well-aligned In[sub 0.4]Ga[sub 0.6]As quantum dot solar cells with In[sub 0.2]Ga[sub 0.8]As cap layer. *Appl. Phys. Lett.* **97,** 183104 (2010).

71. López, N. *et al.* Experimental Analysis of the Operation of Quantum Dot Intermediate Band Solar Cells. *J. Sol. Energy Eng.* **129,** 319 (2007).

72. Martí, A. *et al.* Emitter degradation in quantum dot intermediate band solar cells. *Appl. Phys. Lett.* **90,** 233510 (2007).

73. Solomon, G., Trezza, J., Marshall, A. & Harris, Jr., J. Vertically Aligned and Electronically Coupled Growth Induced InAs Islands in GaAs. *Phys. Rev. Lett.* **76,** 952–955 (1996).

74. Suzuki, R., Miyamoto, T., Sengoku, T. & Koyama, F. Reduction of spacer layer thickness of InAs quantum dots using GaNAs strain compensation layer. *Appl. Phys. Lett.* **92,** 141110 (2008).

75. Hubbard, S. M. *et al.* Effect of strain compensation on quantum dot enhanced GaAs solar cells. *Appl. Phys. Lett.* **92,** 123512 (2008).

76. Okada, Y., Oshima, R. & Takata, A. Characteristics of InAs/GaNAs strain-compensated quantum dot solar cell. *J. Appl. Phys.* **106,** 024306 (2009).

77. Laghumavarapu, R. B. *et al.* Improved device performance of InAs/GaAs quantum dot solar cells with GaP strain compensation layers. *Appl. Phys. Lett.* **91,** 243115 (2007).

78. Jolley, G., Lu, H. F., Fu, L., Tan, H. H. & Jagadish, C. Electron-hole recombination properties of In[sub 0.5]Ga[sub 0.5]As/GaAs quantum dot solar cells and the influence on the open circuit voltage. *Appl. Phys. Lett.* **97,** 123505 (2010).

79. Wei, G. & Forrest, S. R. Intermediate-Band Solar Cells Employing Quantum Dots Embedded in an Energy Fence Barrier. *Nano Lett.* **7,** 218–222 (2007).

80. Sablon, K. A. *et al.* Effects of AlGaAs energy barriers on InAs/GaAs quantum dot solar cells. *J. Appl. Phys.* **108,** 074305 (2010).

81. Arzberger, M., Käsberger, U., Böhm, G. & Abstreiter, G. Influence of a thin AlAs cap layer on optical properties of self-assembled InAs/GaAs quantum dots. *Appl. Phys. Lett.* **75,** 3968 (1999).

82. Dorogan, V. G. *et al.* Thermal peculiarity of AlAs-capped InAs quantum dots in a GaAs matrix. *J. Appl. Phys.* **104,** 104303 (2008).

83. Hu, D., McPheeters, C. C., Yu, E. T. & Schaadt, D. M. Improvement of performance of InAs quantum dot solar cell by inserting thin AlAs layers. *Nanoscale Res. Lett.* **6,** 83 (2011).

84. Eisele, H. *et al.* Change of InAs/GaAs quantum dot shape and composition during capping. *J. Appl. Phys.* **104,** 124301 (2008).

85. Kim, J. S. *et al.* Effects of high potential barrier on InAs quantum dots and wetting layer. *J. Appl. Phys.* **91,** 5055 (2002).

86. Tutu, F. K. *et al.* Improved performance of multilayer InAs/GaAs quantum-dot solar cells using a high-growth-temperature GaAs spacer layer. *J. Appl. Phys.* **111,** 046101 (2012).

87. Yu, G., Gao, J., Hummelen, J. C., Wudl, F. & Heeger, A. J. Polymer Photovoltaic Cells : Enhanced Efficiencies via a Network of Internal Heterojunctions. *Science (80-.).* **270,** 1789–1791 (1995).

88. Yuen, A. P. *et al.* Photovoltaic properties of M-phthalocyanine/fullerene organic solar cells. *Sol. Energy* **86,** 1683–1688 (2012).

89. Vanlaeke, P. *et al.* P3HT/PCBM bulk heterojunction solar cells: Relation between morphology and electro-optical characteristics. *Sol. Energy Mater. Sol. Cells* **90,** 2150–2158 (2006).

90. Watt, A. A. R. *et al.* Lead sulfide nanocrystal: conducting polymer solar cells. *J. Phys. D. Appl. Phys.* **38,** 2006–2012 (2005).

91. Oosterhout, S. D. *et al.* The effect of three-dimensional morphology on the efficiency of hybrid polymer solar cells. *Nat. Mater.* **8,** 818–24 (2009).

92. Barkhouse, D. A. R. *et al.* Depleted bulk heterojunction colloidal quantum dot photovoltaics. *Adv. Mater.* **23,** 3134–8 (2011).

93. Rath, A. K. *et al.* Solution-processed inorganic bulk nano-heterojunctions and their application to solar cells. *Nat. Photonics* **6,** 529–534 (2012).

94. Jabbour, G. E. & Doderer, D. Quantum dot solar cells: The best of both worlds. *Nat. Photonics* **4,** 604–605 (2010).

95. Hillhouse, H. W. & Beard, M. C. Solar cells from colloidal nanocrystals: Fundamentals, materials, devices, and economics. *Curr. Opin. Colloid Interface Sci.* **14,** 245–259 (2009).

96. Emin, S., Singh, S. P., Han, L., Satoh, N. & Islam, A. Colloidal quantum dot solar cells. *Sol. Energy* **85,** 1264–1282 (2011).

97. Kang, I. & Wise, F. W. Electronic structure and optical properties of PbS and PbSe quantum dots. *J. Opt. Soc. Am. B* **14,** 1632 (1997).

98. Krivoshlykov, S. G. Multiple exciton generation in PbSe and PbS nanocrystals incorporated into amorphous silicon p-n junction. *Phys. Status Solidi* **210,** 523–527 (2013).

99. Barkhouse, D. A. R., Pattantyus-Abraham, A. G., Levina, L. & Sargent, E. H. Thiols passivate recombination centers in colloidal quantum dots leading to enhanced photovoltaic device efficiency. *ACS Nano* **2,** 2356–62 (2008).

100. Moreels, I. *et al.* Size-Tunable, Bright, and Stable PbS Quantum Dots : A Surface Chemistry Study. *ACS Nano* **5,** 2004–2012 (2011).

101. Tang, J. *et al.* Schottky quantum dot solar cells stable in air under solar illumination. *Adv. Mater.* **22,** 1398–402 (2010).

102. Hughes, B. K. *et al.* Control of PbSe quantum dot surface chemistry and photophysics using an alkylselenide ligand. *ACS Nano* **6,** 5498–506 (2012).

103. Meza, E. Researchers boost CdTe cell efficiency from below 8% to 11.5%. *PV Mag.* (2013). at <http://www.pv-magazine.com/news/details/beitrag/researchers-boost-cdte-cell-efficiency-from-below-8-to-115-_100012391/#axzz2hJCsJ4Fo>

104. Clifford, J. P., Johnston, K. W., Levina, L. & Sargent, E. H. Schottky barriers to colloidal quantum dot films. *Appl. Phys. Lett.* **91,** 253117 (2007).

105. Kikuchi, E., Kitada, S., Ohno, A., Aramaki, S. & Maenosono, S. Solution-processed polymer-free photovoltaic devices consisting of PbSe colloidal quantum dots and tetrabenzoporphyrins. *Appl. Phys. Lett.* **92,** 173307 (2008).

106. Arango, A. C., Oertel, D. C., Xu, Y., Bawendi, M. G. & Bulovic, V. Heterojunction Photovoltaics Using Printed Colloidal Quantum Dots as a Photosensitive Layer 2009. *Nano Lett.* **9,** 860–863 (2009).

107. Stavrinadis, A. *et al.* SnS/PbS nanocrystal heterojunction photovoltaics. *Nanotechnology* **21,** 185202 (2010).

108. Hernández-Borja, J., Vorobiev, Y. V. & Ramírez-Bon, R. Thin film solar cells of CdS/PbS chemically deposited by an ammonia-free process. *Sol. Energy Mater. Sol. Cells* **95,** 1882–1888 (2011).

109. McDonald, S. A. *et al.* Solution-processed PbS quantum dot infrared photodetectors and photovoltaics. *Nat. Mater.* **4,** 138–42 (2005).

110. Wang, L., Zhao, D., Su, Z. & Shen, D. Hybrid polymer/ZnO solar cells sensitized by PbS quantum dots. *Nanoscale Res. Lett.* **7,** 106 (2012).

111. Pattantyus-Abraham, A. G. *et al.* Depleted-Heterojunction Colloidal Quantum Dot Solar Cells. *ACS Nano* **4,** 3374–3380 (2010).

112. Brown, P. R. *et al.* Improved current extraction from ZnO/PbS quantum dot heterojunction photovoltaics using a MoO3 interfacial layer. *Nano Lett.* **11,** 2955–61 (2011).

113. Gao, J. *et al.* Annealing effect of PbS quantum dot solar cells. *2011 37th IEEE Photovolt. Spec. Conf.* 002619–002621 (2011). doi:10.1109/PVSC.2011.6186485

114. Pacholski, C., Kornowski, A. & Weller, H. Self-assembly of ZnO: from nanodots to nanorods. *Angew. Chem. Int. Ed. Engl.* **41,** 1188–91 (2002).

115. Greenham, N., Peng, X. & Alivisatos, A. Charge separation and transport in conjugated-polymer/semiconductor-nanocrystal composites studied by photoluminescence quenching and photoconductivity. *Phys. Rev. B. Condens. Matter* **54,** 17628–17637 (1996).

116. Saunders, B. R. Hybrid polymer/nanoparticle solar cells: preparation, principles and challenges. *J. Colloid Interface Sci.* **369,** 1–15 (2012).

117. Willis, S. M., Cheng, C., Assender, H. E. & Watt, A. A. R. The transitional heterojunction behavior of PbS/ZnO colloidal quantum dot solar cells. *Nano Lett.* **12,** 1522–6 (2012).

118. Luther, J. M. *et al.* Stability assessment on a 3% bilayer PbS/ZnO quantum dot heterojunction solar cell. *Adv. Mater.* **22,** 3704–7 (2010).

119. Ehrler, B. *et al.* Preventing interfacial recombination in colloidal quantum dot solar cells by doping the metal oxide. *ACS Nano* **7,** 4210–20 (2013).

120. Sigma-Aldrich. Indium Tin Oxide (ITO) Coated Substrates. (2013). at <http://www.sigmaaldrich.com/materials-science/material-science-products.html?TablePage=9548901>

121. Tolcin, A. *U.S. Geological Survery - Mineral Commodity Summaries - Indium*. (2013). at <http://minerals.usgs.gov/minerals/pubs/commodity/indium/mcs-2013-indiu.pdf>

122. Liu, H., Avrutin, V., Izyumskaya, N., Özgür, Ü. & Morkoç, H. Transparent conducting oxides for electrode applications in light emitting and absorbing devices. *Superlattices Microstruct.* **48,** 458–484 (2010).

123. Materion. AZO transparent conductive coating. (2008). at <http://materion.com/ResourceCenter/ProductData/InorganicChemicals/Oxides/BrochuresAndDataSheets/AZOTransparentConductiveCoating.aspx>

124. Agura, H. *et al.* Low-resistive and transparent AZO films prepared by PLD in magnetic field. *Electr. Eng. Japan* **151,** 40–45 (2005).

125. Kim, S.-M., Rim, Y.-S., Keum, M.-J. & Kim, K.-H. Study on the electrical and optical properties of ITO and AZO thin film by oxygen gas flow rate. *J. Electroceramics* **23,** 341–345 (2008).

126. Bel Hadj Tahar, R., Ban, T., Ohya, Y. & Takahashi, Y. Tin doped indium oxide thin films: Electrical properties. *J. Appl. Phys.* **83,** 2631 (1998).

127. Chen, Z., Cotterell, B., Wang, W., Guenther, E. & Chua, S. A mechanical assessment of flexible optoelectronic devices. *Thin Solid Films* **394,** 202–206 (2001).

128. Ni, J. L. *et al.* Comparative investigation of fracture behaviour of aluminium-doped ZnO films on a flexible substrate. *J. Phys. D. Appl. Phys.* **42,** 175404 (2009).

129. Groenendaal, B. L., Jonas, F., Freitag, D., Pielartzik, H. & Reynolds, J. R. Poly(3,4-ethylenedioxythiophene) and Its Derivatives : Past, Present, and Future. *Adv. Mater.* **7,** 481–494 (2000).

130. Vosgueritchian, M., Lipomi, D. J. & Bao, Z. Highly Conductive and Transparent PEDOT:PSS Films with a Fluorosurfactant for Stretchable and Flexible Transparent Electrodes. *Adv. Funct. Mater.* **22,** 421–428 (2012).

131. Jönsson, S. K. . *et al.* The effects of solvents on the morphology and sheet resistance in poly(3,4-ethylenedioxythiophene)–polystyrenesulfonic acid (PEDOT–PSS) films. *Synth. Met.* **139,** 1–10 (2003).

132. Na, S.-I., Kim, S.-S., Jo, J. & Kim, D.-Y. Efficient and Flexible ITO-Free Organic Solar Cells Using Highly Conductive Polymer Anodes. *Adv. Mater.* **20,** 4061–4067 (2008).

133. Aernouts, T. *et al.* Printable anodes for flexible organic solar cell modules. *Thin Solid Films* **451-452,** 22–25 (2004).

134. Yu, J.-S. *et al.* Silver front electrode grids for ITO-free all printed polymer solar cells with embedded and raised topographies, prepared by thermal imprint, flexographic and inkjet roll-to-roll processes. *Nanoscale* **4,** 6032–40 (2012).

135. Angmo, D. *et al.* Scalability and stability of very thin, roll-to-roll processed, large area, indium-tin-oxide free polymer solar cell modules. *Org. Electron.* **14,** 984–994 (2013).

136. Lee, J.-Y., Connor, S. T., Cui, Y. & Peumans, P. Solution-processed metal nanowire mesh transparent electrodes. *Nano Lett.* **8,** 689–92 (2008).

137. Gaynor, W., Lee, J.-Y. & Peumans, P. Fully solution-processed inverted polymer solar cells with laminated nanowire electrodes. *ACS Nano* **4,** 30–4 (2010).

138. Wu, Z. *et al.* Transparent, conductive carbon nanotube films. *Science (80-.).* **305,** 1273–6 (2004).

139. Andrew Ng, M. H., Hartadi, L. T., Tan, H. & Patrick Poa, C. H. Efficient coating of transparent and conductive carbon nanotube thin films on plastic substrates. *Nanotechnology* **19,** 205703 (2008).

140. Ebbesen, T. W. *et al.* Electrical conductivity of individual carbon nanotubes. *Nature* **382,** 54–56 (1996).

141. Garrett, M. P., Ivanov, I. N., Gerhardt, R. a., Puretzky, A. a. & Geohegan, D. B. Separation of junction and bundle resistance in single wall carbon nanotube percolation networks by impedance spectroscopy. *Appl. Phys. Lett.* **97,** 163105 (2010).

142. Hu, L., Li, J., Liu, J., Grüner, G. & Marks, T. Flexible organic light-emitting diodes with transparent carbon nanotube electrodes: problems and solutions. *Nanotechnology* **21,** 155202 (2010).

143. Nair, R. R. *et al.* Fine Structure Constant Defines Visual Transparency of Graphene. *Science (80-.).* **320,** 1308 (2008).

144. Şahin, H. *et al.* Monolayer honeycomb structures of group-IV elements and III-V binary compounds: First-principles calculations. *Phys. Rev. B* **80,** 155453 (2009).

145. Lee, C., Wei, X., Kysar, J. W. & Hone, J. Measurement of the elastic properties and intrinsic strength of monolayer graphene. *Science (80-.).* **321,** 385–8 (2008).

146. Gomez De Arco, L. *et al.* Continuous, highly flexible, and transparent graphene films by chemical vapor deposition for organic photovoltaics. *ACS Nano* **4,** 2865–73 (2010).

147. Das Sarma, S., Adam, S., Hwang, E. H. & Rossi, E. Electronic transport in two-dimensional graphene. *Rev. Mod. Phys.* **83,** 407–470 (2011).

148. Novoselov, K. S. *et al.* Two-dimensional gas of massless Dirac fermions in graphene. *Nature* **438,** 197–200 (2005).

149. Bae, S. *et al.* Roll-to-roll production of 30-inch graphene films for transparent electrodes. *Nat. Nanotechnol.* **5,** 574–8 (2010).

150. Park, H., Brown, P. R., Bulović, V. & Kong, J. Graphene as transparent conducting electrodes in organic photovoltaics: studies in graphene morphology, hole transporting layers, and counter electrodes. *Nano Lett.* **12,** 133–40 (2012).

151. Huang, P. Y. *et al.* Grains and grain boundaries in single-layer graphene atomic patchwork quilts. *Nature* **469,** 389–92 (2011).

152. Choi, Y.-Y., Kang, S. J., Kim, H.-K., Choi, W. M. & Na, S.-I. Multilayer graphene films as transparent electrodes for organic photovoltaic devices. *Sol. Energy Mater. Sol. Cells* **96,** 281–285 (2012).

153. Liu, Z., Li, J. & Yan, F. Package-Free Flexible Organic Solar Cells with Graphene top Electrodes. *Adv. Mater.* **25,** 4296–4301 (2013).

154. Partoens, B. & Peeters, F. From graphene to graphite: Electronic structure around the K point. *Phys. Rev. B* **74,** 075404 (2006).

155. Wang, H., Maiyalagan, T. & Wang, X. Review on Recent Progress in Nitrogen-Doped Graphene: Synthesis, Characterization, and Its Potential Applications. *ACS Catal.* **2,** 781–794 (2012).

156. Liu, Z. *et al.* The application of highly doped single-layer graphene as the top electrodes of semitransparent organic solar cells. *ACS Nano* **6,** 810–8 (2012).

157. Gierz, I., Riedl, C., Starke, U., Ast, C. R. & Kern, K. Atomic hole doping of graphene. *Nano Lett.* **8,** 4603–7 (2008).

158. Tongay, S. *et al.* Stable hole doping of graphene for low electrical resistance and high optical transparency. *Nanotechnology* **22,** 425701 (2011).

159. Chen, G. *et al.* Co-evaporated bulk heterojunction solar cells with >6.0% efficiency. *Adv. Mater.* **24,** 2768–73 (2012).

160. Choe, M. *et al.* Efficient bulk-heterojunction photovoltaic cells with transparent multi-layer graphene electrodes. *Org. Electron.* **11,** 1864–1869 (2010).

161. Fan, B. *et al.* Squaraine Planar-Heterojunction Solar Cells. *Int. J. Photoenergy* **2009,** 1–7 (2009).

162. Shrotriya, V., Li, G., Yao, Y., Chu, C.-W. & Yang, Y. Transition metal oxides as the buffer layer for polymer photovoltaic cells. *Appl. Phys. Lett.* **88,** 073508 (2006).

163. Shen, H. & Pollak, F. H. Generalized Franz-Keldysh theory of electromodulation. *Phys. Rev. B* **42,** 7097 – 7102 (1990).

164. Aspnes, D. E. Third-Derivative Modulation Spectroscopy with Low-Field Electroreflectance. *Surf. Sci.* **37,** 418–442 (1973).

165. Xavier, F. P. Application of electroreflectance analysis for organic semiconductor thin films. *Bull. Mater. Sci.* **20,** 651–665 (1997).

166. Canovas, E. *et al.* Application of the photoreflectance technique to the characterization of quantum dot intermediate band materials for solar cells. *Thin Solid Films* **516,** 6943–6947 (2008).

167. Blume, G., Hosea, T. J. C. & Sweeney, S. J. A study of the low-energy interference oscillations in photoreflectance of GaAsSb/GaAs quantum well structures. *Phys. Status Solidi* **202,** 1244–1254 (2005).

168. Nonomura, S., Okamoto, H. & Hamakawa, Y. A Study of Built-in Potential in a-Si Solar Cells by Means of Back-Surface Reflected Electroabsorption. *Appl. Phys. A* **38,** 31–38 (1983).

169. Yamashita, K., Kita, T. & Nishino, T. Linear electrooptic effect in ordered AlGaInP. *J. Appl. Phys.* **86,** 3140–3143 (1999).

170. Tober, R. L. & Bahder, T. B. Determining the electric field in [111] strained-layer quantum wells. *Appl. Phys. Lett.* **63,** 2369–2371 (1993).

171. Aspnes, D. E. & Studna, A. A. Schottky-Barrier Electroreflectance: Application to GaAs. *Phys. Rev. B* **7,** 4605 – 4624 (1973).

172. Gilman, J. M. A., Hamnett, A. & Batchelor, R. A. Franz-Keldysh and band-filling effects in the electroreflectance of highly doped p-type GaAs. *Phys. Rev. B* **46,** 363–370 (1992).

173. Bentham. Bentham 225 Lock-in Amplifier. at <http://www.bentham.co.uk/pdf/F225.pdf>

174. Nelson, J. *The Physics of Solar Cells*. 328 (Imperial College Press, 2003).

175. Dai, Q. *et al.* Stability study of PbSe semiconductor nanocrystals over concentration, size, atmosphere, and light exposure. *Langmuir* **25,** 12320–4 (2009).

176. Reuter, D., Schafmeister, P., Kailuweit, P. & Wieck, a. D. Frequency-dependent C(V) spectroscopy of the hole system in InAs quantum dots. *Phys. E Low-dimensional Syst. Nanostructures* **21,** 445–450 (2004).

177. Wetzler, R. *et al.* Capacitance–voltage characteristics of InAs/GaAs quantum dots embedded in a pn structure. *Appl. Phys. Lett.* **77,** 1671 (2000).

178. Linares, P. G. *et al.* Voltage recovery in intermediate band solar cells. *Sol. Energy Mater. Sol. Cells* **98,** 240–244 (2012).

179. Luque, A. *et al.* Radiative thermal escape in intermediate band solar cells. *AIP Adv.* **1,** 022125 (2011).

180. Antolín, E. *et al.* Reducing carrier escape in the InAs/GaAs quantum dot intermediate band solar cell. *J. Appl. Phys.* **108,** 064513 (2010).

181. Zollner, S., Sudha, G. & Cardona, M. The Temperature Dependence of the Band Gaps in InP, InAs, InSb and GaSb. *Solid State Commun.* **77,** 485–488 (1991).

182. Adachi, S. GaAs, AlAs, and AlxGa1−xAs Material parameters for use in research and device applications. *J. Appl. Phys.* **58,** R1 (1985).

183. Song, H. Z. *et al.* AlGaAs capping effect on InAs quantum dots self-assembled on GaAs. *Phys. Lett. A* **375,** 3517–3520 (2011).

184. De Pauw, P. in *Silicon Process. Photovoltaics II* (Khattak, C. P. & Ravi, K. V.) 72 (Elsevier B.V., 1987).

185. Langenkamp, M. & Breitenstein, O. Classification of shunting mechanisms in crystalline silicon solar cells. *Sol. Energy Mater. Sol. Cells* **72,** 433–440 (2002).

186. Giovane, L. M., Luan, H.-C., Agarwal, A. M. & Kimerling, L. C. Correlation between leakage current density and threading dislocation density in SiGe p-i-n diodes grown on relaxed graded buffer layers. *Appl. Phys. Lett.* **78,** 541 (2001).

187. Hook, J. R. & Hall, H. E. in *Solid State Phys.* 100–104 (John Wiley & Sons, Inc., 2003).

188. Seraphin, B. O. & Bottka, N. Franz-Keldysh Effect of the Refractive Index in Semiconductors. *Phys. Rev.* **139,** (1965).

189. Padera, F. Measuring Absorptance (k) and Refractive Index (n) of Thin Films with the PerkinElmer Lambda 950/1050 High Performance UV-Vis/NIR Spectrometers. (2013).

190. Tutu, F. K., Lam, P., Wu, J., Miyashita, N. & Okada, Y. InAs / GaAs quantum dot solar cell with an AlAs cap layer. *Appl. Phys. Lett.* **102,** 163907–1–4 (2013).

191. Yokota, H., Iizuka, K., Okamoto, H. & Suzuki, T. AlAs coating for stacked structure of self-assembled InAs/GaAs quantum dots. *J. Cryst. Growth* **301-302,** 825–827 (2007).

192. Airaksinen, V. M. & Lipsanen, H. K. Photoreflectance Study of Photovoltage Effects in GaAs diode structures. *Appl. Phys. Lett.* **60,** 2110–2112 (1992).

193. Hara, N. & Katoda, T. Characterization of interdiffusion coefficients in GaAs-AlAs superlattices with laser Raman spectroscopy. *J. Appl. Phys.* **69,** 2112 (1991).

194. García, J. M., Mankad, T., Holtz, P. O., Wellman, P. J. & Petroff, P. M. Electronic states tuning of InAs self-assembled quantum dots. *Appl. Phys. Lett.* **72,** 3172 (1998).

195. Cuadra, L., Marti, A. & Luque, A. Present status of intermediate band solar cell research. *Thin Solid Films* **451-452,** 593–599 (2004).

196. Okada, Y. *et al.* Increase in photocurrent by optical transitions via intermediate quantum states in direct-doped InAs/GaNAs strain-compensated quantum dot solar cell. *J. Appl. Phys.* **109,** 024301 (2011).

197. Dawson, P. *et al.* Relaxation and recombination in InAs quantum dots. *Phys. Status Solidi* **244,** 2803–2815 (2007).

198. Ghosh, S., Kochman, B., Singh, J. & Bhattacharya, P. Conduction band offset in InAs/GaAs self-organized quantum dots measured by deep level transient spectroscopy. *Appl. Phys. Lett.* **76,** 2571 (2000).

199. Nee, T.-E., Wu, Y.-F., Cheng, C.-C. & Shen, H.-T. Carrier dynamics study of the temperature- and excitation-dependent photoluminescence of InAs⁄GaAs quantum dots. *J. Appl. Phys.* **99,** 013506 (2006).

200. Mazur, Y. I. *et al.* Interdot carrier transfer in asymmetric bilayer InAs⁄GaAs quantum dot structures. *Appl. Phys. Lett.* **86,** 063102 (2005).

201. Dawson, P., Ma, Z., Pierz, K. & Göbel, E. O. Microsecond carrier recombination times in InAs/AlAs quantum dots. *Appl. Phys. Lett.* **81,** 2349 (2002).

202. Ma, Z., Pierz, K., Hübner, J. & Rühle, W. W. Nanosecond scale carrier dynamics of self-assembled InAs/AlAs quantum dots studied by time-resolved photoluminescence. *Phys. E Low-dimensional Syst. Nanostructures* **28,** 203–208 (2005).

203. Offermans, P. *et al.* Atomic-scale structure and photoluminescence of InAs quantum dots in GaAs and AlAs. *Phys. Rev. B* **72,** 165332 (2005).

204. Zhang, Y. . *et al.* Temperature dependence of electron redistribution in modulation-doped InAs/GaAs quantum dots. *J. Cryst. Growth* **219,** 199–204 (2000).

205. Varshni, P. Temperature dependence of the energy gap in semiconductors. *Physica* **34,** 149–154 (1967).

206. Kim, J. S., Ko, B. S., Yu, J. & Bae, I. Temperature- and Excitation-power-dependent Optical Properties of InAs / GaAs Quantum Dots by Comparison of Photoluminescence and Photoreflectance Spectroscopy. *J. Korean Phys. Soc.* **55,** 640–645 (2009).

207. Yeo, I., Dong Song, J. & Lee, J. Temperature-dependent energy band gap variation in self-organized InAs quantum dots. *Appl. Phys. Lett.* **99,** 151909 (2011).

208. Zhou, X. L. *et al.* Carrier tunneling effects on the temperature dependent photoluminescence of InAs/GaAs quantum dot: Simulation and experiment. *J. Appl. Phys.* **109,** 083501 (2011).

209. Polimeni, A., Patanè, A., Henini, M., Eaves, L. & Main, P. C. Temperature dependence of the optical properties of InAs / Al(y)Ga(1-y)As self-organized quantum dots. *Phys. Rev. B* **59,** 5064–5068 (1999).

210. Nelson, J. in *Phys. Sol. Cells* 66 (Imperial College Press, 2003).

211. Boix, P. P. *et al.* Determination of gap defect states in organic bulk heterojunction solar cells from capacitance measurements. *Appl. Phys. Lett.* **95,** 233302 (2009).

212. Fox, M. in *Opt. Prop. Solids* 280–281 (Oxford University Press, 2005).

213. Sharma, A., Kumar, P., Singh, B., Chaudhuri, S. R. & Ghosh, S. Capacitance-voltage characteristics of organic Schottky diode with and without deep traps. *Appl. Phys. Lett.* **99,** 023301 (2011).

214. Harada, K. *et al.* Organic Homojunction Diodes with a High Built-in Potential: Interpretation of the Current-Voltage Characteristics by a Generalized Einstein Relation. *Phys. Rev. Lett.* **94,** 036601 (2005).

215. Campbell, I. H., Smith, D. L. & Ferraris, J. P. Electrical impedance measurements of polymer light-emitting diodes. *Appl. Phys. Lett.* **66,** 3030 (1995).

216. Brounkov, P. N. *et al.* Electronic structure of self-assembled InAs quantum dots in GaAs matrix. *Appl. Phys. Lett.* **73,** 1092 (1998).

217. Wang, S. Y., Lin, S. D., Wu, H. W. & Lee, C. P. High performance InAs/GaAs quantum dot infrared photodetectors with AlGaAs current blocking layer. *Infrared Phys. Technol.* **42,** 473–477 (2001).

218. Shrotriya, V. & Yang, Y. Capacitance–voltage characterization of polymer light-emitting diodes. *J. Appl. Phys.* **97,** 054504 (2005).

219. Markvart, T. & Castaner, L. *Practical Handbook of Photovoltaics: Fundamentals and Applications*. 95–103 (Elsevier, 2003).

220. Wu, B. *et al.* Uncovering loss mechanisms in silver nanoparticle-blended plasmonic organic solar cells. *Nat. Commun.* **4,** 2004 (2013).

221. Breitenstein, O., Altermatt, P. P., Ramspeck, K. & Schenk, A. The Origin of Ideality Factors n > 2 of Shunts and Surfaces in the Dark I-V Curves of Si Solar Cells. *Proc. 21st Eur. PVSEC, Dresden* 625–628 (2006).

222. Alonso-Álvarez, D. *et al.* Carrier recombination effects in strain compensated quantum dot stacks embedded in solar cells. *Appl. Phys. Lett.* **93,** 123114 (2008).

223. Ng, J. T., Bangert, U. & Missous, M. Formation and role of defects in stacked large binary InAs/GaAs quantum dot structures. *Semicond. Sci. Technol.* **22,** 80–85 (2007).

224. Lu, H. F. *et al.* Temperature dependence of dark current properties of InGaAs/GaAs quantum dot solar cells. *Appl. Phys. Lett.* **98,** 183509 (2011).

225. Tarr, N. G. & Pulfrey, D. L. An investigation of dark current and photocurrent superposition in photovoltaic devices. *Solid. State. Electron.* **22,** 265–270 (1979).

226. Hegedus, S. S. Current - Voltage Analysis of a-Si and a-SiGe Solar Cells Including Voltage-dependent Photocurrent Collection. *Prog. Photovoltaics Res. Appl.* **5,** 151–168 (1997).

227. Hegedus, S. S., Desai, D. & Thompson, C. Voltage Dependent Photocurrent Collection in CdTe/CdS Solar Cells. *Prog. Photovoltaics Res. Appl.* **15,** 587–602 (2007).

228. Ali, B., Murray, R., Hegedus, S. S. & Ismat Shah, S. Analysis of voltage and temperature dependent photocurrent collection in p3ht/pcbm solar cells. *J. Appl. Phys.* **112,** 114514 (2012).

229. Sablon, K. A. *et al.* Strong enhancement of solar cell efficiency due to quantum dots with built-in charge. *Nano Lett.* **11,** 2311–7 (2011).

230. Ramey, S. M. & Khoie, R. Modeling of Multiple-Quantum-Well Solar Cells Including Capture , Escape , and Recombination of Photoexcited Carriers in Quantum Wells. *IEEE Trans. Electron Devices* **50,** 1179–1188 (2003).

231. Greenham, N. C., Peng, X. & Alivisatos, a. P. A CdSe nanocrystal/MEH-PPV polymer composite photovoltaic. *AIP Conf. Proc.* **295,** 295–302 (1997).

232. Ip, A. H. *et al.* Hybrid passivated colloidal quantum dot solids. *Nat. Nanotechnol.* **7,** 577–82 (2012).

233. Cheng, C. Semiconductor Colloidal Quantum Dots for Photovoltaic Applications: PbS/ZnO Bulk Heterojunctions. *DPhil Thesis, Univ. Oxford* (2013).

234. Forrest, S. R. The Limits to Organic Photovoltaic Cell Efficiency. *MRS Bull.* **30,** 28–32 (2005).

235. Ma, C. *et al.* Numerical model for planar heterojunction organic solar cells on the condition of short circuit. *Mater. Sci. Eng. B* **176,** 406–411 (2011).

236. Barkhouse, D. A. R., Kramer, I. J., Wang, X. & Sargent, E. H. Dead zones in colloidal quantum dot photovoltaics: evidence and implications. *Opt. Express* **18 Suppl 3,** A451–7 (2010).

237. Senger, R. & Bajaj, K. Optical properties of confined polaronic excitons in spherical ionic quantum dots. *Phys. Rev. B* **68,** 045313 (2003).

238. Leschkies, K. S., Beatty, T. J., Kang, M. S., Norris, D. J. & Aydil, E. S. Solar cells based on junctions between colloidal PbSe nanocrystals and thin ZnO films. *ACS Nano* **3,** 3638–48 (2009).

239. Choi, J. J. *et al.* PbSe nanocrystal excitonic solar cells. *Nano Lett.* **9,** 3749–55 (2009).

240. Hines, M. A. & Scholes, G. D. Colloidal PbS Nanocrystals with Size-Tunable Near-Infrared Emission: Observation of Post-Synthesis Self-Narrowing of the Particle Size Distribution. *Adv. Mater.* **15,** 1844–1849 (2003).

241. Luther, J. M. *et al.* Structural, optical, and electrical properties of self-assembled films of PbSe nanocrystals treated with 1,2-ethanedithiol. *ACS Nano* **2,** 271–80 (2008).

242. Schedelbeck, G. Coupled Quantum Dots Fabricated by Cleaved Edge Overgrowth: From Artificial Atoms to Molecules. *Science (80-.).* **278,** 1792–1795 (1997).

243. Wehrenberg, B. L., Wang, C. & Guyot-Sionnest, P. Interband and Intraband Optical Studies of PbSe Colloidal Quantum Dots. *J. Phys. Chem. B* **106,** 10634–10640 (2002).

244. Roth, A. P., Webb, J. B. & Williams, D. F. Absorption Edge Shift in ZnO Thin Films at High Carrier Densities. *Solid State Commun.* **39,** 1269–1271 (1981).

245. Hyun, B. *et al.* Electron Injection from Colloidal PbS Nanoparticles. *ACS Nano* **2,** (2008).

246. Zhang, Y. *et al.* Hole transfer from PbS nanocrystal quantum dots to polymers and efficient hybrid solar cells utilizing infrared photons. *Org. Electron.* **13,** 2773–2780 (2012).

247. Nanda, K. K. & Sahu, S. N. One-Dimensional Quantum Confinement in Electrodeposited PbS Nanocrystalline Semiconductors. *Adv. Mater.* **13,** 280–283 (2001).

248. Micali, N., Mallamace, F., Castriciano, M., Romeo, A. & Scolaro, L. M. Separation of Scattering and Absorption Contributions in UV / Visible Spectra of Resonant Systems. *Anal. Chem.* **73,** 4958–4963 (2001).

249. Ye, J. *et al.* Size-controllable synthesis of spherical ZnO nanoparticles: Size- and concentration-dependent resonant light scattering. *Microchem. J.* **100,** 61–65 (2012).

250. Zhang, Q., Dandeneau, C. S., Zhou, X. & Cao, G. ZnO Nanostructures for Dye-Sensitized Solar Cells. *Adv. Mater.* **21,** 4087–4108 (2009).

251. Xu, F., Benavides, J., Ma, X. & Cloutier, S. G. Interconnected TiO2 Nanowire Networks for PbS Quantum Dot Solar Cell Applications. *J. Nanotechnol.* **2012,** 1–6 (2012).

252. Jarzab, D. *et al.* Low-Temperature Behaviour of Charge Transfer Excitons in Narrow-Bandgap Polymer-Based Bulk Heterojunctions. *Adv. Energy Mater.* **1,** 604–609 (2011).

253. Li, Z.-L. *et al.* Strong red emission in heterojunctions of conjugated polymer blends. *Appl. Phys. Lett.* **84,** 4944 (2004).

254. Dantas, N. O., de Paula, P. M. N., Silva, R. S., López-Richard, V. & Marques, G. E. Radiative versus nonradiative optical processes in PbS nanocrystals. *J. Appl. Phys.* **109,** 024308 (2011).

255. Yoon, W. *et al.* Enhanced Open-Circuit Voltage of PbS Nanocrystal Quantum Dot Solar Cells. *Sci. Rep.* **3,** 2225 (2013).

256. Tang, J. *et al.* Colloidal-quantum-dot photovoltaics using atomic-ligand passivation. *Nat. Mater.* **10,** 765–771 (2011).

257. Pendyala, N. B. & Koteswara Rao, K. S. R. Identification of surface states in PbS quantum dots by temperature dependent photoluminescence. *J. Lumin.* **128,** 1826–1830 (2008).

258. Yu, P. & Cardona, M. *Fundamentals of Semiconductors: Physics and Materials Properties*. 247 (Springer, 2010).

259. Moreels, I. *et al.* Size-dependent optical properties of colloidal PbS quantum dots. *ACS Nano* **3,** 3023–30 (2009).

260. Schoolar, R. . & Dixon, J. R. Optical Constants of Lead Sulphide in the Fundamental Absorption Edge Region. *Phys. Rev.* **137,** A 667 – A 670 (1965).

261. Tang, J. & Sargent, E. H. Infrared colloidal quantum dots for photovoltaics: fundamentals and recent progress. *Adv. Mater.* **23,** 12–29 (2011).

262. Cuiffi, J., Benanti, T., Nam, W. J. & Fonash, S. Modeling of bulk and bilayer organic heterojunction solar cells. *Appl. Phys. Lett.* **96,** 143307 (2010).

263. Chen, T. L., Chen, J. J.-A., Catane, L. & Ma, B. Fully solution processed p-i-n organic solar cells with an industrial pigment – Quinacridone. *Org. Electron.* **12,** 1126–1131 (2011).

264. Matsuo, Y. *et al.* Columnar structure in bulk heterojunction in solution-processable three-layered p-i-n organic photovoltaic devices using tetrabenzoporphyrin precursor and silylmethyl[60]fullerene. *J. Am. Chem. Soc.* **131,** 16048–50 (2009).

265. Yang, F., Shtein, M. & Forrest, S. R. Controlled growth of a molecular bulk heterojunction photovoltaic cell. *Nat. Mater.* **4,** 37–41 (2004).

266. Park, S., Tark, S. J., Lee, J. S., Lim, H. & Kim, D. Effects of intrinsic ZnO buffer layer based on P3HT/PCBM organic solar cells with Al-doped ZnO electrode. *Sol. Energy Mater. Sol. Cells* **93,** 1020–1023 (2009).

267. Scher, H. & Zallen, R. Critical Density in Percolation Processes. *J. Chem. Phys.* **53,** 3759 (1970).

268. Timp, B. A. & Zhu, X.-Y. Electronic energy alignment at the PbSe quantum dots/ZnO(10$\bar{1}$0) interface. *Surf. Sci.* **604,** 1335–1341 (2010).

269. Rand, B., Burk, D. & Forrest, S. Offset energies at organic semiconductor heterojunctions and their influence on the open-circuit voltage of thin-film solar cells. *Phys. Rev. B* **75,** 1–11 (2007).

270. Liu, Z. T. *et al.* Influence of the donor/acceptor interface on the open-circuit voltage in organic solar cells. *Appl. Phys. Lett.* **95,** 093307 (2009).

271. Lenes, M., Morana, M., Brabec, C. J. & Blom, P. W. M. Recombination-Limited Photocurrents in Low Bandgap Polymer/Fullerene Solar Cells. *Adv. Funct. Mater.* **19,** 1106–1111 (2009).

272. Nelson, J. in *Phys. Sol. Cells* 224 (Imperial College Press, 2003).

273. Jeong, W.-I. *et al.* Photoconductivity of C60 as an Origin of Bias-Dependent Photocurrent in Organic Photovoltaics. *Adv. Funct. Mater.* **22,** 3089–3094 (2012).

274. Riedel, I. *et al.* Effect of Temperature and Illumination on the Electrical Characteristics of Polymer–Fullerene Bulk-Heterojunction Solar Cells. *Adv. Funct. Mater.* **14,** 38–44 (2004).

275. Waldauf, C., Scharber, M. C., Schilinsky, P., Hauch, J. a. & Brabec, C. J. Physics of organic bulk heterojunction devices for photovoltaic applications. *J. Appl. Phys.* **99,** 104503 (2006).

276. Khan, F., Singh, S. N. & Husain, M. Effect of illumination intensity on cell parameters of a silicon solar cell. *Sol. Energy Mater. Sol. Cells* **94,** 1473–1476 (2010).

277. Nelson, J. in *Phys. Sol. Cells* 160–165 (Imperial College Press, 2003).

278. Wang, K. *et al.* Thermally evaporated Cu[2]ZnSnS[4] solar cells. *Appl. Phys. Lett.* **97,** 143508 (2010).

279. Potscavage, W. J., Yoo, S. & Kippelen, B. Origin of the open-circuit voltage in multilayer heterojunction organic solar cells. *Appl. Phys. Lett.* **93,** 193308 (2008).

280. Lee, J. H., Cho, S., Roy, A., Jung, H.-T. & Heeger, A. J. Enhanced diode characteristics of organic solar cells using titanium suboxide electron transport layer. *Appl. Phys. Lett.* **96,** 163303 (2010).

281. Ratcliff, E. L. *et al.* Investigating the Influence of Interfacial Contact Properties on Open Circuit Voltages in Organic Photovoltaic Performance: Work Function Versus Selectivity. *Adv. Energy Mater.* **3,** 647–656 (2013).

282. Zuo, L. *et al.* Immerse precipitation as an efficient protocol to optimize morphology and performance of organic solar cells. *Appl. Phys. Lett.* **101,** 233306 (2012).

283. Brus, V. V. Open-circuit analysis of thin film heterojunction solar cells. *Sol. Energy* **86,** 1600–1604 (2012).

284. Tumbleston, J. R., Ko, D.-H., Samulski, E. T. & Lopez, R. Nonideal parasitic resistance effects in bulk heterojunction organic solar cells. *J. Appl. Phys.* **108,** 084514 (2010).

285. Ryan, J. W., Marin-Beloqui, J. M., Albero, J. & Palomares, E. Nongeminate Recombination Dynamics−Device Voltage Relationship in Hybrid PbS Quantum Dot/C60 Solar Cells. *J. Phys. Chem. C* **117,** 17470–17476 (2013).

286. Gao, J. & Johnson, J. C. Charge trapping in bright and dark states of coupled PbS quantum dot films. *ACS Nano* **6,** 3292–303 (2012).

287. Xiong, G., Pal, U. & Serrano, J. G. Correlations among size, defects, and photoluminescence in ZnO nanoparticles. *J. Appl. Phys.* **101,** 024317 (2007).

288. Hsu, H.-C., Huang, H.-Y., Eriksson, M. O., Dai, T.-F. & Holtz, P.-O. Surface related and intrinsic exciton recombination dynamics in ZnO nanoparticles synthesized by a sol-gel method. *Appl. Phys. Lett.* **102,** 013109 (2013).

289. Choi, H., Ko, J.-H., Kim, Y.-H. & Jeong, S. Steric-hindrance-driven shape transition in PbS quantum dots: understanding size-dependent stability. *J. Am. Chem. Soc.* **135,** 5278–81 (2013).

290. Wang, X., Zhi, L. & Müllen, K. Transparent, conductive graphene electrodes for dye-sensitized solar cells. *Nano Lett.* **8,** 323–7 (2008).

291. Lee, Y.-Y. *et al.* Top laminated graphene electrode in a semitransparent polymer solar cell by simultaneous thermal annealing/releasing method. *ACS Nano* **5,** 6564–70 (2011).

292. Mak, K. F., Sfeir, M. Y., Misewich, J. a & Heinz, T. F. The evolution of electronic structure in few-layer graphene revealed by optical spectroscopy. *Proc. Natl. Acad. Sci. U. S. A.* **107,** 14999–5004 (2010).

293. Wallace, P. R. The Band Theory of Graphite. *Physical* **71,** 622 (1947).

294. Wu, J. *et al.* Organic solar cells with solution-processed graphene transparent electrodes. *Appl. Phys. Lett.* **92,** 263302 (2008).

295. Kang, J.-W. *et al.* Reduction of Series Resistance in Organic Photovoltaic Using Low Sheet Resistance of ITO Electrode. *Electrochem. Solid-State Lett.* **12,** H64 (2009).

296. Angmo, D. & Krebs, F. C. Flexible ITO-free polymer solar cells. *J. Appl. Polym. Sci.* **129,** 1–14 (2013).

297. Heliatek. Efficient manufacture of innovative solar films. at <http://www.heliatek.com/technologie/fertigung/?lang=en>

298. Bishop, C. *Roll-to-Roll Vacuum Deposition of Barrier Coatings*. p. 4 (Wiley-Scrivener, 2010).

299. Chen, G. *et al.* Optical and electrical properties of a squaraine dye in photovoltaic cells. *Appl. Phys. Lett.* **101,** 083904 (2012).

300. Wang, S. *et al.* High efficiency organic photovoltaic cells based on a vapor deposited squaraine donor. *Appl. Phys. Lett.* **94,** 233304 (2009).

301. Pfuetzner, S., Meiss, J., Petrich, A., Riede, M. & Leo, K. Improved bulk heterojunction organic solar cells employing C[70] fullerenes. *Appl. Phys. Lett.* **94,** 223307 (2009).

302. Li, W. *et al.* Efficient Small Bandgap Polymer Solar Cells with High Fill Factors for 300 nm Thick Films. *Adv. Mater.* **25,** 3182–6 (2013).

303. Suk, J. W. *et al.* Transfer of CVD-grown monolayer graphene onto arbitrary substrates. *ACS Nano* **5,** 6916–24 (2011).

304. Park, H., Shi, Y. & Kong, J. Application of solvent modified PEDOT:PSS to graphene electrodes in organic solar cells. *Nanoscale* (2013). doi:10.1039/c3nr00611e

305. Wei, G., Wang, S., Renshaw, K., Thompson, M. E. & Forrest, S. R. Solution-Processed Squaraine Bulk Heterojunction Photovoltaic Cells. *ACS Nano* **4,** 1927–1934 (2010).

306. Ni, Z. H. *et al.* Graphene thickness determination using reflection and contrast spectroscopy. *Nano Lett.* **7,** 2758–63 (2007).

307. Blake, P. *et al.* Graphene-based liquid crystal device. *Nano Lett.* **8,** 1704–8 (2008).

308. Caglar, M., Caglar, Y. & Ilican, S. The determination of the thickness and optical constants of the ZnO crystalline thin film by using envelope method. *J. Optoelectron. Adv. Mater.* **8,** 1410–1413 (2006).

309. Elite, J. & Spencer, A. G. *Indium Tin Oxide for transparent EMC shielding and Anti-static applications*. (2004). at <http://www.diamondcoatings.co.uk/datasheet/emc_ito_presentation.pdf>

310. Eo, Y. S., Rhee, H. W., Chin, B. D. & Yu, J.-W. Influence of metal cathode for organic photovoltaic device performance. *Synth. Met.* **159,** 1910–1913 (2009).

311. Mihailetchi, V. D., Blom, P. W. M., Hummelen, J. C. & Rispens, M. T. Cathode dependence of the open-circuit voltage of polymer:fullerene bulk heterojunction solar cells. *J. Appl. Phys.* **94,** 6849 (2003).

312. Lo, M. F. *et al.* Limits of open circuit voltage in organic photovoltaic devices. *Appl. Phys. Lett.* **96,** 113303 (2010).

313. Kinoshita, Y., Takenaka, R. & Murata, H. Independent control of open-circuit voltage of organic solar cells by changing film thickness of MoO[sub 3] buffer layer. *Appl. Phys. Lett.* **92,** 243309 (2008).

314. Bijleveld, J. C., Verstrijden, R. a. M., Wienk, M. M. & Janssen, R. a. J. Maximizing the open-circuit voltage of polymer: Fullerene solar cells. *Appl. Phys. Lett.* **97,** 073304 (2010).

315. Aksoy, B., Coskun, S., Kucukyildiz, S. & Unalan, H. E. Transparent, highly flexible, all nanowire network germanium photodetectors. *Nanotechnology* **23,** 325202 (2012).

316. Qiu, C., Xie, Z., Chen, H., Wong, M. & Kwok, H. S. Comparative study of metal or oxide capped indium–tin oxide anodes for organic light-emitting diodes. *J. Appl. Phys.* **93,** 3253 (2003).

317. Cattin, L. *et al.* MoO3 surface passivation of the transparent anode in organic solar cells using ultrathin films. *J. Appl. Phys.* **105,** 034507 (2009).

318. Noh, S., Suman, C. K., Lee, D., Kim, S. & Lee, C. Study of Buffer Layer Thickness on Bulk Heterojunction Solar Cell. *J. Nanosci. Nanotechnol.* **10,** 6815–6818 (2010).

319. Parker, I. D. & Kim, H. H. Fabrication of polymer light-emitting diodes using doped silicon electrodes. *Appl. Phys. Lett.* **64,** 1774 (1994).

320. Lassiter, B. E., Zimmerman, J. D., Panda, A., Xiao, X. & Forrest, S. R. Tandem organic photovoltaics using both solution and vacuum deposited small molecules. *Appl. Phys. Lett.* **101,** 063303 (2012).

321. Chiu, S.-W. *et al.* A donor-acceptor-acceptor molecule for vacuum-processed organic solar cells with a power conversion efficiency of 6.4%. *Chem. Commun. (Camb).* **48,** 1857–9 (2012).

322. Wei, G. *et al.* Functionalized squaraine donors for nanocrystalline organic photovoltaics. *ACS Nano* **6,** 972–8 (2012).

323. Pfuetzner, S. Studies on Organic Solar Cells Composed of Fullerenes and Zinc-Phthalocyanines. 92 (2011).

324. Wei, G. *et al.* Arylamine-based squaraine donors for use in organic solar cells. *Nano Lett.* **11,** 4261–4 (2011).

325. Peumans, P., Yakimov, A. & Forrest, S. R. Small molecular weight organic thin-film photodetectors and solar cells. *J. Appl. Phys.* **93,** 3693 (2003).

326. Zhang, C. *et al.* Facile One-Step Fabrication of Ordered Organic Nanowire Films. *Adv. Mater.* **21,** 4172–4175 (2009).

327. Tress, W., Leo, K. & Riede, M. Effect of concentration gradients in ZnPc:C60 bulk heterojunction organic solar cells. *Sol. Energy Mater. Sol. Cells* **95,** 2981–2986 (2011).

328. Riedel, I. & Dyakonov, V. Influence of electronic transport properties of polymer-fullerene blends on the performance of bulk heterojunction photovoltaic devices. *Phys. Status Solidi* **201,** 1332–1341 (2004).

329. Burkhard, G. F., Hoke, E. T., Beiley, Z. M. & McGehee, M. D. Free Carrier Generation in Fullerene Acceptors and Its Effect on Polymer Photovoltaics. *J. Phys. Chem. C* **116,** 26674–26678 (2012).

330. Kazaoui, S., Minami, N. & Tanabe, Y. Comprehensive analysis of intermolecular charge-transfer excited states in C60 and C70 films. *Phys. Rev. B* **58,** 7689–7700 (1998).

331. Gloeckler, M. & Sites, J. R. Apparent quantum efficiency effects in CdTe solar cells. *J. Appl. Phys.* **95,** 4438 (2004).